



# Dynamics of Frenkel Excitons in Pigment-Protein Complexes and Hybrid Systems

**Dissertation**

zur Erlangung des Grades  
doctor rerum naturalium (Dr. rer. nat.)

am Institut für Physik  
der Mathematisch-Naturwissenschaftlichen Fakultät  
der Universität Rostock

Rostock, 2019

**vorgelegt von:**

Xiaomeng Liu

aus Rostock

geboren am 02.10.1987 in Shandong



**Gutachter:**

1. Gutachter:

Prof. Dr. Oliver Kühn,  
Institut für Physik, Universität Rostock

2. Gutachter:

PD Dr. Volkhard May,  
Institut für Physik, Humboldt Universität Berlin

**Datum der Einreichung:** 21. Februar 2019

**Datum der Verteidigung:** 21. Juni 2019



---

# Abstract

The understanding of the fundamental processes determining the efficiency of electronic excitation energy (exciton) transfer in photosynthetic light-harvesting is of vital importance for the design of new solar energy driven materials. Recently, quantum coherence involving exciton-vibrational coupling has been realized to play an important role for the high efficiency of the energy transfer process. In this thesis, a Quantum Master Equation approach is applied to describe the exciton dynamics of the Fenna-Matthews-Olson complex, paying special attention to the effects of vibrations that are taken into account explicitly. Two different models are contrasted, namely the one- and two-particle approximation to the exciton-vibrational basis, and compared with a purely excitonic model. It is found that (i) explicit inclusion of vibrations into the relevant system influences the trapping at the reaction center site considerably and (ii) the difference between the one- and two-particle approximation is of qualitative nature. In a further application an excitonic model is applied to the description of the LH2 antenna complex of the bacterium *Alc. vinosum*. Here the goal has been to unravel the origin of the unusual B800 absorption band splitting and to connect this to observed exciton relaxation rates. A key point of the model is the particular arrangement of transition dipoles in combination with B800 and B850 pigment pool specific relaxation rates.

In the second part of the thesis the focus is put on hybrid systems consisting of metal nanospheres and aggregates composed of organic dyes. A density functional theory-based tight binding approach yielding a discrete representation of the electronic quantum mechanical charge density in terms of atom-centred Mulliken charges is used for the description of the molecules. It is self-consistently linked to the classical polarization field of the nanosphere. Particular emphasis is put on the analysis of the energetics of the static case and here on the influence of system parameters such as the nanosphere's radius, the type of molecule and their mutual distance. It is found that charge-neutral and charged molecules show a rather different non-trivial distance dependence of the interaction energy.

Finally, excitation of the hybrid system by an external field is considered. Molecules next to the surface of the nanosphere experience an additional near field which enhances their excitation as compared to further away molecules, e.g. in an aggregate. Conditions are identified where the excitation dynamics of the nanosphere-aggregate hybrid system can be described using an effective single particle model. The polarization effect of the nanosphere on the dynamics is shown to be noticeable for the charged-molecule case.

---

---

# Zusammenfassung

Das Verständnis der fundamentalen Prozesse, welche die Effizienz des elektronischen Anregungsenergietransfers in photosynthetischen Lichtsammelkomplexen bestimmen, ist von großer Bedeutung für das Design neuartiger Materialien zur Nutzung der Solarenergie. In den vergangenen Jahren hat es sich herausgestellt, dass Quantenkohärenz im Zusammenspiel mit der Elektron-Schwingungswechselwirkung an dieser Stelle eine entscheidende Rolle spielt. In der vorliegenden Arbeit wurde der Zugang der Quanten-Master-Gleichung genutzt, um die Dynamik im Fenna-Matthews-Olson Komplex zu untersuchen. Besondere Aufmerksamkeit wurde dabei auf Effekte von explizit berücksichtigten Schwingungen gelegt. Zwei Näherungen wurden gegenübergestellt und mit einem rein exzitonischen Modell verglichen. Resultate zeigen, dass (i) die explizite Berücksichtigung von Schwingungen einen erheblichen Einfluss auf die Population des Reaktionszentrums hat und (ii) Ein- und Zweiteilchennäherungen in der Exziton-Schwingungsbasis zu qualitativ unterschiedlichen Ergebnissen führen. In einer zweiten Anwendung wurde ein exzitonisches Modell für den LH2 Antennenkomplex der Bakterienform *Alc. vinosum* untersucht. Im Zentrum stand dabei die Erklärung der ungewöhnlichen Form der B800 Absorptionsbande und deren Beziehung zu den beobachteten Exziton-Relaxationsraten. Es zeigte sich, dass insbesondere die spezielle Anordnung der Dipolmomente sowie die für B800 und B850 Pigmente spezifischen Relaxationsraten wichtig sind.

Im zweiten Teil der Arbeit wurden Hybridsysteme aus Metallnanokugeln und Farbstoffaggregaten untersucht. Dazu wurde ein Dichtefunktionaltheorie-basierter *tight-binding* Zugang genutzt, der eine diskrete Darstellung quantenmechanischer elektronischer Ladungsdichten erlaubt. Diese Ladungen wurden selbstkonsistent an das klassische Polarisationsfeld der Nanokugel gekoppelt. Besondere Aufmerksamkeit wurde dem statischen Fall gewidmet, wobei der Einfluss von Systemparametern wie dem Radius der Nanokugel, der Molekülladung sowie dem Abstand analysiert wurden. Es zeigte sich unter anderem, dass die Abstandsabhängigkeit der Wechselwirkungsenergie durch die Ladung des Moleküls in nicht-trivialer Weise bestimmt wird.

Abschließend wurde die Anregung eines Hybridsystems mit einem externen Laserfeld beschrieben. Für ein Aggregat ergibt dies ein zusätzliches Nahfeld, das insbesondere auf das unmittelbar zur Nanokugel benachbarte Molekül einwirkt. Der Effekt der Polarisation auf die Dynamik ist für geladene Moleküle besonders ausgeprägt. Im Rahmen der Untersuchungen wurden schließlich Bedingungen identifiziert, unter denen das Hybridsystem mit einem effektiven Einteilchenmodell beschrieben werden kann.

---



---

# Contents

<b>I</b>	<b>Introduction</b>	<b>1</b>
1	Photosynthetic Light-Harvesting . . . . .	1
2	Nanostructures . . . . .	4
3	Goals of this Thesis . . . . .	5
<b>II</b>	<b>Theoretical Background</b>	<b>7</b>
1	Molecular Hamiltonian . . . . .	7
2	Excitation Energy Transfer . . . . .	9
2.1	Frenkel Exciton Hamiltonian . . . . .	9
2.2	System-Bath Approach and Redfield Equations of Motion . . . . .	13
3	The Polarization-Field of a Spherical Nanoparticle . . . . .	18
4	DFTB-Based Calculation of Electronic States . . . . .	22
4.1	SCC-DFTB Theory in Time-independent Constant External Field . . . . .	22
4.2	Approximate TDDFT in an External Field . . . . .	28
<b>III</b>	<b>Dissipative Exciton Dynamics in LH Complexes</b>	<b>31</b>
1	Vibrational and Vibronic Coherences in FMO Complex . . . . .	31
1.1	FMO Model . . . . .	32
1.2	Results . . . . .	36
2	LH2 of <i>Alc. vinosum</i> : B800 Band Splitting . . . . .	46
2.1	Model System . . . . .	46
2.2	Results . . . . .	50
<b>IV</b>	<b>Polarization Effects and Exciton Dynamics in Hybrid Systems</b>	<b>57</b>
1	Static Case . . . . .	57
1.1	Model Systems . . . . .	57
1.2	Results . . . . .	60
2	External Field Driven Dynamics . . . . .	70
2.1	Model System . . . . .	70
2.2	Dynamics of the Molecule Nearest to the NS . . . . .	72
2.3	Exciton Dynamics in a Model Aggregate . . . . .	78
<b>V</b>	<b>Conclusions and Outlook</b>	<b>83</b>



---

# List of Abbreviations

2DES	Two-Dimensional Electronic Spectroscopy
BChl	Bacteriochlorophyll
CCY	Cationic Carbocyanine
Chl	Chlorophyll
DFT	Density-Functional Theory
DFTB	Density-Functional Tight-Binding
DOF	Degree Of the Freedom
EET	Excitation Energy Transfer
EVC	Exciton-Vibrational Coupling
FC	Franck-Condon
FMO	Fenna-Matthews-Olson
KS	Kohn-Sham
LCAO	Linear Combination of Atomic Orbitals
LH1	core reaction-centre LHCs
LH2	the peripheral antenna complex of purple bacteria
LHC	Light-Harvesting Complex
NS	Nanosphere
OPA	One-Particle Approximation
PPC	Pigment-Protein Complex
QM	Quantum Mechanical
QME	Quantum Master Equation
RC	Reaction Center
RDM	Reduced Density Matrix
RDO	Reduced Density Operator
SCC	Self-Consistent-Charge
SCC-DFTB	Self-Consistent-Charge Density-Functional Tight-Binding
SERS	Surface-Enhanced Raman Spectroscopy
TDDFT	Time-Dependent Density-Functional Theory
TDKS	Time-Dependent Kohn-Sham
TET	Tetracene
TPA	Two-Particle Approximation
XC	Exchange-Correlation



---

# Chapter I

## Introduction

### 1 PHOTOSYNTHETIC LIGHT-HARVESTING

Every day sunlight supports the activities of all life on earth. Even though solar thermal collectors and solar panels are widely used, the photosynthetic organisms are still the largest energy producers. Solar-energy capture, transfer and conversion are the most important processes in photosynthetic organisms. Photosynthetic organisms contain light-harvesting complexes (LHCs) and the reaction center (RC). LHCs are the sophisticated pigment-protein complexes (PPCs), which surround the photosystem's RC. LHCs are important models for the research on photosynthetic efficiency, protection and acclimation, since they have evolved to capture photons and perform excitation energy transfer (EET) to the RC on a 10-100 picosecond time scale with high efficiency [1, 2, 3]. LHCs consist of several chromophores (sites) mutually coupled by dipole interactions and embedded in a protein environment. Due to their coupling, light induced excitations can undergo energy transfer from site to site towards the RC. In the RC the excitation energy triggers the conversion to chemical energy [4]. During this process, the conversion from light to photosynthetic energy can reach very high efficiency (conversion for initial processes >95%) [5], much higher than that in solar thermal collectors or solar panels.

There are only four classes of chromophores used for photosynthetic organisms: chlorophylls (Chls) and bacteriochlorophylls (BChls), phycobilins, and carotenoids. The chromophores are bound to proteins, which are mostly from seven major protein families, i.e. the core complex family, chlorosomes, phycobilisomes, the Fenna-Matthews-Olson (FMO) proteins, the protobacterial antenna complexes, the LHCs superfamily, and the preidinin-Chl *a* protein. In fact, Chls, BChls, phycobilins and carotenoids all absorb sunlight very strongly. Chls have strong absorption bands in the blue and red regions of the spectrum. In Chls, Chl *a* has bands peaking near 380 and 780 nm, and Chl *b* near 460 and 650 nm. BChls have similar absorption bands and intense absorption strength as Chls. For example, a 0.1 mM solution of BChl *a* in 1 cm cuvette can absorb about 99% of the energy in a 770 nm light beam [4].

LHCs are contained in green, purple bacteria and so on. The green and purple bacteria are anoxygenic phototrophs, i.e. anoxic conditions are required for phototrophic growth. They participate in the anoxic cycling of carbon as primary producers and light-stimulated consumers. Green bacteria have large cigar-shaped complexes appressed to the surface of the cytoplasmic membrane and they are two families: green sulfur bacteria (Chlorobiaceae) [6] and green non-

sulfur bacteria (Chloroflexaceae) [7]. The FMO is a water-soluble protein and only found in the green sulfur bacteria. It transfers the excitation energy from chlorosome to the RC. FMO has been the first crystallized chlorophyll-protein with a high resolution structure as reported by the Matthews group in 1979 [8]. In their work, FMO consists of three monomers, each of which contains seven BChls  $a$ . However, the location of the FMO protein in the green sulfur bacteria is still uncertain. For example, the FMO is modelled as a layer between the chlorosome baseplate and the RC [9] or embedded in the lipid bilayer near by the RC [10]. And in 2009, the eighth BChl  $a$  was revealed in the structures of the FMO [11]. Although very weakly coupled with other BChls  $a$ , this eighth BChl  $a$  is believed to act as a linker between the chlorosome and the other monomers [12].

The purple bacteria are composed by BChl  $a,b$  and various carotenoids. They are easy to cultivate and best understood of all LHCs. The protobacterial antenna complexes for many photosynthetic purple bacteria are composed by larger core reaction-centre LHCs (LH1) and the peripheral antenna complex of purple bacteria (LH2). The LH1 forms a ring of 16-fold symmetry and has only a single absorption maximum around 875 nm. LH2 is the main part for absorbing the sun light and rapidly transfer the energy via LH1 to the RC. The LH2s are ring-like oligomers formed by  $\alpha$ -polypeptides and  $\beta$ -polypeptides, which non-covalently bind three BChls  $a$  and one carotenoid. Carotenoids are chromophores which act as antioxidant agents, absorb in the blue-green region light and transfer the excitation energy to BChls. A special feature of the LH2 is that the BChl  $a$  molecules are arranged in two concentric rings with a common symmetry axis perpendicular to the plane of the rings. One ring consists of weakly interacting BChl  $a$  molecules (B800) with the absorption band around 800 nm. And the other is composed by a group of strongly interacting BChl  $a$  (B850) in near van der Waals contact with an absorption band around 850 nm.

The first high-resolution crystal structure was solved by McDermott and co-workers for the bacterium *Rhodospseudomonas acidophila* (*Rps. acidophila*) in 1995 [13] with 9 subunits. In the following, the bacterium *Rhodospirillum molischanum* (*Rsp. molischanum*) with 8 subunits was cultivated by Koepke et al. in 1996 [14]. The high-light LH2 from *Allochromatium vinosum* (*Alc. vinosum*) was reported by Sami Kereïche et al. in 2008 [15]. It features an unusual spectrum where the B800 band is split into a doublet. The antenna for this type is assumed to contain 12 subunits as concluded from ensemble circular dichroism spectroscopy and polarisation-resolved single-molecule spectroscopy [16].

EET is the energy transfer between different molecules by the coupling of electronic excitations and also called fluorescence resonance energy transfer. Fig. I.1 a shows EET process in the general scheme. D represents the excitation energy donor and A is the excitation energy acceptor. At the beginning, the donor molecule has been excited and the acceptor molecule is in its ground state. Then due to the Coulomb interaction  $J_{DA}$  between the donor and acceptor, the excitation energy is transferred to the acceptor molecule, i.e. the donor molecule is deexcited and the acceptor molecule is excited at the end. Fig. I.1 b shows the same system including vibrational states. During this process, the donor is deexcited from excited state with vibrational quantum number  $M_{eD}$  to ground state with  $N_{gD}$  and the acceptor is excited from ground state with  $N_{gA}$  to the excited state  $M_{eA}$ . In this case, the Coulomb coupling between the molecules

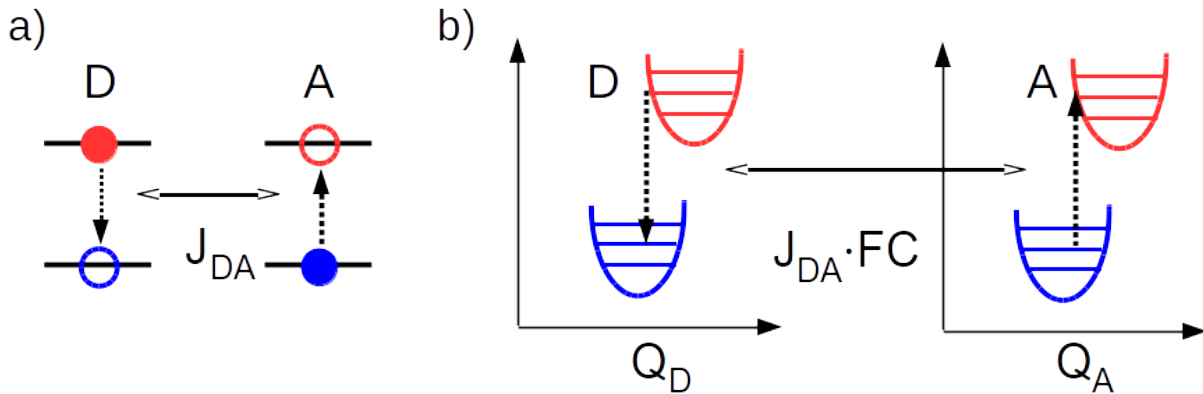


Figure I.1: Schematic of EET between a donor molecule D and an acceptor A. a) the general case with the Coulomb interaction  $J_{DA}$ . b) the scheme with exciton-vibrational coupling. FC is the FC overlap integral.

is  $J_{DA} \cdot FC$ , where the Franck-Condon (FC) overlap integral between the vibrational states has been introduced.

EET has been of interest for decades, not only in the quest for very high efficiency but also as a widely used tool to study the structure and dynamics in photosynthesis systems, such as the FMO complex [17] and LH2 [18, 19, 20, 21, 22]. The early theory for a rate description was introduced by Förster in 1946 [23, 24]. In the Förster theory, the interaction between the donor and acceptor  $J_{DA}$  is treated as the interaction between two oscillating electric dipoles and the EET rate yields

$$k_{\text{EET}}^{\text{Förster}} = \frac{1}{\tau_D} \left( \frac{R_0}{R_{DA}} \right)^6 \quad (\text{I.1})$$

where  $R_{DA}$  is the distance between the donor and acceptor,  $\tau_D$  represents the fluorescence lifetime of the donor, and  $R_0$  is the Förster radius, which depends on the fluorescence yields of the donor, the overlap between the emission spectra of the donor and the absorption spectra of the acceptor, and the relative orientation. All the factors can be accessed in the experiment [25]. The first experiment was made by H. J. Dutton and his coworkers in 1943, which observed EET from fucoxanthin to Chl *a* in a dimer using monochromatic excitation [26]. But the Förster theory is limited to weak coupling  $J_{DA}$  and the surrounding environment is assumed to be homogeneous to get the Förster radius  $R_0$ .

When the coupling for EET is sufficiently large, a quantum-mechanical (QM) superposition state may be formed, which is known as Frenkel exciton. In Frenkel theory, the Frenkel exciton represents an electron-hole pair at the same molecule, i.e. the Frenkel exciton is local, but upon the coupling the Frenkel exciton state is delocalized. Frenkel excitons occur in associated and noncovalent supramolecular complexes. For decades, Frenkel exciton theory is used for the description of EET in photosynthetic antenna.

Exciton-vibrational coupling (EVC) exists in all EET processes in real systems. However owing to the smallness of the FC coupling for BChl and limitation of experimental technology, EVC was long considered to guarantee directed downhill energy transfer only. But in the recent years by applying the two-dimensional electronic spectroscopy (2DES) long-lasting quantum

coherence was observed in several LHCs both at cryogenic temperature [27, 28, 29] and room temperature [30, 31]. Then it was realized that quantum coherence involving EVC may play an important role in the high efficiency energy transfer process [32, 33, 34]. Therefore during recent years, the impact of EVC according to the model in Fig. I.1 b on the dynamics of biological systems beyond the role of a heat bath has triggered more and more interest [35]. For example, based on theoretical calculation, Nalbach and coworkers predicted that the transfer towards the RC in the FMO complex at 300 K is speed up by 24% if specific vibrations are taken into account [36].

## 2 NANOSTRUCTURES

Nanostructures have at least one dimension less than 100 nm and are widely studied because of site-dependent physical and chemical properties. The applications include optical systems, catalysis, optical data communication and storage, etc. Nanoparticles have unique electronic, magnetic, optical and other important material properties which are applied in molecular sensing, catalysis and biological technologies. For example, the optical properties of nanoparticles can be tuned gradually by their size and shape. The nanoparticle-based composites have both the specific characteristics of the individual nanoparticles [37, 38] and of the total structure (e.g. periodic arrangement) [39, 40]. Semiconductor nanoparticles have been already used successfully as solar cells for converting sunlight to electricity [41].

An applied external field can cause the delocalized electrons at the surface of the nanoparticles to oscillate, which is called a surface plasmon. When the induced electric field resonates with the external field, surface plasmon resonance occurs. Especially if the size of the nanoparticle is smaller than the wavelength of the light, the surface plasmon resonance can cause different field distributions near the surface, which is considered as a kind of polarization and called localized surface plasmon resonance [42]. Such near-fields with nanometer spatial resolution can be controlled by localized electronic processes. Popular examples that utilize this scheme include surface-enhanced Raman spectroscopy (SERS), where Raman scattering from the surface adsorbates is extremely enhanced by near-fields generated at surface roughnesses [43] or in the adjacent metal clusters and nanoparticles [44, 45, 46]. It is worth noting that SERS is not limited to stationary spectroscopy, and ultrafast nonlinear SERS is used as a tool to study molecular dynamics with unprecedented sensitivity [47].

Nanoparticles are much smaller than everyday objects described by Newton's laws of motion, but larger than single atoms or molecules and it is too expensive to compute all the dynamics using quantum mechanics. Several theoretical models have been proposed to understand the behavior of nanoparticle-organic hybrid systems [48, 49, 50]. For a few cases, the nanoparticles have been described by QM methods [51, 52], however, here nanoparticle sizes are much smaller than those of practical interest. For this reason different groups devised approximate models to use a QM description for the molecule, but a classical electromagnetic description for the nanoparticles either as a continuous dielectric [53, 46, 54, 55, 56] or a collection of polarizable atoms [57, 58, 59]. In fact, a nanostructure brought into close proximity of a molecule will not only enhance the field of an incident external laser pulse, but also react on the presence of the molecular charge density via an additional polarization field. In principle the theoretical



description would require to solve Maxwell's equations for the fields, self-consistently with the Schrödinger equation for the material system nanostructure plus molecule. Since this is far from being feasible for any real system, various approximations have been developed.

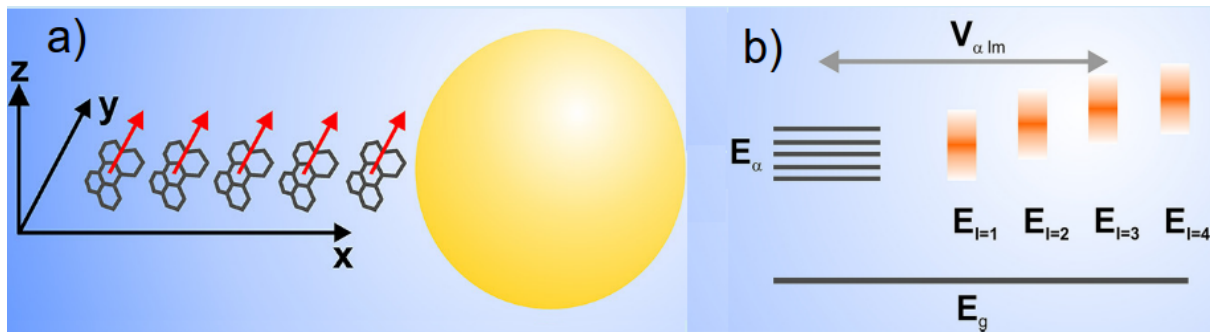


Figure I.2: a) Scheme of a molecular aggregate-NS system with the transition dipole moments drawn as red arrows. b) Energy level scheme of the aggregate-NS system.  $E_g$  is the aggregate-NS ground state,  $E_\alpha$  are the exciton energies and  $E_l$  refers to the multipole excitation (whole set  $m = -l, \dots, l$ ) of the metal NS with broadened levels (orange) reflecting their short lifetime. They are connected via coupling  $V_{\alpha,lm}$ . Reprinted with permission from Y. Zelinsky, Y. Zhang, and V. May, Supramolecular complex coupled to a metal nanoparticle: computational studies on the optical absorption, *J. Phys. Chem. A*, 116, 11330 (2012). Copyright 2012 by the American Chemical Society.

For instance in ref. [60], May and coworkers used a fully QM description based on model Hamiltonians for the considered metal nanosphere (NS) interacting with a molecular aggregate. The aggregate-NS and energy level scheme is shown in Fig. I.2. One finds the arrangement of the aggregate in the model (cf. Fig. I.2 a) being strictly linear. In the theory, they assumed the conduction band electrons of the metal NS interact strongly with the transitions in the aggregate. As in Fig. I.2 b, the aggregate system is described in single-excited state representation, which means that the aggregate Hamiltonian is directly expanded in the relevant molecular electronic states without the effect of the metal NS. Ground  $|E_g\rangle$  and excited aggregate states  $|E_\alpha\rangle$  are shown in Fig. I.2 b. The Hamiltonian of the metal NS has been represented in a collective plasmon excitation approximation. Then based on Mie theory and multipole expansion for metal NS, the NS Hamiltonian is finally described by energies  $E_{lm}$  with multipolar indices  $l, m$  as shown in Fig. I.2 b. The coupling between aggregate and metal NS  $V_{\alpha,lm}$  is calculated by the transition dipole moments of the aggregate and the metal NS. Then the aggregate-NS system is propagated in density matrix theory treating plasmon decay and EVC by dephasing rates. Special attention has been paid to the absorption line shape for the hybrid system.

Although this type of microscopic model has been proven to provide valuable insight in a numbers of applications [61, 62, 63], it lacks a self-consistent description of the coupled NS-aggregate system.

### 3 GOALS OF THIS THESIS

EET plays an important role in photosynthetic systems and hybrid system composed of nanoparticles and assemblies of dye molecules. In this work, I focus on various processes affecting EET

in the photosynthetic and NS-organic hybrid systems.

In Section III.1, the EET dynamics, especially coupled exciton-vibrational dynamics, are investigated in the FMO complex using a quantum master equation (QME) approach. Different approximations to the EVC basis are used to analyse the vibronic and vibrational effects on EET. Further the cause and effects of the B800 band splitting in the LH2 of *Alc. vinosum* is investigated in Section III.2.

In Chapter IV, hybrid systems of a NS and different molecules are studied in a semiclassical self-consistent method. Here, the near-field of the NS due to the molecule is studied in classical multipole expansion. Placing different dye molecules in the vicinity of the NS, the mutual electronic polarization is investigated using the Self-Consistent-Charge Density-Functional Tight-Binding (SCC-DFTB) method in Section IV.1. Finally the effect of an additional external field driving electronic excitation dynamics is investigated in Section IV.2.

---

## Chapter II

# Theoretical Background

This chapter presents the basic theory. The first section discusses the molecular Hamiltonian. Subsequently, the second section focusses on the transfer of electronic excitation energy. The effect of NS on the electronic properties of molecules are discussed in the third section. The Density-Functional Tight-Binding (DFTB) method is introduced in the last section (All the equations below are in the atomic units unless mentioned otherwise).

### 1 MOLECULAR HAMILTONIAN

The molecular Hamiltonian is introduced and the stationary Schrödinger equation is formulated by separating the electronic and nuclear degrees of freedom (DOFs) using the Born-Oppenheimer approximation [64].

Let us consider a molecule composed of  $N_n$  nuclei with the atomic number  $Z_1, \dots, Z_{N_n}$ , coordinates  $\vec{R}_k$ , momenta  $\vec{P}_k$  and  $N_e$  electrons with the Cartesian coordinates  $\vec{r}_i$  and conjugate momenta  $\vec{p}_i$ . The Hamiltonian operator of the molecule yields the Schrödinger equation

$$H_{\text{mol}}\Phi(\vec{r}, \vec{R}) = (T_e + V_{ee} + V_{en} + T_n + V_{nn})\Phi(\vec{r}, \vec{R}) = \varepsilon\Phi(\vec{r}, \vec{R}) \quad (\text{II.1})$$

where the kinetic energies of the electrons and nuclei are

$$T_e = \sum_{i=1}^{N_e} \frac{\vec{p}_i^2}{2} \quad (\text{II.2})$$

$$T_n = \sum_{k=1}^{N_n} \frac{\vec{P}_k^2}{2M_k} \quad (\text{II.3})$$

with  $M_k$  being the mass of the  $k$ th nucleus. Since both kinds of particles interact via Coulomb forces, the repulsive interactions in Eq. (II.1) become

$$V_{ee} = \frac{1}{2} \sum_{i \neq j} \frac{1}{|\vec{r}_i - \vec{r}_j|} \quad (\text{II.4})$$

$$V_{nn} = \frac{1}{2} \sum_{k \neq l} \frac{Z_k Z_l}{|\vec{R}_k - \vec{R}_l|} \quad (\text{II.5})$$

and the attractive interaction in Eq. (II.1) is

$$V_{en} = - \sum_{j,k} \frac{Z_k}{|\vec{r}_j - \vec{R}_k|} \quad (\text{II.6})$$

Due to the large mass difference between electrons,  $m_e$ , and nuclei,  $M_k$  ( $m_e/M_k < 10^{-3}$ ), one can expect that the electrons move much faster than the nuclei on average. Therefore, in many situations the electronic motions are assumed to respond instantaneously to any changes in the nuclear configuration, i.e. the electronic wave function can be described by stationary states. In other words, the electronic wavefunction evolves adiabatically with nuclear configuration, i.e. there are no transitions between different stationary states. Thus, it is reasonable to define an electronic Schrödinger Hamiltonian which parametrically depends on the nuclear coordinate:

$$H_e(\vec{R})\Psi_a(\vec{r}; \vec{R}) = (T_e + V_{ee} + V_{en})\Psi_a(\vec{r}; \vec{R}) = E_a(\vec{R})\Psi_a(\vec{r}; \vec{R}) \quad (\text{II.7})$$

Hence, the molecular wave function for Eq. (II.1) can be expanded in the basis as

$$\Phi(\vec{r}, \vec{R}) = \sum_a \chi_a(\vec{R})\Psi_a(\vec{r}; \vec{R}) \quad (\text{II.8})$$

where  $\chi_a(\vec{R})$  depends on the configuration of the nuclei. Inserting Eq. (II.8) into Eq. (II.1), one obtains

$$\begin{aligned} H_{\text{mol}}\Phi(\vec{r}, \vec{R}) &= [H_e(\vec{R}) + T_n + V_{nn}] \sum_a \chi_a(\vec{R})\Psi_a(\vec{r}; \vec{R}) \\ &= \sum_a [E_a(\vec{R}) + V_{nn}] \chi_a(\vec{R})\Psi_a(\vec{r}; \vec{R}) + \sum_a T_n \chi_a(\vec{R})\Psi_a(\vec{r}; \vec{R}) \\ &= \varepsilon \sum_a \chi_a(\vec{R})\Psi_a(\vec{r}; \vec{R}) \end{aligned} \quad (\text{II.9})$$

Using the orthogonality of the adiabatic basis, multiplication from the left by  $\Psi_b^*(\vec{r}; \vec{R})$  and integration yields

$$\begin{aligned} \int \Psi_b^*(\vec{r}; \vec{R}) H_{\text{mol}} \Psi_a(\vec{r}; \vec{R}) &= [E_b(\vec{R}) + V_{nn}] \chi_b(\vec{R}) + \sum_a \int \Psi_b^*(\vec{r}; \vec{R}) T_n \Psi_a(\vec{r}; \vec{R}) \chi_a(\vec{R}) \\ &= \varepsilon \chi_b(\vec{R}) \end{aligned} \quad (\text{II.10})$$

Considering that the electronic wave functions depend on the nuclear coordinates, one obtains by the product rule for differentiation

$$\begin{aligned} T_n \Psi_a(\vec{r}; \vec{R}) \chi_a(\vec{R}) &= \sum_k \frac{1}{2M_k} \left\{ [\vec{P}_k^2 \Psi_a(\vec{r}; \vec{R})] \chi_a(\vec{R}) + 2[\vec{P}_k \Psi_a(\vec{r}; \vec{R})] \vec{P}_k \chi_a(\vec{R}) \right. \\ &\quad \left. + \Psi_a(\vec{r}; \vec{R}) \vec{P}_k^2 \chi_a(\vec{R}) \right\} \end{aligned} \quad (\text{II.11})$$

Since the last term is simply the kinetic energy operator acting on  $\chi_a(\vec{R})$ , one can define the

other terms as so-called nonadiabaticity operator

$$\Theta_{ab} = \int \Psi_a(\vec{r}; \vec{R}) T_n \Psi_b(\vec{r}; \vec{R}) + \sum_k \frac{1}{M_k} \left[ \int \Psi_a(\vec{r}; \vec{R}) \vec{P}_k \Psi_b(\vec{r}; \vec{R}) \right] \vec{P}_n \quad (\text{II.12})$$

Thus, one can obtain an equation for  $\chi_a(\vec{R})$  from Eq. (II.11):

$$\left[ T_n + E_a(\vec{R}) + V_{nn} + \Theta_{aa} - \varepsilon \right] \chi_a(\vec{R}) = - \sum_{b \neq a} \Theta_{ab} \chi_b(\vec{R}) \quad (\text{II.13})$$

This result can be interpreted as the stationary Schrödinger equation for the motion of nuclei, with the respective wave functions  $\chi_a(\vec{R})$ . The solution to Eq. (II.13) requires to know the electronic spectrum for all configurations of the nuclei. Due to the electronic nonadiabatic coupling  $\Theta_{ab}$ , transitions between individual adiabatic electronic states become possible.  $\Theta_{ab}$  is a consequence of the nuclear motions which enter by their momentum as Eq. (II.12). In fact, the diagonal part  $\Theta_{aa}$  is usually a small perturbation to the nuclear dynamics in a given electronic state.

However often, it is possible to neglect the nonadiabatic coupling  $\Theta_{ab}$ , which is called Born-Oppenheimer approximation. Thus, the nuclear Schrödinger equation for the states  $|\Psi_a\rangle$  reads

$$H_a(\vec{R}) \chi_a(\vec{R}) = \left[ T_n + U_a(\vec{R}) \right] \chi_a(\vec{R}) = \varepsilon \chi_a(\vec{R}) \quad (\text{II.14})$$

and the adiabatic molecular wavefunction is

$$\Phi(\vec{r}, \vec{R}) = \chi_a(\vec{R}) \Psi_a(\vec{r}; \vec{R}) \quad (\text{II.15})$$

Here the potential energy surface for the nuclear motion is introduced when the electronic system is in its adiabatic state  $|\Psi_a\rangle$ :

$$U_a(\vec{R}) = E_a(\vec{R}) + V_{nn}(\vec{R}) \quad (\text{II.16})$$

## 2 EXCITATION ENERGY TRANSFER

The excitation energy delocalization and transfer are explained in the so-called Frenkel exciton model. In this model, the moving excitation energy is completely represented by an intramolecular excitation and there is no charge transfer between different molecules. The interaction of the exciton system with the mentioned bath is described by a QME [64].

### 2.1 FRENKEL EXCITON HAMILTONIAN

The aggregate Hamiltonian is given by the Frenkel exciton Hamiltonian, which is based on the assumption that the interacting sites (i.e. monomers) retain their chemical identity. Hence the site adiabatic states  $|a_m\rangle = |\Psi_{a,m}\rangle$  can be used to represent the diabatic monomeric states and the inter-site Coulomb coupling. Here,  $a = g, e$  is the monomeric adiabatic electronic state and  $m = 1, \dots, N$  labels the site of the aggregate. If only considering situations up to a single

excitation, the ground state  $|g\rangle$  and the one-exciton states  $|m\rangle$  of the aggregate are given by

$$|g\rangle = \prod_m |g_m\rangle, \quad |m\rangle = |e_m\rangle \prod_{n \neq m} |g_n\rangle \quad (\text{II.17})$$

Of course, higher-order excitations, such as higher excited adiabatic states or multiple excitations at different sites, can be incorporated similarly into the description. Including the ground state and one-exciton states, the Frenkel Hamiltonian is

$$H_{\text{agg}} = H_g |g\rangle \langle g| + \sum_m H_m |m\rangle \langle m| + \sum_{m \neq n} J_{mn} |m\rangle \langle n| + H_{\text{field}}(t) \quad (\text{II.18})$$

Here, the coupling element  $J_{mn}$  is the interaction between different exciton states and  $H_{\text{field}}(t)$  represents the interaction with external fields.

The interaction between different one-exciton states is given by the Coulomb integral (Here and in the following  $\int d\vec{r}'$  is abbreviated as  $\int'$ , and  $\int d\vec{r}$  as  $\int$ )

$$J_{mn} = \iint' \frac{\mathcal{N}_{ab}^{(m)}(\vec{r}) \mathcal{N}_{cd}^{(n)}(\vec{r}')}{|\vec{r} - \vec{r}'|} \quad (\text{II.19})$$

Here  $\vec{r}$  is an electronic coordinate and  $\mathcal{N}$  denotes the generalised molecular charge density [64] where electrons and nuclei contribute according to

$$\mathcal{N}_{ab}^{(m)}(\vec{r}) = \rho_{ab}^{(m)}(\vec{r}) - \delta_{ab} \sum_{A \in m} Z_A \delta(\vec{r} - \vec{R}_A) \quad (\text{II.20})$$

with the electronic density

$$\rho_{ab}^{(m)}(\vec{r}) = \langle a_m | n(\vec{r}) | b_m \rangle = N_m \langle a_m | b_m \rangle \quad (\text{II.21})$$

where  $n(\vec{r})$  is the one-particle electron density operator and  $N_m$  is the number of electrons for molecule  $m$ .

In fact, often the intramolecular distance is much larger than the extension of the electron-nuclei densities  $\mathcal{N}(\vec{r})$ . Thus, a dipole-dipole approximation can be used to simplify Eq. (II.19). Defining the mass center of the molecule  $m$  as  $\vec{r}_m$  and the extension of the electron-nuclei density as  $\vec{x}$ , the term  $1/|\vec{r} - \vec{r}'|$  from Eq. (II.19) could be replaced by  $1/|\vec{r}_m - \vec{r}_n + \vec{x} - \vec{x}'|$ . If  $|\vec{X}|/|r| \ll 1$ , the term  $1/|\vec{r} + \vec{X}|$  can be expanded as

$$\begin{aligned} \frac{1}{|\vec{r} + \vec{X}|} &= \frac{1}{|\vec{r}|} + \vec{X} \nabla_r \frac{1}{|\vec{r}|} + \frac{1}{2} (\vec{X} \nabla_r) (\vec{X} \nabla_r) \frac{1}{|\vec{r}|} + o\left(\frac{|\vec{X}|}{|r|}\right)^3 \\ &= \frac{1}{|\vec{r}|} - \frac{\vec{X} \vec{r}}{|\vec{r}|^3} - \frac{\vec{X}^2}{2|\vec{r}|^3} + \frac{3(\vec{X} \vec{r})^2}{2|\vec{r}|^5} + o\left(\frac{|\vec{X}|}{|r|}\right)^3 \end{aligned} \quad (\text{II.22})$$

Assuming  $\vec{r} = \vec{r}_{mn} = \vec{r}_m - \vec{r}_n$  and  $\vec{X} = \vec{x} - \vec{x}'$  in Eq. (II.22) and considering the charge

neutrality, Eq. (II.19) is expanded in the second-order as

$$J_{mn} \approx \iint d\vec{x} d\vec{x}' \mathcal{N}_{ab}^{(m)}(\vec{x} + \vec{r}_m) \mathcal{N}_{cd}^{(n)}(\vec{x}' + \vec{r}_n) \left[ \frac{\vec{x}\vec{x}'}{|\vec{r}_{mn}|^3} - \frac{3(\vec{x}\vec{r}_{mn})(\vec{x}'\vec{r}_{mn})}{|\vec{r}_{mn}|^5} \right] \quad (\text{II.23})$$

Set the transition dipole moment as

$$\vec{\mu}_{mab} = \int \vec{r} \mathcal{N}_{ab}^{(m)}(\vec{r}) = \int \vec{r} \rho_{ab}^{(m)}(\vec{r}) - \delta_{ab} \sum_{A \in m} Z_A \vec{R}_A \quad (\text{II.24})$$

one can obtain the Coulomb coupling in dipole-dipole approximation by the transition dipole moment

$$J_{mn} \approx \frac{\vec{\mu}_{m,ab} \vec{\mu}_{n,cd}}{|\vec{r}_{mn}|^3} - 3 \frac{(\vec{r}_{mn} \vec{\mu}_{m,ab})(\vec{r}_{mn} \vec{\mu}_{n,cd})}{|\vec{r}_{mn}|^5} \quad (\text{II.25})$$

In dipole approximation, the last term in Eq. (II.18) is given by

$$H_{\text{field}}(t) = -\vec{\mu} \cdot \vec{E}_{\text{ext}}(t) \quad (\text{II.26})$$

with the external laser field  $\vec{E}_{\text{ext}}$  and the total transition dipole for the considered two level case is

$$\vec{\mu} = \sum_m \mu_{m,ge} |m\rangle \langle g| + \text{h.c.} \quad (\text{II.27})$$

In Eq. (II.18), the adiabatic states should depend on the intra-molecular nuclear coordinates  $R = (\vec{R}_1, \vec{R}_2, \dots)$ , i.e.  $|m\rangle = |m(R)\rangle$ . The  $H_g$  and  $H_m$  are given by the electronic state energy and a contribution representing potential energy and kinetic energy of the nuclei. Then the corresponding on-site elements of the system Hamiltonian are given by

$$\begin{aligned} H_g(R) &= E_g + U_g(R) + T_g \\ H_m(R) &= E_m + U_m(R) + T_m \end{aligned} \quad (\text{II.28})$$

Here  $E_g$  and  $E_m$  are the bare electronic energy for state  $|g\rangle$  and  $|m\rangle$ . In the second order Taylor expansion of the potential energy around its minimum with respect to  $R$ , combined with a normal mode transformation yields the harmonic oscillator model (assuming a description in terms of ground state models and no Dushinsky notation)

$$\begin{aligned} H_g(q) &= E_g + \frac{1}{2} \sum_m \sum_{\xi} (p_{\xi,m}^2 + \omega_{\xi,m}^2 q_{\xi,m}^2) \\ H_m(q) &= E_m + \frac{1}{2} \sum_{n \neq m} \sum_{\xi} (p_{\xi,n}^2 + \omega_{\xi,n}^2 q_{\xi,n}^2) + \frac{1}{2} \sum_{\xi} (p_{\xi,m}^2 + \omega_{\xi,m}^2 (q_{\xi,m} - d_{\xi,m})^2) \end{aligned} \quad (\text{II.29})$$

with  $p_{\xi,m}^2$  and  $\omega_{\xi,m}^2$  are the momentum and the harmonic frequency associated with the  $\xi$ th mode of monomer  $m$ , the relevant normal coordinate  $q_{\xi,m}$  and  $d_{\xi,m}$  represents the shift of the excited state oscillator along  $q_{\xi,m}$  with respect to the ground state potential energy surface. Note that the normal coordinates are mass-weighted. Introducing intrinsic harmonic oscillator variables,

$$\tilde{p}_{\xi,m} = \sqrt{\frac{1}{\omega_{\xi,m}}} p_{\xi,m}, \quad \tilde{q}_{\xi,m} = \sqrt{\omega_{\xi,m}} q_{\xi,m} \quad (\text{II.30})$$

gives

$$\begin{aligned}
 H_g(\tilde{q}) &= E_g + \sum_m \sum_{\xi} \frac{\omega_{\xi,m}}{2} (\tilde{p}_{\xi,m}^2 + \tilde{q}_{\xi,m}^2) \\
 H_m(\tilde{q}) &= E_m + \sum_{n \neq m} \sum_{\xi} \frac{\omega_{\xi,n}}{2} (\tilde{p}_{\xi,n}^2 + \tilde{q}_{\xi,n}^2) + \sum_{\xi} \frac{\omega_{\xi,m}}{2} (\tilde{p}_{\xi,m}^2 + (\tilde{q}_{\xi,m} - \tilde{d}_{\xi,m})^2)
 \end{aligned} \tag{II.31}$$

The dimensionless shift  $\tilde{d}_{\xi,m}$  can be represented by the Huang-Rhys factor  $S_{\xi,m} \equiv \tilde{d}_{\xi,m}^2/2$ . Then the one-exciton Hamiltonian can be expanded as

$$H_m(\tilde{q}) = E_m + \sum_n \sum_{\xi} \frac{\omega_{\xi,n}}{2} (\tilde{p}_{\xi,n}^2 + \tilde{q}_{\xi,n}^2) - \sum_{\xi} \omega_{\xi,m} \sqrt{2S_{\xi,m}} \tilde{q}_{\xi,m} + \sum_{\xi} \omega_{\xi,m} S_{\xi,m} \tag{II.32}$$

In this equation, the last term is the reorganization energy for the relaxation in the excited state after a vertical transition from the ground state. Thus, it is related to the Stokes shift in linear spectroscopy.

Treating Eq. (II.32), one needs to consider the effect from vibrational degrees of freedom on the spectrum. To this end Eq. (II.17) is supplemented by vibrational states

$$|g, \mathbf{M}\rangle = \prod_m |g_m, M_{g_m}\rangle, \quad |m, \mathbf{M}\rangle = |e_m, M_{e_m}\rangle \prod_{n \neq m} |g_n, M_{g_n}\rangle \tag{II.33}$$

where  $M_{a_m}$  is the vibrational quantum number for site  $m$ . It refers to a *vibronic* excitation if site  $m$  is in state  $|e_m\rangle$  or to a *vibrational* excitation if site  $m$  is in state  $|g_m\rangle$ . The vibronic and vibrational quantum numbers are comprised into the index  $\mathbf{M} \equiv \{\dots, M_{e_m}, \dots, M_{g_n}, \dots\}$ . Eq. (II.32) is expanded as

$$\begin{aligned}
 H_{\text{agg}} &= \sum_{\mathbf{M}} E_{g,\mathbf{M}} |g, \mathbf{M}\rangle \langle g, \mathbf{M}| + \sum_m \sum_{\mathbf{M}} E_{m,\mathbf{M}} |m, \mathbf{M}\rangle \langle m, \mathbf{M}| \\
 &+ \sum_{m \neq n} \sum_{\mathbf{M}, \mathbf{N}} J_{mn} (\text{FC})_{\mathbf{M}\mathbf{N}} |m, \mathbf{M}\rangle \langle n, \mathbf{N}| + H_{\text{field}}(t)
 \end{aligned} \tag{II.34}$$

Here,  $E_{m,\mathbf{M}}$  is the energy of the exciton-vibrational state  $|m, \mathbf{M}\rangle$  and the product of FC overlap integral between sites  $m$  and  $n$  is (assuming the Condon-approximation to be valid)

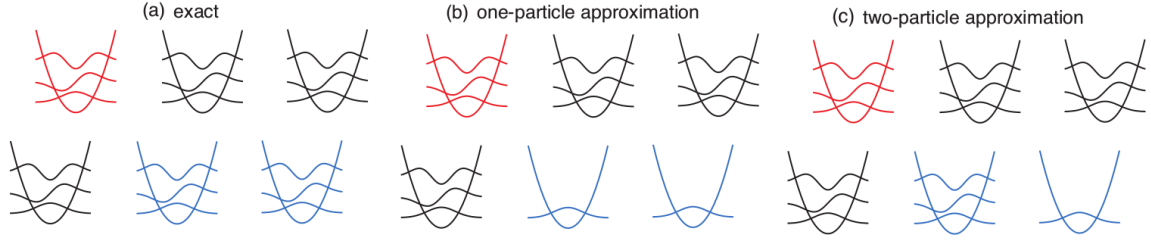
$$(\text{FC})_{\mathbf{M}\mathbf{N}} = \langle M_{e_m} | N_{g_m} \rangle \langle M_{g_n} | N_{e_n} \rangle \prod_{i \neq m, n} \delta_{M_{g_i} N_{g_i}} \tag{II.35}$$

Then the one-exciton eigenstates in this basis are

$$|\alpha\rangle = \sum_{m, \mathbf{M}} C_{m, \mathbf{M}} |m, \mathbf{M}\rangle \tag{II.36}$$

To treat high-dimensional situations, the  $n$ -particle approximation was proposed [65], which is shown in Fig. II.1. In the one-particle approximation (OPA) only vibronic excitations are allowed, i.e  $M_{g_n} = 0$  and  $M_{e_m} = 0, \dots, M_{e_m}^{\text{max}}$ . In the two-particle approximation (TPA) there are vibronic excitations for one site and a second site only is vibrationally excited, while others are




 Figure II.1: Schematic of the  $n$ -particle approximation

in their vibrational ground state, i.e  $M_{e_m} = 0, \dots, M_{e_m}^{\max}$ ,  $M_{g_n} = 0, \dots, M_{g_n}^{\max}$ , and  $M_{g_{k \neq m, n}} = 0$ . And in the  $n$ -particle approximation besides the vibronic excitations,  $n - 1$  vibrationally sites are excited and the others are still in their ground state.

## 2.2 SYSTEM-BATH APPROACH AND REDFIELD EQUATIONS OF MOTION

In the previous section, it has been assumed that all vibrational DOFs are treated equally and at the same QM level as the electronic DOFs. However, photosynthetic antenna systems or molecular aggregates are usually very complex, consisting of several chromophores embedded in a protein environment or a solution. It is practically impossible to consider all DOFs for the system in an explicit QM treatment. Therefore the total system is reduced to only a few DOFs, which are of interest because they provide insights into the physical processes. All other DOFs are treated as a heat bath, which interacts with the system DOFs. The Hamiltonian of the total system is separated as

$$H = H_S + H_B + H_{S-B} \quad (\text{II.37})$$

with  $H_S$  and  $H_B$  denoting the system and bath Hamiltonian, respectively.  $H_{S-B}$  represents the interaction between the system and bath. This separation implies that one will solve the QM equations of motion for the relevant system DOFs, treating the influence of the bath DOFs approximately. In this case, the density operator of the system is called a reduced density operator (RDO),  $\rho(t) = \text{tr}_B\{W(t)\}$ .

The equation of motion for the RDO according to the Liouville-Von Neumann equation is

$$\begin{aligned} \frac{\partial}{\partial t} \rho(t) &= \text{tr}_B \left\{ \frac{\partial}{\partial t} W(t) \right\} = -i \text{tr}_B \{ [H_S + H_B + H_{S-B}, W(t)] \} \\ &= -i [H_S, \rho(t)] - i \text{tr}_B \{ [H_{S-B} + H_B, W(t)] \} \end{aligned} \quad (\text{II.38})$$

Note here to get the final equation, it is assumed that the basis which defines the trace in the bath space is time independent. Then the system Hamiltonian  $H_S$  is not affected by the bath trace. Based on the cyclic invariance of the trace for  $H_B$ , which acts exclusively in the state space of the bath, one has  $\text{tr}_B \{ H_B W(t) \} = \text{tr}_B \{ W(t) H_B \}$ . Eq. (II.38) can be reduced to

$$\frac{\partial}{\partial t} \rho(t) = -i [H_S, \rho(t)] - i \text{tr}_B \{ [H_{S-B}, W(t)] \} \quad (\text{II.39})$$

and  $W(t)$  is assumed to factorize into  $\rho(t)$  and an operator  $R(t)$  which is defined only in the

Hilbert space of the bath and that obeys  $\text{tr}_B\{R\} = 1$ . Assuming that the system-bath interaction Hamiltonian can be factorized into system parts  $K_\mu$  and bath parts  $\Phi_\mu$ ,  $H_{S-B}$  becomes

$$H_{S-B} = \sum_{\mu} K_{\mu}(s)\Phi_{\mu}(Z) \quad (\text{II.40})$$

Here,  $s$  and  $Z$  comprise the coordinates of the system and bath respectively. The index  $\mu$  counts the different contributions that may follow from a particular microscopic model for the coupling between the system and bath. Then the approximate equation for the RDO becomes

$$\frac{\partial}{\partial t}\rho(t) = -i \left[ H_S + \sum_{\mu} K_{\mu}\text{tr}_B \{ \Phi_{\mu}R(t) \}, \rho(t) \right] \quad (\text{II.41})$$

Considering the general time evolution operator  $U(t-t_0) = \exp(-iH(t-t_0))$ , the “free” time-evolution operator is defined according to

$$U_0(t-t_0) = \exp(-iH_S(t-t_0))\exp(-iH_B(t-t_0)) \equiv U_S(t-t_0)U_B(t-t_0) \quad (\text{II.42})$$

Then in the interaction representation, we have

$$H_{S-B}^{(I)} = U_0^+(t-t_0)H_{S-B}U_0(t-t_0) \quad (\text{II.43})$$

$$\rho^{(I)}(t) = U_S^+(t-t_0)\rho(t)U_S(t-t_0) \quad (\text{II.44})$$

Taking an equilibrium assumption for  $R(t)$  i.e.  $R(t) \equiv R_{eq}$  with

$$R_{eq} = \frac{\exp(-H_B/k_B T)}{\text{tr}_B\{\exp(-H_B/k_B T)\}} \quad (\text{II.45})$$

the equation of motion for the RDO up to second order with respect to  $H_{S-B}$  reads

$$\begin{aligned} \frac{\partial}{\partial t}\rho^{(I)}(t) = & -i \text{tr}_B \left\{ R_{eq} \left[ H_{S-B}^{(I)}(t), \rho^{(I)}(t) \right] \right\} - \int_{t_0}^t d\tau' \text{tr}_B \left\{ \left[ H_{S-B}^{(I)}(t), \left[ H_{S-B}^{(I)}(\tau'), R_{eq}\rho^{(I)}(\tau') \right] \right] \right\} \\ & + \int_{t_0}^t d\tau' \text{tr}_B \left\{ \left[ H_{S-B}^{(I)}(t), R_{eq}\text{tr}_B \left\{ \left[ H_{S-B}^{(I)}(\tau'), R_{eq}\rho^{(I)}(\tau') \right] \right\} \right] \right\} \end{aligned} \quad (\text{II.46})$$

Defining the correlation function as (Here and in the following  $\text{tr}_B\{R_{eq}\dots\} = \langle \dots \rangle_B$ )

$$C_{\mu\nu}(t) = \langle \Phi_{\mu}(t)\Phi_{\nu}(0) \rangle_B - \langle \Phi_{\mu}(t) \rangle_B \langle \Phi_{\nu}(0) \rangle_B = \langle \Delta\Phi_{\mu}(t)\Delta\Phi_{\nu}(0) \rangle_B \quad (\text{II.47})$$

the equation of motion for RDO follows as

$$\begin{aligned} \frac{\partial}{\partial t}\rho^{(I)}(t) = & -i \sum_{\mu} \langle \Phi_{\mu} \rangle_B \left[ K_{\mu}^{(I)}, \rho^{(I)}(t) \right] - \sum_{\mu,\nu} \int_{t_0}^t d\tau' \left( C_{\mu\nu}(t-\tau') \left[ K_{\mu}^{(I)}(t), K_{\nu}^{(I)}(\tau')\rho^{(I)}(\tau') \right] \right. \\ & \left. - C_{\nu\mu}(-t+\tau') \left[ K_{\mu}^{(I)}(t), \rho^{(I)}(\tau')K_{\nu}^{(I)}(\tau') \right] \right) \end{aligned} \quad (\text{II.48})$$

Following Eq. (II.44) the equation of motion for the RDO can be transformed from the interaction representation into the Schrödinger representation as

$$\begin{aligned}
 \frac{\partial}{\partial t}\rho(t) &= \frac{\partial}{\partial t} \left[ U_S(t-t_0)\rho^{(I)}(t)U_S^+(t-t_0) \right] \\
 &= -i[H_S, \rho(t)] + U_S(t-t_0)\frac{\partial}{\partial t}\rho^{(I)}(t)U_S^+(t-t_0) \\
 &= -i \left[ H_S + \sum_{\mu} \langle \Phi_{\mu} \rangle_B K_{\mu}, \rho(t) \right] - U_S(t-t_0) \sum_{\mu, \nu} \int_{t_0}^t d\tau' \{ C_{\mu\nu}(t-\tau') \\
 &\quad \times [U_S^+(t-t_0)K_{\mu}U_S(t-t_0), U_S^+(\tau'-t_0)K_{\nu}U_S(\tau'-t_0)U_S^+(\tau'-t_0)\rho(\tau')U_S(\tau'-t_0)] \\
 &\quad - C_{\nu\mu}(-t+\tau') [U_S^+(t-t_0)K_{\mu}U_S(t-t_0), U_S^+(\tau'-t_0)\rho(\tau')U_S(\tau'-t_0) \\
 &\quad \times U_S^+(\tau'-t_0)K_{\nu}U_S(\tau'-t_0)] \} U_S^+(t-t_0)
 \end{aligned} \tag{II.49}$$

Combining products of time-evolution and replace  $t-\tau'$  by  $\tau$ , one obtains the QME in Schrödinger representation

$$\begin{aligned}
 \frac{\partial}{\partial t}\rho(t) &= -i \left[ H_S + \sum_{\mu} \langle \Phi_{\mu} \rangle_B K_{\mu}, \rho(t) \right] - \sum_{\mu, \nu} \int_0^{t-t_0} d\tau \{ C_{\mu\nu}(\tau) [K_{\mu}, \\
 &\quad U_S(\tau)K_{\nu}\rho(t-\tau)U_S^+(\tau)] - C_{\nu\mu}(-\tau) [K_{\mu}, U_S(\tau)\rho(t-\tau)K_{\nu}U_S^+(\tau)] \}
 \end{aligned} \tag{II.50}$$

The term  $\sim \langle \Phi_{\mu} \rangle_B$  contains the mean-field contribution to the system dynamics, which is of first order in the system-bath interaction. The second term, which depends on the correlation function  $C_{\mu\nu}$ , is responsible for energy dissipation from the relevant system into the bath and decoherence of the system's dynamics.

Considering the interaction representation the Markov approximation can be involved according to

$$\begin{aligned}
 \rho(t-\tau) &= U_S(t-\tau-t_0)\rho^{(I)}(t-\tau)U_S^+(t-\tau-t_0) \\
 &\approx U_S(-\tau)U_S(t-t_0)\rho^{(I)}(t)U_S^+(t-t_0)U_S^+(-\tau) \\
 &= U_S^+(\tau)\rho(t)U_S(\tau)
 \end{aligned} \tag{II.51}$$

The dissipation part of the QME becomes

$$\left( \frac{\partial \rho(t)}{\partial t} \right)_{\text{diss}} = - \sum_{\mu, \nu} \int_0^{\infty} d\tau \left\{ C_{\mu\nu}(\tau) [K_{\mu}, K_{\nu}^{(I)}(-\tau)\rho(t)] - C_{\nu\mu}(-\tau) [K_{\mu}, \rho(t)K_{\nu}^{(I)}(-\tau)] \right\} \tag{II.52}$$

where  $K_{\nu}^{(I)}(-\tau) = U_S(\tau)K_{\nu}U_S^+(\tau)$ . A more compact form is obtained after introduction of the operator

$$\Lambda_{\mu} = \sum_{\nu} \int_0^{\infty} d\tau C_{\mu\nu}(\tau)K_{\nu}^{(I)}(-\tau) \tag{II.53}$$

$$H_S^{(\text{eff})} = H_S + \sum_{\mu} K_{\mu} [\langle \Phi_{\mu} \rangle_B - i\Lambda_{\mu}] \tag{II.54}$$

With this definition the final result in the Markov approximation for Eq. (II.50) is

$$\frac{\partial}{\partial t}\rho(t) = i \left( H_S^{(\text{eff})} \rho(t) - \rho(t) H_S^{(\text{eff})+} \right) + \sum_{\mu} \left( K_{\mu} \rho(t) \Lambda_{\mu}^{(+)} + \Lambda_{\mu} \rho(t) K_{\mu} \right) \quad (\text{II.55})$$

Here the operator  $\Lambda_{\mu}^{(+)}$  following from  $\Lambda_{\mu}$  by replacing  $C_{\mu\nu}(\tau)$  with  $C_{\nu\mu}(-\tau)$  (if any term of  $H_{S-B}$  is Hermitian, then  $\Lambda_{\mu}^{(+)} = \Lambda_{\mu}^{+}$ ). And  $H_S^{(\text{eff})+}$  needs to be understood as the Hermitian conjugation of  $H_S^{(\text{eff})}$  except all  $\Lambda_{\mu}$  are replaced by  $\Lambda_{\mu}^{(+)}$ .

## CORRELATION FUNCTION

For the reservoir of many systems, the atoms or molecules have high symmetry and the vibrations only appear as small oscillations around the equilibrium positions. Thus the reservoir usually is described by a harmonic approximation. Then if one performs a Taylor expansion of  $H_{S-B}$  with respect to the reservoir coordinates and focus on the lowest-order contribution only,  $H_{S-B}$  in Eq. (II.40) will become linear with respect to the harmonic oscillator coordinates  $Z = \{Z_{\xi}\}$ :

$$H_{S-B} = K(s)\Phi(Z) = K(s) \sum_{\xi} \hbar \gamma_{\xi} Z_{\xi} \quad (\text{II.56})$$

here  $\gamma_{\xi}$  is the system-reservoir coupling constant. Since dealing with decoupled normal-mode oscillators, one can define the reservoir part  $\Phi(Z)$  by using normal-mode frequency  $\omega_{\xi}$  and its harmonic oscillator eigenstates  $|N_{\xi}\rangle = (C_{\xi}^{+})^{N_{\xi}}|0_{\xi}\rangle/\sqrt{N_{\xi}!}$  as

$$\Phi(Z) = \sum_{\xi} \hbar \omega_{\xi} g_{\xi} (C_{\xi} + C_{\xi}^{+}) \quad (\text{II.57})$$

with  $g_{\xi} = \gamma_{\xi} \sqrt{\hbar/2\omega_{\xi}^3}$ . If simply writing  $Q_{\xi} = C_{\xi} + C_{\xi}^{+}$ , Eq. (II.47) will become

$$\begin{aligned} C(t) &= \sum_{\xi, \xi'} \omega_{\xi} g_{\xi} \omega_{\xi'} g_{\xi'} \text{tr}_B \{ R_{\text{eq}} Q_{\xi}(t) Q_{\xi'} \} \\ &= \sum_{\xi, \xi'} \omega_{\xi} g_{\xi} \omega_{\xi'} g_{\xi'} \sum_{\{N_{\zeta}\}} \left( \prod_{\zeta} f_{N_{\zeta}} \langle N_{\zeta} | \right) Q_{\xi}(t) Q_{\xi'} \left( \prod_{\zeta'} |N_{\zeta'}\rangle \right) \\ &= \sum_{\xi, \xi'} \omega_{\xi} g_{\xi} \omega_{\xi'} g_{\xi'} \sum_{N_{\xi}, N_{\xi'}} f_{N_{\xi}} \langle N_{\xi} | \langle N_{\xi'} | Q_{\xi}(t) Q_{\xi'} | N_{\xi} \rangle | N_{\xi'} \rangle \\ &= \sum_{\xi} \omega_{\xi}^2 g_{\xi}^2 \sum_{N_{\xi}} f_{N_{\xi}} \langle N_{\xi} | \left[ C_{\xi} e^{-i\omega_{\xi} t} + C_{\xi}^{+} e^{i\omega_{\xi} t} \right] \left[ C_{\xi} + C_{\xi}^{+} \right] | N_{\xi} \rangle \\ &= \sum_{\xi} \omega_{\xi}^2 g_{\xi}^2 \sum_{N_{\xi}} f_{N_{\xi}} \left( [1 + N_{\xi}] e^{-i\omega_{\xi} t} + e^{i\omega_{\xi} t} N_{\xi} \right) \end{aligned} \quad (\text{II.58})$$

with the thermal distributions  $f_{N_{\xi}} = 1/Z \times \exp(-N_{\xi} \hbar \omega_{\xi} / k_B T)$ . Introducing the Bose-Einstein distribution, which is the mean occupation number of a harmonic oscillator mode

$$n(\omega_{\xi}) = \sum_{N_{\xi}} N_{\xi} f_{N_{\xi}} = \frac{1}{\exp\{\hbar \omega_{\xi} / k_B T\} - 1} \quad (\text{II.59})$$

one obtains

$$C(t) = \sum_{\xi} (\omega_{\xi} g_{\xi})^2 \{ [1 + n(\omega_{\xi})] e^{-i\omega_{\xi} t} + n(\omega_{\xi}) e^{i\omega_{\xi} t} \} \quad (\text{II.60})$$

The Fourier-transformed form is

$$C(\omega) = \sum_{\xi} 2\pi (\omega_{\xi} g_{\xi})^2 \{ [1 + n(\omega_{\xi})] \delta(\omega - \omega_{\xi}) + n(\omega_{\xi}) \delta(\omega + \omega_{\xi}) \} \quad (\text{II.61})$$

If one defines spectral density  $J(\omega)$  as

$$J(\omega) = \sum_{\xi} g_{\xi}^2 \delta(\omega - \omega_{\xi}) \quad (\text{II.62})$$

The Fourier-transformed correlation function reads

$$C(\omega) = 2\pi \omega^2 [1 + n(\omega)] [J(\omega) - J(-\omega)] \quad (\text{II.63})$$

## RELAXATION AND DEPHASING RATES

Transforming the QME (II.50) into the energy representation assuming  $H_S|a\rangle = E_a|a\rangle$ . The reduced density matrix (RDM) will be given by  $\rho_{ab}(t) = \langle a|\rho(t)|b\rangle$ . Introducing the elements of the system part of the system-bath coupling according to  $\langle a|K_{\mu}|b\rangle = K_{ab}^{(\mu)}$ , one obtains the dissipative part of QME for Eq. (II.52) as

$$\begin{aligned} \left( \frac{\partial \rho_{ab}}{\partial t} \right)_{\text{diss.}} = & - \sum_{c,d} \sum_{\mu\nu} \int_0^{\infty} d\tau \left\{ C_{\mu\nu}(\tau) \left[ K_{ac}^{(\mu)} K_{cd}^{(\nu)} e^{i\omega_{dc}\tau} \rho_{db}(t) - K_{db}^{(\mu)} K_{ac}^{(\nu)} e^{i\omega_{ca}\tau} \rho_{cd}(t) \right] \right. \\ & \left. - C_{\nu\mu}(-\tau) \left[ K_{ac}^{(\mu)} K_{db}^{(\nu)} e^{i\omega_{bd}\tau} \rho_{cd}(t) - K_{db}^{(\mu)} K_{cd}^{(\nu)} e^{i\omega_{dc}\tau} \rho_{ac}(t) \right] \right\} \end{aligned} \quad (\text{II.64})$$

with  $\omega_{ab} = (E_a - E_b)/\hbar$ . Defining the tetradic matrix

$$M_{ab,cd}(t) = \sum_{\mu\nu} C_{\mu\nu}(t) K_{ab}^{(\mu)} K_{cd}^{(\nu)} \quad (\text{II.65})$$

Eq. (II.64) becomes

$$\begin{aligned} \left( \frac{\partial \rho_{ab}}{\partial t} \right)_{\text{diss.}} = & - \sum_{c,d} \int_0^{\infty} d\tau \left\{ M_{cd,db}(-\tau) e^{i\omega_{dc}\tau} \rho_{ac}(t) + M_{ac,cd}(\tau) e^{i\omega_{dc}\tau} \rho_{db}(t) \right. \\ & \left. - [M_{db,ac}(-\tau) e^{i\omega_{bd}\tau} + M_{db,ac}(\tau) e^{i\omega_{ca}\tau}] \rho_{cd}(t) \right\} \end{aligned} \quad (\text{II.66})$$

In this equation, the real part introduces an irreversible redistribution of the amplitudes contained in the RDM. And the imaginary part represents the term, which can be interpreted as a modification of the transition frequencies and the respective mean-field matrix elements. It will be neglected in the following. Next one introduces the damping matrix as the real part of the Fourier-transformed tetradic matrix:

$$\Gamma_{ab,cd}(\omega) = \text{Re} \int_0^{\infty} d\tau e^{i\omega\tau} M_{ab,cd}(\tau) = \text{Re} \sum_{\mu\nu} K_{ab}^{(\mu)} K_{cd}^{(\nu)} \int_0^{\infty} d\tau e^{i\omega\tau} C_{\mu\nu}(\tau) \quad (\text{II.67})$$

Considering the definition of  $\Lambda_\mu$  in Eq. (II.53), the damping matrix can also be written as

$$\Gamma_{ab,cd}(\omega_{dc}) = \text{Re} \sum_{\mu} \langle a | K_{\mu} | b \rangle \langle c | \Lambda_{\mu} | d \rangle \quad (\text{II.68})$$

Using this notation, Eq. (II.66) becomes

$$\begin{aligned} \left( \frac{\partial \rho_{ab}}{\partial t} \right)_{\text{diss.}} = & - \sum_{c,d} \{ \Gamma_{bd,dc}(\omega_{cd}) \rho_{ac}(t) + \Gamma_{ac,cd}(\omega_{dc}) \rho_{db}(t) \\ & - [ \Gamma_{ca,bd}(\omega_{db}) + \Gamma_{db,ac}(\omega_{ca}) ] \rho_{cd}(t) \} \end{aligned} \quad (\text{II.69})$$

If one further defines the relaxation matrix as

$$R_{ab,cd} = \delta_{a,c} \sum_e \Gamma_{be,ed}(\omega_{de}) + \delta_{b,d} \sum_e \Gamma_{ae,ec}(\omega_{ce}) - \Gamma_{ca,bd}(\omega_{db}) - \Gamma_{db,ac}(\omega_{ca}) \quad (\text{II.70})$$

The dissipative term of the RDM can be simplified as

$$\left( \frac{\partial \rho_{ab}}{\partial t} \right)_{\text{diss.}} = - \sum_{cd} R_{ab,cd} \rho_{cd}(t) \quad (\text{II.71})$$

The transition rate  $k_{a \rightarrow b}$  from state  $|a\rangle$  to state  $|b\rangle$  is

$$k_{a \rightarrow b} = 2\Gamma_{ab,ba}(\omega_{ab}) = 2\text{Re} \int_0^{\infty} d\tau e^{i\omega_{ab}\tau} M_{ab,ba}(\tau) = \sum_{\mu\nu} C_{\mu\nu}(\omega_{ab}) K_{ab}^{(\mu)} K_{ba}^{(\nu)} \quad (\text{II.72})$$

This rate is also called energy relaxation rates. From the equation, one finds the amplitude for relaxation is determined by the matrix elements of the operators  $K_{\mu}$  and the value of the correlation function at the respective transition frequency  $C_{\mu\nu}(\omega = \omega_{ab})$ .

According to Eq. (II.69), the coherence dephasing rate  $\gamma_{ab}$  is

$$\gamma_{ab} = \sum_e [ \Gamma_{ae,ea}(\omega_{ae}) + \Gamma_{be,eb}(\omega_{be}) ] - \Gamma_{aa,bb}(0) - \Gamma_{bb,aa}(0) \quad (\text{II.73})$$

This expression determines the damping of the off-diagonal elements of the RDM. One notices the first part of this equation represents the transitions out of states  $|a\rangle$  and  $|b\rangle$  according to Eq. (II.72). The remaining part, usually denoted by  $\gamma_{ab}^{(\text{pd})}$ , describes an elastic type of collision where no energy is exchanged between system and bath.

### 3 THE POLARIZATION-FIELD OF A SPHERICAL NANOPARTICLE

The model system of an uncharged dielectric sphere and a single external point charge is shown in the Fig. II.2. Considering the size, the polarization of the NS is treated in classical approximation [66].

The total electrostatic potential  $V_{\text{tot}}^1(\vec{r})$  for this system is obtained by the Poisson equation as

$$\nabla^2 V_{\text{tot}}^1(\vec{r}) = - \frac{\rho(\vec{r})}{\epsilon} \quad (\text{II.74})$$

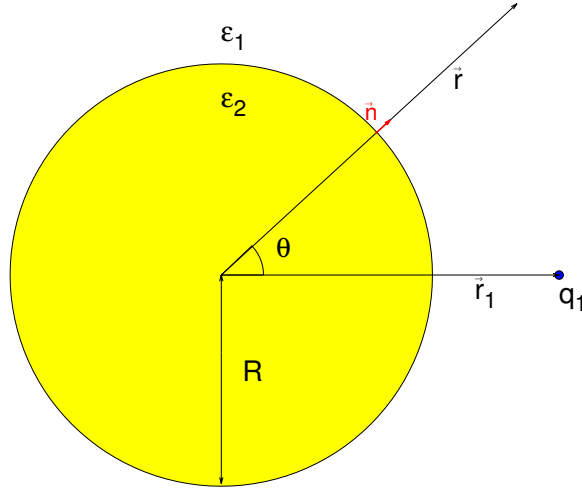


Figure II.2: An uncharged dielectric sphere of relative permittivity  $\varepsilon_2$  was embedded in an infinite  $\varepsilon_1$  medium. A point charge  $q_1$  is located outside the sphere.

where  $\rho(\vec{r})$  is charge density and  $\varepsilon = \varepsilon_0 \varepsilon_i$  with  $\varepsilon_0$  being the vacuum permittivity and  $i = 1, 2$ . Considering  $\rho(\vec{r}) = q_1 \delta(\vec{r} - \vec{r}_1)$  and the azimuthal symmetry for this model, Eq. (II.74) becomes the Laplace equation when  $\vec{r} \neq \vec{r}_1$ :

$$\nabla^2 V_{\text{tot}}^1(r, \theta) = \frac{1}{r^2} \frac{\partial}{\partial r} \left( r^2 \frac{\partial V_{\text{tot}}^1}{\partial r} \right) + \frac{1}{r^2 \sin \theta} \frac{\partial}{\partial \theta} \left( \sin \theta \frac{\partial V_{\text{tot}}^1}{\partial \theta} \right) = 0 \quad (\text{II.75})$$

with  $r = |\vec{r}|$  and  $\theta$  being the angle between  $\vec{r}$  and  $\vec{r}_1$  as shown in Fig. II.2. As is known, the general solution for the Laplace equation is given by [67]

$$V_{\text{tot}}^1(\vec{r}) = \sum_{l=0}^{\infty} \left[ M_l r^l + N_l \frac{1}{r^{l+1}} \right] P_l(\cos \theta) \quad (\text{II.76})$$

with  $P_l(\cos \theta)$  being the Legendre polynomial and coefficient  $M_l, N_l$  in the order  $l$ .

The electrostatic potential  $V_{\text{tot}}^1(\vec{r})$  must be finite at  $r = 0$ , thus inside the sphere  $r \leq R$  it reads

$$V_{\text{tot}}^1(r, \theta) = \sum_{l=0}^{\infty} M_l r^l P_l(\cos \theta) \quad (\text{II.77})$$

In addition, the potential of the point charge  $q_1$  reads

$$V_{\text{point}}^1(r, \theta) = \frac{q_1}{\varepsilon_1 |\vec{r} - \vec{r}_1|} = \begin{cases} \sum_{l=0}^{\infty} \frac{q_1 r^l}{\varepsilon_1 r_1^{l+1}} P_l(\cos \theta) & r < r_1 \\ \sum_{l=0}^{\infty} \frac{q_1 r_1^l}{\varepsilon_1 r^{l+1}} P_l(\cos \theta) & r > r_1 \end{cases} \quad (\text{II.78})$$

Due to the fact that  $V_{\text{tot}}^1(\vec{r})$  must be finite at  $r \rightarrow \infty$ , the electrostatic potential outside the

sphere  $r > R$  is

$$V_{\text{tot}}^1(r, \theta) = \begin{cases} \sum_{l=0}^{\infty} \left[ \frac{N_l}{r^{l+1}} + \frac{q_1 r^l}{\varepsilon_1 r_1^{l+1}} \right] P_l(\cos \theta) & r < r_1 \\ \sum_{l=0}^{\infty} \left[ \frac{N_l}{r^{l+1}} + \frac{q_1 r_1^l}{\varepsilon_1 r^{l+1}} \right] P_l(\cos \theta) & r > r_1 \end{cases} \quad (\text{II.79})$$

According to Maxwell's equations, the boundary conditions on the spherical interface at  $r = R$  satisfy

$$\begin{cases} \left( \vec{D}_{\text{tot}}^1|_{r=R^+} - \vec{D}_{\text{tot}}^1|_{r=R^-} \right) \cdot \vec{n} = 0 \\ \left( \vec{E}_{\text{tot}}^1|_{r=R^+} - \vec{E}_{\text{tot}}^1|_{r=R^-} \right) \times \vec{n} = 0 \end{cases} \quad (\text{II.80})$$

where  $\vec{n} = \vec{r}/r$  is a unit normal vector on the surface as in Fig. II.2. In Eq. (II.80) it is  $\vec{E}_{\text{tot}}^1 = -\nabla V_{\text{tot}}^1$  and  $\vec{D}_{\text{tot}}^1 = \varepsilon \vec{E}_{\text{tot}}^1$ . Thus combining Eqs. (II.77) and (II.79) into Eq. (II.80), it follows

$$\begin{cases} \varepsilon_1 \left[ \frac{N_l(l+1)}{R^{l+2}} + \frac{q_1 l R^{l-1}}{\varepsilon_1 r_1^{l+1}} \right] = -\varepsilon_2 M_l l R^{l+1} \\ \frac{N_l}{R^{l+1}} + \frac{q_1 R^l}{\varepsilon_1 r_1^{l+1}} = M_l R^l \end{cases} \quad (\text{II.81})$$

Solving the Eq. (II.81) for the coefficients  $M_l$  and  $N_l$  yield

$$\begin{cases} M_l = \frac{q_1(2l+1)}{r_1^{l+1}[\varepsilon_1(l+1) + \varepsilon_2 l]} \\ N_l = \frac{q_1 R^{2l+1}(\varepsilon_1 - \varepsilon_2)l}{\varepsilon_1 r_1^{l+1}[\varepsilon_1(l+1) + \varepsilon_2 l]} \end{cases} \quad (\text{II.82})$$

Finally, the polarization potential  $V_{\text{pol}}^1(r)$  outside of the dielectric sphere ( $r \geq R$ ) due to the point charge  $q_1$  is obtained by Eq. (II.78) and (II.79) with (II.82)

$$V_{\text{pol}}^1(r, \theta) = V_{\text{tot}}^1(r, \theta) - V_{\text{point}}^1(r, \theta) = \sum_{l=1}^{\infty} \frac{q_1(\varepsilon_1 - \varepsilon_2)l}{\varepsilon_1[(\varepsilon_1 + \varepsilon_2)l + \varepsilon_1]} \frac{R^{2l+1}}{r^{l+1}r_1^{l+1}} P_l(\cos \theta) \quad (\text{II.83})$$

Thus the total polarization potential of the NS due to the molecule can be expressed in multipolar form

$$V_{\text{pol}}(\vec{r}) = \sum_{A=1}^N \sum_{l=1}^m \frac{q_A(1 - \varepsilon_r)l}{(1 + \varepsilon_r)l + 1} \frac{R^{2l+1}}{r^{l+1}R_A^{l+1}} P_l(\cos \theta) \quad (\text{II.84})$$

where  $R$  is the radius,  $\varepsilon_r$  is the relative permittivity of the NS and the upper summation limit  $m$  is the chosen highest order to reach convergence.  $N$  is the number of atoms in the molecule with Mulliken charge  $q_A$  at distance  $R_A$  from the center of the NS ( $A = 1, \dots, N$ ).

When the uncharged dielectric sphere is in the external field  $\vec{E}_{\text{ext}}(t)$  as Fig. II.3, the total potential  $V_{\text{tot}}^f(\vec{r})$  can be also expanded with the associated Legendre polynomials in Eq. (II.76) due to the azimuthal symmetry. For this model, it must satisfy that  $V_{\text{tot}}^f(\vec{r})$  is finite when  $r \rightarrow 0$ , i.e.  $N_l = 0$  for  $r \leq R$ . And  $V_{\text{tot}}^f(\vec{r})$  has to be replaced by  $-E_{\text{ext}}(t)r \cos \theta$  when  $r \rightarrow \infty$ . Thus the



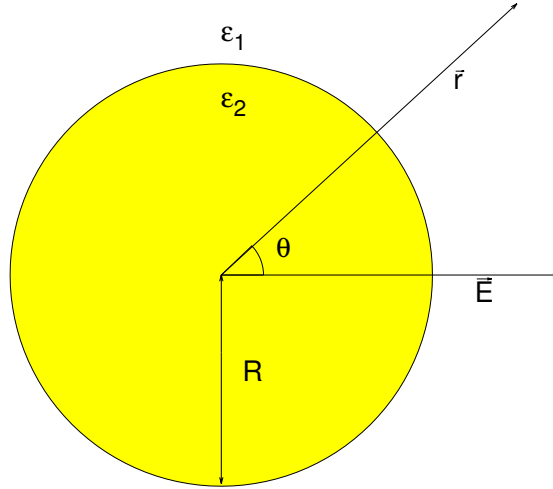


Figure II.3: An uncharged dielectric sphere of relative permittivity  $\varepsilon_2$  embedded in an infinite  $\varepsilon_1$  medium with external field  $\vec{E}_{\text{ext}}(t)$ .

potential of the NS reads

$$V_{\text{tot}}^f(r, \theta, t) = \begin{cases} \sum_{l=0}^{\infty} M_l r^l P_l(\cos \theta) & r \leq R \\ \sum_{l=0}^{\infty} \frac{N_l}{r^{l+1}} P_l(\cos \theta) - E_{\text{ext}}(t) r \cos \theta & r > R \end{cases} \quad (\text{II.85})$$

The continuous boundary conditions for this model are

$$\begin{cases} V_{\text{tot}}^f|_{R^-} = V_{\text{tot}}^f|_{R^+} \\ \varepsilon_2 \frac{\partial V_{\text{tot}}^f}{\partial r} \Big|_{R^-} = \varepsilon_1 \frac{\partial V_{\text{tot}}^f}{\partial r} \Big|_{R^+} \end{cases} \quad (\text{II.86})$$

Consider  $-E_{\text{ext}}(t)r \cos \theta = -E_{\text{ext}}(t)r P_1(\cos \theta)$ , thus when  $l \neq 1$  the coefficients satisfy

$$\begin{cases} M_l R^l = \frac{N_l}{R^{l+1}} \\ \varepsilon_2 l M_l R^{l-1} = -\varepsilon_1 \frac{N_l(l+1)}{R^{l+2}} \end{cases} \quad (\text{II.87})$$

And for  $l = 1$ , they follow as

$$\begin{cases} M_1 R = \frac{N_1}{R^2} - E_{\text{ext}} R \\ \varepsilon_2 M_1 = -\varepsilon_1 \frac{2N_1}{R^3} - \varepsilon_1 E_{\text{ext}} \end{cases} \quad (\text{II.88})$$

Solving the Eqs. (II.87) and (II.88), one finds

$$\begin{cases} M_1 = -\frac{3\varepsilon_1 E_{\text{ext}}}{\varepsilon_2 + 2\varepsilon_1} \\ N_1 = \frac{(\varepsilon_2 - \varepsilon_1) E_{\text{ext}} R^3}{\varepsilon_2 + 2\varepsilon_1} \\ M_l = N_l = 0 \quad l \neq 1 \end{cases} \quad (\text{II.89})$$

Finally, the total potential of NS with relative permittivity  $\varepsilon_r$  due to external field  $E_{\text{ext}}$  is

$$V_{\text{tot}}^{\text{f}}(\vec{r}, t) = \begin{cases} -\frac{3E_{\text{ext}}(t)}{\varepsilon_r + 2} r \cos \theta & r \leq R \\ -E_{\text{ext}}(t) \left[ 1 - \frac{(\varepsilon_r - 1)R^3}{(\varepsilon_r + 2)r^3} \right] r \cos \theta & r > R \end{cases} \quad (\text{II.90})$$

with  $\theta$  being the angle between  $\vec{r}$  and the external field  $\vec{E}_{\text{ext}}(t)$  as in Fig. II.3. Considered the relation between the potential and field  $E_{\text{tot}}^{\text{f}} = -\nabla V_{\text{tot}}^{\text{f}}$ , the total field induced by the external field is

$$E_{\text{tot}}^{\text{f}}(t)(\vec{r}, t) = \begin{cases} \frac{3E_{\text{ext}}(t)}{\varepsilon_r + 2} \cos \theta & r \leq R \\ E_{\text{ext}}(t) \left[ 1 + \frac{2(\varepsilon_r - 1)R^3}{(\varepsilon_r + 2)r^3} \right] \cos \theta & r > R \end{cases} \quad (\text{II.91})$$

## 4 DFTB-BASED CALCULATION OF ELECTRONIC STATES

The charge and energy transfer in molecules is described by the electronic Schrödinger equation. Often ab initio methods are exploited to solve this equation. Here attention is focused on the simpler SCC-DFTB method and an approximate Time-Dependent Density-Functional Theory (TDDFT) [68].

### 4.1 SCC-DFTB THEORY IN TIME-INDEPENDENT CONSTANT EXTERNAL FIELD

DFT is the most popular theoretical method to determine the electronic structure. It can reach high accuracy using generalized gradient approximation for the exchange-correlation (XC) functional. DFTB is an approximate method based on the DFT framework, but doesn't require many empirical parameters and has a better computational scaling. SCC-DFTB is an extension of DFTB to improve total energies, forces, and transferability by the Self-Consistent-Charge (SCC) approach. It is based on a second-order expansion of the Kohn-Sham (KS) total energy with respect to charge density fluctuations. From Eq. (II.7), a system of electrons obeys the Schrödinger equation

$$H_e \Psi(\vec{r}) = [T_e + V_{ee} + V_{\text{ext}}] \Psi(\vec{r}) = E \Psi(\vec{r}) \quad (\text{II.92})$$

where  $V_{\text{ext}}$  is the external potential for the system of electrons, which is a sum of the nuclear potential  $V_{en}$  and an electric field potential  $V_{\text{field}}(\vec{r})$ .

Based on the Hohenberg-Kohn theorem [69], there exists a one-to-one correspondence between the external potential and the one-body density. But to obtain the density of an interacting system is very hard. To solve this, Kohn and Sham introduced an auxiliary system of non-interaction particles [70], whose dynamics are governed by a potential chosen such that the

density of the KS system equals the density of the interacting system. This potential  $V_{\text{KS}}$  is local in real space, but highly non-locally dependent on the density  $\rho(\vec{r})$ . The KS molecular orbitals obey

$$\left[ -\frac{\nabla^2}{2} + V_{\text{KS}}(\vec{r}) \right] \Psi_i(\vec{r}) = E \Psi_i(\vec{r}) \quad (\text{II.93})$$

The density of the interacting system follows from the KS orbitals as

$$\rho(\vec{r}) = \sum_i^{\text{occ}} |\Psi_i(\vec{r})|^2 \quad (\text{II.94})$$

The KS potential in Eq. (II.93) is given by

$$V_{\text{KS}}(\vec{r}) = V_{\text{ext}}(\vec{r}) + V_{\text{Hartree}}(\vec{r}) + V_{\text{xc}}(\vec{r}) \quad (\text{II.95})$$

The first term is again the external potential. The second term is the classical electrostatic potential between the electrons

$$V_{\text{Hartree}}(\vec{r}) = \int' \frac{\rho(\vec{r}')}{|\vec{r} - \vec{r}'|} \quad (\text{II.96})$$

The last term, the XC potential  $V_{\text{xc}}(\vec{r})$ , comprises the non-trivial many-body effects and is a functional of the density and defined by the XC energy  $E_{\text{xc}}$  as

$$V_{\text{xc}}(\vec{r}) = \frac{\delta E_{\text{xc}}[\rho]}{\delta \rho(\vec{r})} \quad (\text{II.97})$$

The energy of a molecule comprised of  $N_e$  electron and  $N_n$  nuclei can be expressed with the KS states  $\Psi_i(\vec{r})$  as

$$E[\rho] = \sum_i^{\text{occ}} \langle \Psi_i(\vec{r}) | -\frac{\nabla^2}{2} + V_{\text{ext}}[\rho] + \frac{1}{2} \int' \frac{\rho(\vec{r}')}{|\vec{r} - \vec{r}'|} | \Psi_i(\vec{r}) \rangle + E_{\text{xc}}[\rho] + V_{nn} \quad (\text{II.98})$$

Following Foulkes and Haydock [71] the electronic density can be treated as the sum of a reference density and the deviation to the actual density:

$$\rho(\vec{r}) = \rho_0(\vec{r}) + \delta\rho(\vec{r}) \quad (\text{II.99})$$

The reference density  $\rho_0$  is the superposition of contributions from free neutral atoms. Inserting Eq. (II.99) into Eq. (II.98) (Here and in the following  $\rho = \rho(\vec{r})$  and  $\rho' = \rho(\vec{r}')$  as shorthand notations) yields

$$E = \sum_i^{\text{occ}} \langle \Psi_i(\vec{r}) | -\frac{\nabla^2}{2} + V_{\text{ext}}(\vec{r}) + \int' \frac{\rho'_0}{|\vec{r} - \vec{r}'|} + V_{\text{xc}}[\rho_0] | \Psi_i(\vec{r}) \rangle - \frac{1}{2} \iiint' \frac{\rho'_0(\rho_0 + \delta\rho)}{|\vec{r} - \vec{r}'|} \quad (\text{II.100a})$$

$$- \int V_{\text{xc}}[\rho_0](\rho_0 + \delta\rho) + \frac{1}{2} \iiint' \frac{\delta\rho'(\rho_0 + \delta\rho)}{|\vec{r} - \vec{r}'|} + E_{\text{xc}}[\rho_0 + \delta\rho] + V_{nn} \quad (\text{II.100b})$$

Next,  $E_{\text{xc}}[\rho_0 + \delta\rho]$  is expanded to the second order term in a Taylor series:

$$E_{\text{xc}}[\rho_0 + \delta\rho] = E_{\text{xc}}[\rho_0] + \int \frac{\delta E_{\text{xc}}}{\delta\rho} \Big|_{\rho_0} \delta\rho + \frac{1}{2} \iint' \frac{\delta^2 E_{\text{xc}}}{\delta\rho\delta\rho'} \Big|_{\rho_0} \delta\rho\delta\rho' \quad (\text{II.101})$$

Consider Eq. (II.97), the total energy in DFT is

$$E = \sum_i^{\text{occ}} \langle \Psi_i(\vec{r}) | -\frac{\nabla^2}{2} + V_{\text{ext}}(\vec{r}) + \int' \frac{\rho'_0}{|\vec{r} - \vec{r}'|} + V_{\text{xc}}[\rho_0] | \Psi_i(\vec{r}) \rangle \quad (\text{II.102a})$$

$$- \frac{1}{2} \iint' \frac{\rho'_0 \rho_0}{|\vec{r} - \vec{r}'|} + E_{\text{xc}}[\rho_0] - \int V_{\text{xc}}[\rho_0] \rho_0 + V_{nn} \quad (\text{II.102b})$$

$$+ \frac{1}{2} \iint' \left( \frac{1}{|\vec{r} - \vec{r}'|} + \frac{\delta^2 E_{\text{xc}}}{\delta\rho\delta\rho'} \Big|_{\rho_0} \right) \delta\rho\delta\rho' \quad (\text{II.102c})$$

In the equation, the first line Eq. (II.102a) is usually treated as a reference Hamiltonian  $H_0$  which depends only on  $\rho_0$ :

$$H_0 = -\frac{\nabla^2}{2} + V_{\text{ext}}(\vec{r}) + \int' \frac{\rho'_0}{|\vec{r} - \vec{r}'|} + V_{\text{xc}}[\rho_0] \quad (\text{II.103})$$

The second line Eq. (II.102b) is denoted as the repulsive contribution  $E_{\text{rep}}$ , which is strictly pairwise, repulsive and short ranged. And, the last line Eq. (II.102c) is denoted as  $E_{2\text{nd}}$ .

## NON-SCC DFTB THEORY

In fact, the standard DFTB, zeroth-order non-SCC approach, is to neglect the  $E_{2\text{nd}}$  term. Further, a frozen-core approximation usually is applied to reduce the computational effort by only considering the valence orbitals. Thus the core-core repulsion in Eq. (II.102a) is a sum of one- and two-body potentials [71] and the total energy becomes

$$E_0^{\text{TB}} = \sum_i^{\text{occ}} \langle \Psi_i | H_0 | \Psi_i \rangle + E_{\text{rep}} \quad (\text{II.104})$$

The KS equations are solved by the linear combination of atomic orbitals (LCAO) method. Here the single-particle wave function  $\Psi_i$  is expanded into the atomic valence orbitals:

$$\Psi_i(\vec{r}) = \sum_{\nu} b_{\nu i} \varphi_{\nu}(\vec{r} - \vec{R}_A) \quad (\text{II.105})$$

By applying the linear variational principle to Eq. (II.104), the non-SCC KS equation in the atomic basis reads

$$\sum_{\nu}^M b_{\nu i} (H_{\mu\nu}^0 - \varepsilon_i S_{\mu\nu}) = 0, \quad \forall \mu, i, \quad (\text{II.106})$$

$$H_{\mu\nu}^0 = \langle \varphi_{\mu} | H_0 | \varphi_{\nu} \rangle, \quad S_{\mu\nu} = \langle \varphi_{\mu} | \varphi_{\nu} \rangle, \quad \forall \mu \in A, \nu \in B \quad (\text{II.107})$$

For the Hamiltonian matrix elements  $H_{\mu\nu}^0$  the following form is used [72]:

$$H_{\mu\nu}^0 = \begin{cases} \varepsilon_{\mu}^{\text{neutral free atom}} & \text{if } \mu = \nu \\ \langle \varphi_{\mu}^A | T + V_0^A + V_0^B | \varphi_{\nu}^B \rangle & \text{if } A \neq B \\ 0 & \text{otherwise} \end{cases} \quad (\text{II.108})$$

with  $T$  is the kinetic energy. Since the wavefunctions  $\varphi_{\mu}$  and atomic potentials  $V_0$  are centred on the atoms, only two-center Hamiltonian matrix elements are evaluated in combination with the two-center overlap matrix elements. The diagonal elements give the energy of the free atoms to guarantee the correct limit of isolated atoms.

By solving Eq. (II.106), the total energy becomes a sum over all occupied KS orbitals  $\varepsilon_i$  with the occupation number  $n_i$ . The  $E_{\text{rep}}$  can be obtained as a function of distance by taking the difference of the DFT cohesive energy such as given by a self-consistent field local-density approximation [73] and the corresponding tight binding band-structure energy for a suitable reference system

$$E_{\text{rep}}(R) = \left\{ E_{\text{DFT}}(R) - \sum_i^{\text{occ}} n_i \varepsilon_i(R) \right\} \Big|_{\text{reference system}} \quad (\text{II.109})$$

This non-SCC DFTB works very well for systems in which the polyatomic electronic density can be represented by a sum of atom-like densities, i.e. homonuclear covalent systems or highly ionic systems [74, 75, 76].

## SCC-DFTB THEORY

The error of non-SCC DFTB increases if the chemical bonding is controlled by a delicate charge balance between different atomic constituents, especially in heteronuclear molecules and polar semiconductors. For this case, long-range Coulomb interactions must be considered and  $E_{2\text{nd}}$  in Eq. (II.102c) can not be neglected [77].

To this end,  $\delta\rho$  is decomposed into atom-centred contributions  $\delta\rho_A$ , which decay fast with increasing distance from the corresponding center. This gives

$$E_{2\text{nd}} = \frac{1}{2} \sum_{A,B}^N \iint' \left( \frac{1}{|\vec{r} - \vec{r}'|} + \frac{\delta^2 E_{\text{xc}}}{\delta\rho\delta\rho'} \Big|_{\rho_0} \right) \delta\rho_A \delta\rho'_B \quad (\text{II.110})$$

where  $\delta\rho_A(\vec{r})$  can be expanded in a series of radial function  $F_{ml}^A$  and spherical function  $Y_{lm}$ :

$$\delta\rho_A(\vec{r}) = \sum_{l,m} K_{ml} F_{ml}^A(|\vec{r} - \vec{R}_A|) Y_{lm} \left( \frac{\vec{r} - \vec{R}_A}{|\vec{r} - \vec{R}_A|} \right) \quad (\text{II.111})$$

Considering the most important contributions which are coming from the monopole and thus avoiding a substantial increase in the numerical complexity of the scheme, the deviation to the reference density on atom  $A$  can be truncated after the monopole term in the multipole expansion.

$$\delta\rho_A(\vec{r}) \approx \Delta q_A F_{00}^A(|\vec{r} - \vec{R}_A|) Y_{00} \quad (\text{II.112})$$

while the total charge in the system is preserved as

$$\sum_A \Delta q_A = \int \delta \rho_A(\vec{r}) d\vec{r} \quad (\text{II.113})$$

Then the simple final expression for the second-order energy term is

$$E_{2\text{nd}} = \frac{1}{2} \sum_{A,B}^N \Delta q_A \Delta q_B \gamma_{AB} \quad (\text{II.114})$$

where

$$\begin{aligned} \gamma_{AB} &= \iint' \left( \frac{1}{|\vec{r} - \vec{r}'|} + \left. \frac{\delta^2 E_{\text{xc}}}{\delta \rho \delta \rho'} \right|_{\rho_0} \right) \frac{F_{00}^A(|\vec{r} - \vec{R}_A|) F_{00}^B(|\vec{r} - \vec{R}_B|)}{4\pi} \\ &= \iint' \Upsilon_A(\vec{r}) \left( \frac{1}{|\vec{r} - \vec{r}'|} + \left. \frac{\delta^2 E_{\text{xc}}}{\delta \rho \delta \rho'} \right|_{\rho_0} \right) \Upsilon_B(\vec{r}') \end{aligned} \quad (\text{II.115})$$

with

$$\Upsilon_A(\vec{r}) = \frac{1}{N_A} \sum_{\mu \in A} |\varphi_\mu(\vec{r})|^2 \quad (\text{II.116})$$

The quantity  $N_A$  is the number of basis functions on atom  $A$ . To solve Eq. (II.114),  $\gamma_{AB}$  needs to be analysed. When the intratomic separation is very large ( $R = |\vec{R}_A - \vec{R}_B| \rightarrow \infty$ ), the XC term vanishes and  $E_{2\text{nd}}$  will reduce to the Coulomb interaction between two point charges  $\lim_{R \rightarrow \infty} \gamma_{AB}(R) = 1/R$ . In the opposite case, when the interatomic distance tends to zero ( $R \rightarrow 0$ ),  $\gamma_{AB}$  will describe the electron-electron interaction within the atom  $A$  and can be related to the chemical hardness  $\eta_A$  or Hubbard parameter  $\gamma_{AA} = 2\eta_A = U_A$ . Based on Pariser's observation [78],  $\gamma_{AA}$  can be approximated by the difference of the atomic ionization potential  $I_A$  and the electron affinity  $A_A$ ,  $\gamma_{AA} \approx I_A - A_A \approx 2\eta_A \approx U_A$ . The  $\gamma_{AB}$  only depend on the distance between the atoms  $A$  and  $B$ , and the parameters  $U_A$  and  $U_B$ , which means  $\gamma_{AB}(R) = \gamma_{AB}(U_A, U_B, R)$ . But these parameters are neither adjustable nor empirical values. In fact the necessary corrections for the TB energy by the charge fluctuations turns out to be a typical Hubbard-type correlation in combination with a long-range interatomic Coulomb interaction.

Finally, the total energy of Eq. (II.102) in second order DFTB is

$$E_2^{\text{TB}} = \sum_i^{\text{occ}} \langle \Psi_i | H_0 | \Psi_i \rangle + \frac{1}{2} \sum_{A,B}^N \gamma_{AB} \Delta q_A \Delta q_B + E_{\text{rep}} \quad (\text{II.117})$$

As mentioned in the previous subsection, the contribution to  $H_0$  depends only on the  $\rho_0$ . The atomic charges are only related to the single-particle wave functions  $\Psi_i$ . The self-consistent procedure is to find a minimum for Eq. (II.117) by adjusting the charge fluctuations  $\Delta q_A$ .

To solve the problem, the single-particle wave function can be expanded as the same form

like Eq. (II.105). Then the charge localized on the atom  $A$  is

$$q_A = \sum_i^{\text{occ}} \int_{V_A} |\Psi_i(\vec{r})|^2 d\vec{r} = \sum_i^{\text{occ}} \sum_{\mu\nu} b_{\mu i}^* b_{\nu i} \int_{V_A} \varphi_\mu^*(\vec{r}) \varphi_\nu(\vec{r}) d\vec{r} \quad (\text{II.118})$$

where the integrations is over the volume  $V_A$  belong to atom  $A$ . Let's consider three cases : 1) If neither  $\mu$  nor  $\nu$  belong to atom  $A$ , there is no contribution for  $q_A$ ; 2) If  $\mu$  and  $\nu$  both belong to atom  $A$ , the integration becomes  $\delta_{\mu\nu}$ , because the orbitals  $\varphi_\nu$  are orthonormal on the same atom; 3) If only one of  $\mu$  and  $\nu$  belong to atom  $A$ , i.e.  $\mu$  belongs to atom  $A$  and  $\nu$  belongs to atom  $B$ , then the integral becomes

$$\int_{V_A} \varphi_\mu^*(\vec{r}) \varphi_\nu(\vec{r}) d\vec{r} \approx \frac{1}{2} \int_V \varphi_\mu^*(\vec{r}) \varphi_\nu(\vec{r}) d\vec{r} = \frac{1}{2} S_{\nu\mu} \quad (\text{II.119})$$

and the Mulliken charge is approximated [79] as

$$q_A = \sum_i^{\text{occ}} \sum_{\mu \in A} \sum_{\nu} \frac{1}{2} (b_{\mu i}^* b_{\nu i} S_{\mu\nu} + b_{\mu i} b_{\nu i}^* S_{\nu\mu}) \quad (\text{II.120})$$

The charge fluctuation is  $\Delta q_A = q_A - q_A^0$ , if the charge of atom  $A$  in the reference system is  $q_A^0$ .

Inserting the LCAO expansion into Eq. (II.117), one obtains

$$\sum_{\nu}^M b_{\nu i} (H_{\mu\nu} - \varepsilon_i S_{\mu\nu}) = 0, \quad \forall \mu, i, \quad (\text{II.121})$$

$$\begin{aligned} H_{\mu\nu} &= \langle \varphi_\mu | H_0 | \varphi_\nu \rangle + \frac{1}{2} S_{\mu\nu} \sum_{\xi}^N (\gamma_{A\xi} + \gamma_{B\xi}) \Delta q_{\xi} \\ &= H_{\mu\nu}^0 + H_{\mu\nu}^1 \quad \forall \mu \in A, \nu \in B \end{aligned} \quad (\text{II.122})$$

When there are local external potentials  $V_{\text{ext}}^A$  on the atoms  $A$ , then in the spirit of two-center approximation Eq. (II.122) will become

$$\begin{aligned} H_{\mu\nu} &= H_{\mu\nu}^0 + H_{\mu\nu}^1 + \int \varphi_\mu^*(\vec{r}) V_{\text{ext}}(\vec{r}) \varphi_\nu(\vec{r}) d\vec{r} \\ &\approx H_{\mu\nu}^0 + H_{\mu\nu}^1 + V_{\text{ext}}^A \int_{V_A} \varphi_\mu^* \varphi_\nu + V_{\text{ext}}^B \int_{V_B} \varphi_\mu^* \varphi_\nu \\ &\approx H_{\mu\nu}^0 + H_{\mu\nu}^1 + \frac{1}{2} (V_{\text{ext}}^A + V_{\text{ext}}^B) S_{\mu\nu} \quad \forall \mu \in A, \nu \in B \end{aligned} \quad (\text{II.123})$$

The smoothly varying external potentials can also shift the matrix  $H_{\mu\nu}$ . Thus the SCC-DFTB based self-consistent procedure for the hybrid system, consisting of a metal NS and different molecules, is as follows: from guessed initial charge fluctuations  $\{\Delta q\}$  one can obtain  $H_{\mu\nu}^1$  by Eq. (II.122) and the external potential  $V_{\text{ext}}^A$  on atom  $A$  from the polarization potential  $V_{\text{pol}}$  by Eq. (II.84). Then by solving the Eq. (II.121), new coefficients  $\{b_{\nu i}\}$  are obtained. Finally, one obtains new charge fluctuations  $\{\Delta q\}$  and continues the iteration till self-consistency is achieved.

## 4.2 APPROXIMATE TDDFT IN AN EXTERNAL FIELD

This approximate TDDFT is a mixed quantum-classical approach to simulate the coupled dynamics of electrons and nuclei in nanoscale molecular systems [80].

In the time-dependent systems, the QM action is

$$\mathcal{A}[\Psi] = \int_{t_0}^{t_1} dt \langle \Psi(t) | i \frac{\partial}{\partial t} - H_e(t) | \Psi(t) \rangle \quad (\text{II.124})$$

with  $\Psi(t)$  and  $H_e(t)$  is the total electronic wavefunction and Hamiltonian. Based on the Runge-Gross theorem [81], there is the one-to-one correspondence between the potential  $V_{\text{ext}}(\vec{r}, t)$  and the one-body density  $\rho(\vec{r}, t)$ . And the exact density should satisfy the stationary condition  $\delta \mathcal{A}[\rho] / \delta \rho(\vec{r}, t) = 0$ . Thus in the stationary case, the time-dependent Kohn-Sham (TDKS) molecular orbitals obey the time-dependent Schrödinger equation.

Assuming that the XC contributions are local in time [82], the equation of motion is derived by applying the Lagrange formalism. The Lagrangian depending on the TDKS states  $\Psi_i(\vec{r}, t)$  and the nuclear positions  $\vec{R}_A$  reads

$$\mathcal{L} = \sum_A \frac{1}{2} M_A \dot{\vec{R}}_A^2 - \sum_i^{\text{occ}} \langle \Psi_i(\vec{r}, t) | H[\rho](\vec{r}, t) - i \frac{\partial}{\partial t} | \Psi_i(\vec{r}, t) \rangle - E_{\text{DC}} - V_{nn} \quad (\text{II.125})$$

In this equation, the first and last term are the classical kinetic energy and interactions for nuclei, while from the TDDFT functional the remaining terms are obtained under the assumption that the XC contributions are local in time. In the adiabatic local density approximation, standard ground state functionals can be used in the time dependent case simply replaced by the time dependent density. In addition  $E_{\text{DC}}$  comprises the double counting terms

$$E_{\text{DC}} = -\frac{1}{2} \iint' \frac{\rho(\vec{r}, t) \rho(\vec{r}', t)}{|\vec{r} - \vec{r}'|} + E_{\text{xc}}[\rho] - \int V_{\text{xc}}[\rho] \rho(\vec{r}, t) \quad (\text{II.126})$$

Eq. (II.125) can be solved in the spirit of DFTB. First, the electronic density is written as the sum of a reference density  $\rho_0(\vec{r})$ , which is given as a superposition of atomic (ground state) densities, and the deviation to the actual density, i.e. the fluctuation density  $\delta\rho(\vec{r}, t)$ :

$$\rho(\vec{r}, t) = \rho_0(\vec{r}) + \delta\rho(\vec{r}, t) \quad (\text{II.127})$$

Next Eq. (II.125) is expanded in second order as

$$\mathcal{L} \approx \sum_A \frac{1}{2} M_A \dot{\vec{R}}_A^2 - \sum_i^{\text{occ}} \langle \Psi_i(\vec{r}, t) | H[\rho_0](\vec{r}) - i \frac{\partial}{\partial t} | \Psi_i(\vec{r}, t) \rangle \quad (\text{II.128a})$$

$$+ \frac{1}{2} \iint' \frac{\rho_0(\vec{r}) \rho_0(\vec{r}')}{|\vec{r} - \vec{r}'|} - E_{\text{xc}}[\rho_0] + \int v_{\text{xc}}[\rho_0] \rho_0(\vec{r}) - V_{nn} \quad (\text{II.128b})$$

$$- \frac{1}{2} \iint' \left( \frac{1}{|\vec{r} - \vec{r}'|} + \frac{\delta v_{\text{xc}}[\rho](\vec{r}, t)}{\delta \rho(\vec{r}', t)} \right) \delta\rho(\vec{r}, t) \delta\rho(\vec{r}', t) \quad (\text{II.128c})$$

In Eq. (II.128a) the second term contains all the contributions linear in  $\delta\rho$  through the TDKS states. The terms in Eq. (II.128b) are denoted as  $E_{\text{rep}}$ .  $E_{\text{rep}}$  is a sum of strictly pairwise,



repulsive, and short ranged potentials, which is only a functional of the atomic species and the interatomic distance in the frozen-core approximation. Since  $E_{\text{rep}}$  only depends on the time independent reference density  $\rho_0$ , it is exactly the same as used in the ground state DFTB scheme. The terms in Eq. (II.128c) are of second order in  $\delta\rho$  and will be called  $E_{2\text{nd}}(t)$ .

Since  $H[\rho_0](\vec{r})$  and  $E_{\text{rep}}$  are independent on the time, the KS equations can be solved based on the LCAO method. Therefore the single-particle wave function  $\Psi_i(\vec{r}, t)$  is expanded in the basis of non-orthogonal atomic orbitals  $\varphi_\mu$  with time-dependent coefficients  $b_{\mu i}(t)$ :

$$\Psi_i(\vec{r}, t) = \sum_{\mu} b_{\mu i}(t) \varphi_{\mu}(\vec{r} - \vec{R}_A) \quad (\text{II.129})$$

Using arguments similar to the discussion of Eq. (II.114) in SCC-DFTB, the second order term of Eq. (II.128c) is approximated as follows:

$$E_{2\text{nd}}(t) \approx -\frac{1}{2} \sum_{AB} \Delta q_A(t) \gamma_{AB} \Delta q_B(t) \quad (\text{II.130})$$

where the Mulliken charge fluctuation  $\Delta q_A(t)$  is  $\Delta q_A(t) = q_A(t) - q_A^0$ . And  $q_A^0$  is the Mulliken charge for the free atom. In this basis, the Mulliken charge on atom  $A$  becomes

$$q_A(t) = \frac{1}{2} \sum_i^{\text{occ}} \sum_{\mu \in A, \nu} (b_{\mu i}^*(t) b_{\nu i}(t) S_{\mu\nu} + b_{\nu i}^*(t) b_{\mu i}(t) S_{\nu\mu}) \quad (\text{II.131})$$

Inserting Eq. (II.129) and Eq. (II.130) into Eq. (II.128),  $\mathcal{L}$  is obtained as a function of the nuclear position  $\vec{R}$  and the time-dependent coefficients  $b_{\mu i}$  as

$$\begin{aligned} \mathcal{L}(b_{\mu, i}, \vec{R}_A) = & \sum_A \frac{1}{2} M_A \dot{\vec{R}}_A^2 - E_{\text{rep}} - \frac{1}{2} \sum_{AB} \Delta q_A(t) \gamma_{AB} \Delta q_B(t) \\ & - \sum_i^{\text{occ}} \sum_{\mu\nu} \left[ b_{\mu i}^* (H_{\mu\nu}^0 - i\langle \varphi_{\mu} | \dot{\varphi}_{\nu} \rangle) b_{\nu i} - i b_{\mu i}^* S_{\mu\nu} \dot{b}_{\nu i} \right] \end{aligned} \quad (\text{II.132})$$

Note that the atom-centred basis functions  $\varphi_{\mu}$  implicitly depend on time due the motion of the nuclei. In fact, based on the chain rule for differentiation of the basis function, one can find the derivative

$$\frac{d}{dt} \frac{\partial \mathcal{L}}{\partial \dot{b}_{\mu i}^*} = \frac{\partial \mathcal{L}}{\partial b_{\mu i}^*} = 0 \quad (\text{II.133})$$

and

$$\frac{\partial \mathcal{L}}{\partial b_{\mu i}^*} = - \sum_i^{\text{occ}} \sum_{\nu} \left[ (H_{\mu\nu}^0 - i\langle \varphi_{\mu} | \dot{\varphi}_{\nu} \rangle) b_{\nu i} - i S_{\mu\nu} \dot{b}_{\nu i} + \frac{1}{2} S_{\mu\nu} b_{\nu i} \sum_{\xi} (\gamma_{A\xi} + \gamma_{B\xi}) \Delta q_{\xi} \right] \quad (\text{II.134})$$

Finally the electronic motion follows from

$$\dot{b}_{\nu i} = - \sum_{\delta\mu} S_{\mu\delta}^{-1} \left[ i H_{\delta\mu} + \sum_A \dot{\vec{R}}_A \langle \varphi_{\delta} | \frac{\partial}{\partial \vec{R}_A} \varphi_{\mu} \rangle \right] b_{\mu i} \quad (\text{II.135})$$

with

$$\begin{aligned}
 H_{\mu\nu} &= \langle \varphi_\mu | H[\rho_0] | \varphi_\nu \rangle + \frac{1}{2} S_{\mu\nu} \sum_{\xi} (\gamma_{A\xi} + \gamma_{B\xi}) \Delta q_{\xi}(t) \\
 &= H_{\mu\nu}^0 + H_{\mu\nu}^1; \quad \forall \mu \in A; \nu \in B
 \end{aligned} \tag{II.136}$$

By the same procedure, the force on the atom  $A$  is

$$\begin{aligned}
 M_A \ddot{\vec{R}}_A &= - \sum_i^{\text{occ}} \sum_{\mu\nu} b_{\mu i}^* b_{\nu i} \left( \frac{\partial H_{\mu\nu}^0}{\partial \vec{R}_A} + \frac{\partial S_{\mu\nu}}{\partial \vec{R}_A} \sum_B \gamma_{AB} \Delta q_B \right) \\
 &+ \sum_i^{\text{occ}} \sum_{\mu\nu\delta\xi} \left( b_{\mu i}^* \langle \frac{\partial \varphi_\mu}{\partial \vec{R}_A} | \varphi_\nu \rangle S_{\nu\delta}^{-1} H_{\delta\xi} b_{\xi i} + c.c. \right) \\
 &- \Delta q_A \sum_B \frac{\partial \gamma_{AB}}{\partial \vec{R}_A} \Delta q_B - \frac{\partial E_{\text{rep}}}{\partial \vec{R}_A}
 \end{aligned} \tag{II.137}$$

In order to simulate the interaction with external electromagnetic fields, the Hamiltonian (II.136) needs to be supplemented by respective terms. This is usually achieved by substituting the momentum  $\vec{p}$  by the generalized form  $\vec{p} - \vec{A}$ , where  $\vec{A}(\vec{r}, t)$  is the vector potential of the external field. Since the LCAO basis functions for the DFTB method are known, one can get the matrix elements of the Hamiltonian  $H \left[ \vec{r}, \vec{p} - \frac{e}{c} \vec{A} \right]$  by numerical integration and use it to propagate the wave function. Using the approximation of the time-dependent matrix elements proposed by Graf and Vogl [83], the Hamiltonian is

$$H \left[ \vec{r}, \vec{p} - \vec{A}(\vec{r}, t) \right] = \exp \left[ i \int^{\vec{r}} \vec{A}(s, t) ds \right] H(\vec{r}, \vec{p}) \exp \left[ -i \int^{\vec{r}} \vec{A}(s, t) ds \right] \tag{II.138}$$

Since the wavelengths of the fields studied here are much larger than the molecular size ( $\lambda > 100\text{nm}$ ), the vector potential can be approximated as constant in the integration region, which means  $\int^{\vec{R}_A} \vec{A}(s, t) ds \approx \vec{A}(t) \vec{R}_A$ . Then the time-dependent Hamiltonian matrix elements are

$$\begin{aligned}
 H_{\mu\nu} \left[ \vec{r}, \vec{p}, \vec{A}(t) \right] &= \int \varphi_\mu(\vec{r} - \vec{R}_A) H(\vec{r}, \vec{p} - \vec{A}) \varphi_\nu(\vec{r} - \vec{R}_B) d\vec{r} \\
 &= \int \varphi_\mu \exp \left[ i \int^{\vec{r}} \vec{A}(t) ds \right] H(\vec{r}, \vec{p}) \exp \left[ -i \int^{\vec{r}} \vec{A}(t) ds \right] \varphi_\nu d\vec{r} \\
 &= \exp \left[ i \int^{\vec{R}_A} \vec{A}(s, t) ds \right] \exp \left[ -i \int^{\vec{R}_B} \vec{A}(s, t) ds \right] \int \varphi_\mu H(\vec{r}, \vec{p}) \varphi_\nu d\vec{r} \\
 &= \exp \left[ i(\vec{R}_A - \vec{R}_B) \vec{A}(t) \right] H_{\mu\nu}[\vec{r}, \vec{p}] \quad \mu \in A, \nu \in B
 \end{aligned} \tag{II.139}$$

Below, a hybrid system in the induced field is studied by the following steps: first, one obtains the self-consistent result for the hybrid system without the induced field according to Section II.4.1. Second, the total field  $\vec{E}_{\text{tot}}^{\text{f}}$  induced by the external field  $\vec{E}_{\text{ext}}$  is obtained by Eq. (II.91). Finally, the propagation of the electronic states of the molecule in the total field is obtained by Eq. (II.139).

---

## Chapter III

# Dissipative Exciton Dynamics in LH Complexes

### 1 VIBRATIONAL AND VIBRONIC COHERENCES IN FMO COMPLEX

In recent years, the energy transfer and the spectroscopy of photosynthetic light-harvesting pigment-protein complexes [65] triggered substantial interest. Here the FMO complex has played a prominent role.

The FMO complex, which consists of three identical subunits, serves as an energy funnel linking the light-harvesting chlorosome with the RC in green sulphur bacteria [84]. Every subunit is formed by an aggregate of seven BChl *a* molecules as shown in Fig. III.1, which are embedded in a protein environment [85]. In fact, there is an eighth BChl *a* molecule, which will not be considered here. For the FMO a comparison between the electronic energy level structure and the experimentally determined spectral density [86] suggested a mode around  $180\text{ cm}^{-1}$  to fulfil the conditions for reasonably strong mixing between excitonic and vibronic (i.e. local electron vibrational) excitations or, in terms of dynamics, for vibrationally assisted exciton transfer [87].

In system-bath approaches by construction the dynamics is obtained explicitly only for the relevant system, whereas the bath is traced out in the RDO [64]. With recent advances in the numerical solution of the Schrödinger equation for high-dimensional Hamiltonians by means of the multi-layer multi-configuration time-dependent Hartree method [88] it became possible to approach exciton–vibrational dynamics in the FMO complex by discretization of the spectral density yielding a high-dimensional model [89]. Here, indeed it has been found that vibrational modes in a window around  $180\text{ cm}^{-1}$  are appreciably excited in both the electronic ground and excited states. It should be noted that the model of Ref. [89] applies to the zero temperature case and the description of relaxation is limited by the finite discretization of the bath. In order to have a proper description of relaxation while having access to the dynamics of vibrational degrees of freedom, models have been suggested where a single vibrational mode is kept “active” as part of the relevant system. The latter has been either a molecular dimer [90, 91] or a model of the FMO complex [36, 92].

In the present section such an extended relevant system is investigated using a QME, as introduced in Sec. II.2.2. Sacrificing the non-Markovian and non-perturbative treatment of

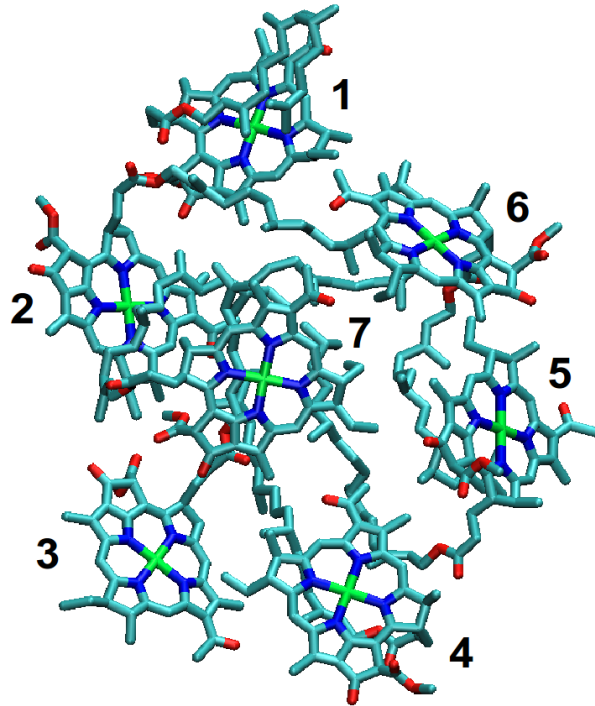


Figure III.1: Structure of the monomeric subunit of the FMO complex of *Prothecochloris aestuarii* formed by seven BChl *a* molecules (labelled) embedded in a protein environment of folded  $\alpha$ -sheets (not shown).

most of the bath (except for the modes which are part of the relevant system), allows us to focus on the difference between OPA and TPA. Working within the TPA gives further access not only to the vibronic (as in OPA), but also to the vibrational coherences. Indeed, in view of the results of Ref. [89] the inclusion of vibrational motion in the local electronic ground states appears to be mandatory. Emphasis is put on the effect from the vibrational coherence on the exciton transfer. The present focus is on the dynamics of the RDM and not on spectroscopic signals.

### 1.1 FMO MODEL

The Hamiltonian can be written in system-bath form as Eq. (II.37). In the following two models are considered: First, only the exciton subspace is taken as the relevant system (model I). From Eq. (II.18), the system Hamiltonian without ground state represents

$$H_S^{(1)} = \sum_{mn} (E_m \delta_{mn} + J_{mn}) |m\rangle \langle n| \quad (\text{III.1})$$

where  $E_m$  is the site energy and  $J_{mn}$  the Coulomb coupling between sites  $m$  and  $n$  taken from Ref. [93] as (in units of  $\text{cm}^{-1}$ )

$$H_S^{(I)} = \begin{pmatrix} 310 & -97.9 & 5.5 & -5.8 & 6.7 & -12.1 & -10.3 \\ -97.9 & 230 & 30.1 & 7.3 & 2.0 & 11.5 & 4.8 \\ 5.5 & 30.1 & 0 & -58.8 & -1.5 & -9.6 & 4.7 \\ -5.8 & 7.3 & -58.5 & 180 & -64.9 & -17.4 & -64.4 \\ 6.7 & 2.0 & -1.5 & -64.9 & 405 & 89.0 & -6.4 \\ -12.1 & 11.5 & -9.6 & -17.4 & 89.0 & 320 & 31.7 \\ -10.3 & 4.8 & 4.7 & -64.4 & -6.4 & 31.7 & 270 \end{pmatrix}$$

In the Hamiltonian, the site energies  $E_m$  are obtained from quantum chemical/electrostatic calculations. And the Coulomb couplings  $J_{mn}$  are calculated in the dipole-dipole approximation. The labelling of the sites follows the structure of the Hamiltonian matrix, e.g., site  $m = 3$  has the lowest energy  $12195 \text{ cm}^{-1}$  which is taken as zero energy in the above.

In the second case (model II) each site  $m$  contains a single intramolecular harmonic vibrational mode with coordinate  $Q_m^{(H)}$ , frequency  $\Omega_m^{(H)}$ , and Huang-Rhys factor  $S_m^{(H)}$ . From Eq. (II.34), the Hamiltonian reads:

$$H_S^{(II)} = \sum_m \sum_{\mathbf{M}} E_{m,\mathbf{M}} |m, \mathbf{M}\rangle \langle m, \mathbf{M}| + \sum_{m \neq n} \sum_{\mathbf{M}, \mathbf{N}} J_{mn} (\text{FC})_{\mathbf{M}\mathbf{N}} |m, \mathbf{M}\rangle \langle n, \mathbf{N}| \quad (\text{III.2})$$

In the spirit of the  $n$ -particle approximation, the OPA and TPA as shown in Fig. II.1 are used. To reduce the unnecessary calculations, the maximum vibrational quantum numbers  $\{\mathbf{M}\}$  act as a convergence criterion with regard to the basis size in the numerical simulations and have been chosen as follows. A certain upper energy limit is defined from a vertical excitation at site  $m = 1$ , i.e. if exciton-vibrational levels exceed that limit there is only little influence on the results. The FC mediated Coulomb coupling between the sites causes the situations that even if a level would be energetically accessible, the coupling is too small to lead to sizeable exciton-vibrational state mixing. This has been checked by calculating exciton-vibrational eigenstates and subsequently an additional criterion is used for restricting the state space of the dynamics simulations. The Huang-Rhys factor is so small that only a few vibronic levels are necessary to be included at the initially excited site  $m = 1$ ; the actual value is also dependent on the temperature due to the thermal population of vibrational states in the electronic ground states. At  $T = 77 \text{ K}$   $M_{e_1}^{(\max)} = 2$  is found to be sufficient, which yields for the levels included in the other sites, i.e. maximal energy for all sites with  $\{\mathbf{M}\}$  is approximately equal or below  $M_{e_1}^{(\max)} = 2$ :  $M_{e_2 \dots e_7}^{(\max)} = (3, 4, 3, 2, 2, 3)$ . In case of the TPA the electronic ground states  $M_{g_n}^{(\max)} = 2$  are used for all  $n$ . However at  $T = 300 \text{ K}$  the vibrational numbers need to be increased to  $M_{e_1 \dots e_7}^{(\max)} = (3, 4, 5, 4, 3, 3, 4)$  and  $M_{g_n}^{(\max)} = 3$ . For the chosen setups there are 133 and 338 exciton-vibrational eigenstates for  $T = 77 \text{ K}$  and  $300 \text{ K}$ , respectively. For OPA the same vibronic excitation  $M_{e_m}$  as for TPA and all  $M_{g_n} = 0$  at  $T = 77 \text{ K}$  and  $300 \text{ K}$ .

For both cases the bath, which contains solvent and protein environment as well as further intramolecular vibrations, is represented by a set of uncoupled harmonic oscillators with

dimensionless coordinates  $\{x_i\}$ , and frequencies  $\{\omega_i\}$ , i.e.

$$H_B = \sum_i \frac{\omega_i}{2} \left( -\frac{\partial^2}{\partial x_i^2} + x_i^2 \right) \quad (\text{III.3})$$

The system-bath coupling for model I is given by

$$H_{S-B}^{(I)} = \sum_{m,i} \omega_i g_i x_i |m\rangle \langle m| \quad (\text{III.4})$$

The dimensionless coupling constant  $g_i$  is simply assumed to be independent of the site (see the study of the site dependence in Ref. [94]). Based on a fit of low temperature fluorescence line narrowing spectra of B777 complexes by Renger and Marcus [95], the spectral density is suggested as

$$J^{(I)}(\omega) = \sum_{i=1,2} \frac{s_i}{7!} \frac{\omega^3}{2\omega_i^4} e^{-\sqrt{\omega/\omega_i}} \quad (\text{III.5})$$

where  $s_1 = 0.8$ ,  $s_2 = 0.5$ ,  $\omega_1 = 0.6 \text{ cm}^{-1}$ , and  $\omega_2 = 1.9 \text{ cm}^{-1}$  [95].

The above spectral model has been extended by Renger and Adolphs in Ref. [96] by adding a discrete mode. Thus the spectral density yields

$$J(\omega) = S_0 J^{(I)}(\omega) + S^{(H)} \delta(\omega - \Omega^{(H)}) \quad (\text{III.6})$$

The parameters  $\Omega^{(H)} = 180 \text{ cm}^{-1}$  and  $S^{(H)} = 0.22$  had been chosen for the vibrational mode, together with a Huang-Rhys factor  $S_0 = 0.5$  for the protein environment. Later it was suggested that this vibrational mode was considered as a mode which effectively combined three modes around  $180 \text{ cm}^{-1}$  yielding a reduced Huang-Rhys factor of  $S^{(H)} = 0.027$  (see, e.g., Ref. [36]).

Following Nalbach and coworkers [36, 92], one extends the model behind Eq. (III.6) and includes a damping of this effective mode. This is accomplished by choosing the system-bath Hamiltonian for model II as follows:

$$H_{S-B}^{(II)} = \sum_{m,i} [c_i \Omega^{(H)} ((Q_m^{(H)} - \sqrt{2S^{(H)}})|e_m\rangle \langle e_m| + Q_m^{(H)}|g_m\rangle \langle g_m|) x_i + \omega_i g_i x_i] |m\rangle \langle m| \quad (\text{III.7})$$

This coupling Hamiltonian contains two contributions, where the coupling strengths are assumed to be independent on the site. First, the coupling between the electronic excitation and the protein environment is taken as in Eq. (III.5) again. Second, a bilinear coupling between the system vibrational coordinate and the bath coordinates is assumed with coupling strength  $c_i$ . Notice that the bilinear coupling is defined by the minimum of the potential for the coordinate  $Q_m^{(H)}$  in the respective electronic state. The Huang-Rhys factor for the mode  $Q_m^{(H)}$ , which determines the FC factors in Eq. (III.2), will be taken as  $S^{(H)} = 0.027$  for all sites [36].

The influence of the bilinear coupling for the selected vibrational mode from the bath is modelled by an Ohmic spectral density, i.e.

$$\omega^2 J^{(H)}(\omega) = \eta^{(H)} \omega e^{-\omega/\omega_c} \quad (\text{III.8})$$

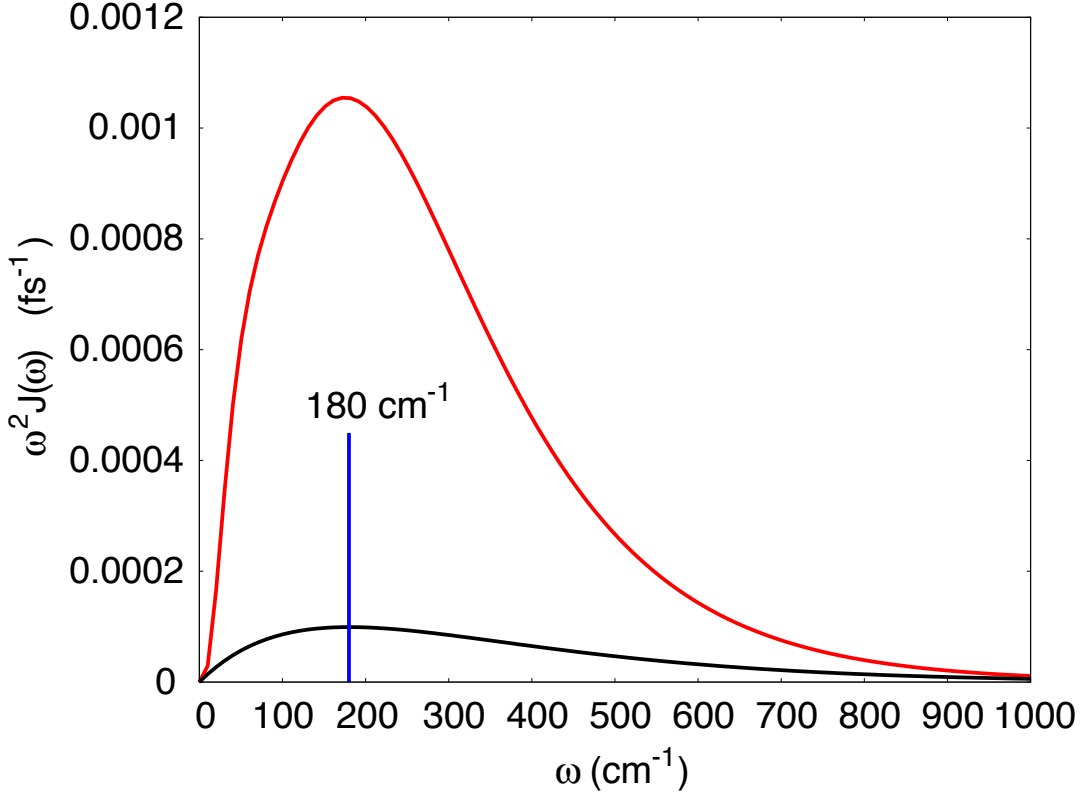


Figure III.2: The spectral density according to Renger and Marcus (red), Eq. (III.5), and the Ohmic spectral density (black), Eq. (III.8). Also shown is the position of the effective vibrational mode at  $180 \text{ cm}^{-1}$ .

with  $\eta^{(H)}=0.05$  and  $\omega_c = 180 \text{ cm}^{-1}$ . The choice of  $\omega_c$  is reasonable for the present purpose as it gives the most effective coupling, but otherwise arbitrary since nothing is known about  $J^{(H)}(\omega)$  in the FMO complex. The coupling strength  $\eta^{(H)}$  has been chosen such as to give a relaxation time 246 fs of vibrational transition from the  $M = 1$  to  $M = 0$ . A similar relaxation time has been reported in Ref. [97] for the LH1. It should be emphasized that the TPA model requires to contain a damping of the  $Q_m^{(H)}$  mode to guarantee relaxation also in the electronic ground states. In the OPA model, as a consequence of the mixing between excitonic and vibronic excitations, relaxation of vibronic excitations occurs already with the coupling according to Eq. III.1. Figure III.2 summarizes the spectral densities used in this work.

The dynamics of the two models will be investigated within the QME approach. Thereby, non-Markovian effects are neglected for model I, whereas for model II the dynamics of the selected modes is treated beyond perturbation theory and Markov approximation. This simplification allows one to address the exciton-vibrational dynamics beyond the OPA, i.e. to include vibrational motion at those sites, which are in their electronic ground states.

The system-bath couplings are of the form of Eq. (II.40). Thus the QME for the RDO  $\rho(t)$  from Eq. (II.55) becomes

$$\frac{\partial}{\partial t}\rho(t) = -i[H_S, \rho(t)] - \sum_m \left[ K_m, \Lambda_m \rho(t) - \rho(t) \Lambda_m^{(+)} \right] \quad (\text{III.9})$$

Let's specify these equations for the considered models. In model I one obtains

$$K_m^{(I)} = |m\rangle\langle m| \quad (\text{III.10})$$

whereas in model II this operator gives the full  $K_m^{(II)}$  as

$$K_m^{(II)} = \Omega^{(H)} ((Q_m^{(H)} - \sqrt{2S^{(H)}})|e_m\rangle\langle e_m| + Q_m^{(H)}|g_m\rangle\langle g_m|)|m\rangle\langle m| \quad (\text{III.11})$$

Using the spectral density models as given in Fig. III.2 one has neglected correlations between different terms in  $K_m$ , i.e.  $J_{mn}(\omega) = J(\omega)$  and accordingly  $C_{mn}(t) = C(t)$ . Further, the time evolution operator in Eq. II.53 has been evaluated in the eigenstate representation in order to guarantee proper equilibration [64]. In order to describe the effect of an energy sink at site 3, i.e. the RC, one has used the approach of Ref. [19], which treats the coupling to the sink perturbatively under the assumption of a constant spectral density of the interaction between site 3 and the sink. Thus the transfer towards the RC is treated as an incoherent population decay on a purely phenomenological level, i.e. with the sink it has

$$\frac{\partial}{\partial t}\rho(t) = -i[H_S, \rho(t)] - \sum_m [K_m, \Lambda_m\rho(t) - \rho(t)\Lambda_m^{(+)}] - \Gamma_{\text{RC}} \sum_{\mathbf{M}} |3, \mathbf{M}\rangle\langle 3, \mathbf{M}| \quad (\text{III.12a})$$

$$\frac{\partial}{\partial t}\rho_{\text{RC}}(t) = \Gamma_{\text{RC}} \sum_{\mathbf{M}} |3, \mathbf{M}\rangle\langle 3, \mathbf{M}| \quad (\text{III.12b})$$

with a constant decay rate  $\Gamma_{\text{RC}} = 1 \text{ ps}^{-1}$  [36]. In addition, the initial density  $\rho(0)$  of the system was set to  $\rho_{11}(0) = 1$  in model I. In model II in thermal equilibrium yields

$$\rho_{1\mathbf{M}, 1\mathbf{M}}(0) = \frac{\exp(-E_{1\mathbf{M}}/k_B T)}{\sum_{\mathbf{M}} \exp(-E_{1\mathbf{M}}/k_B T)} \quad (\text{III.13})$$

## 1.2 RESULTS

### EXCITON POPULATION DYNAMICS

Fig. III.3 shows the site populations  $P_m(t) = \rho_{mm}(t)$  after initial excitation at site  $m = 1$  for system-bath model I (no explicit vibrations) at two temperatures ( $T = 77$  and  $300$  K) and with/without (upper/lower panels) a sink. At  $T = 77$  K pronounced coherent oscillations are observed between the populations at site  $m = 1$  and  $m = 2$ , and similar to those reported in many other researches (see, e.g. Ref. [65]). After 5 ps the population virtually has relaxed to the lowest-energy site  $m = 3$ , with obvious population at site  $m = 4$ . At  $T = 300$  K the oscillations almost disappeared and a redistribution of population away from the exit site  $m = 3$  resulted from the Boltzmann population.

Upon inclusion of the sink attached to site  $m = 3$  (in following “with sink” means inclusion of a sink attached to site 3) one finds no appreciable change in the dynamics at sites  $m = 1, 2$ . However, the population at site  $m = 3$  decays afterwards with a maximum rate around 1400 fs. Most of the population is at the sink after 5 ps. At  $T = 300$  K a similar observation holds true with the notable exception that the rate for population of the sink is slowed down (Notice that the sink is not part of the equilibrated system). This results from the fact that more population



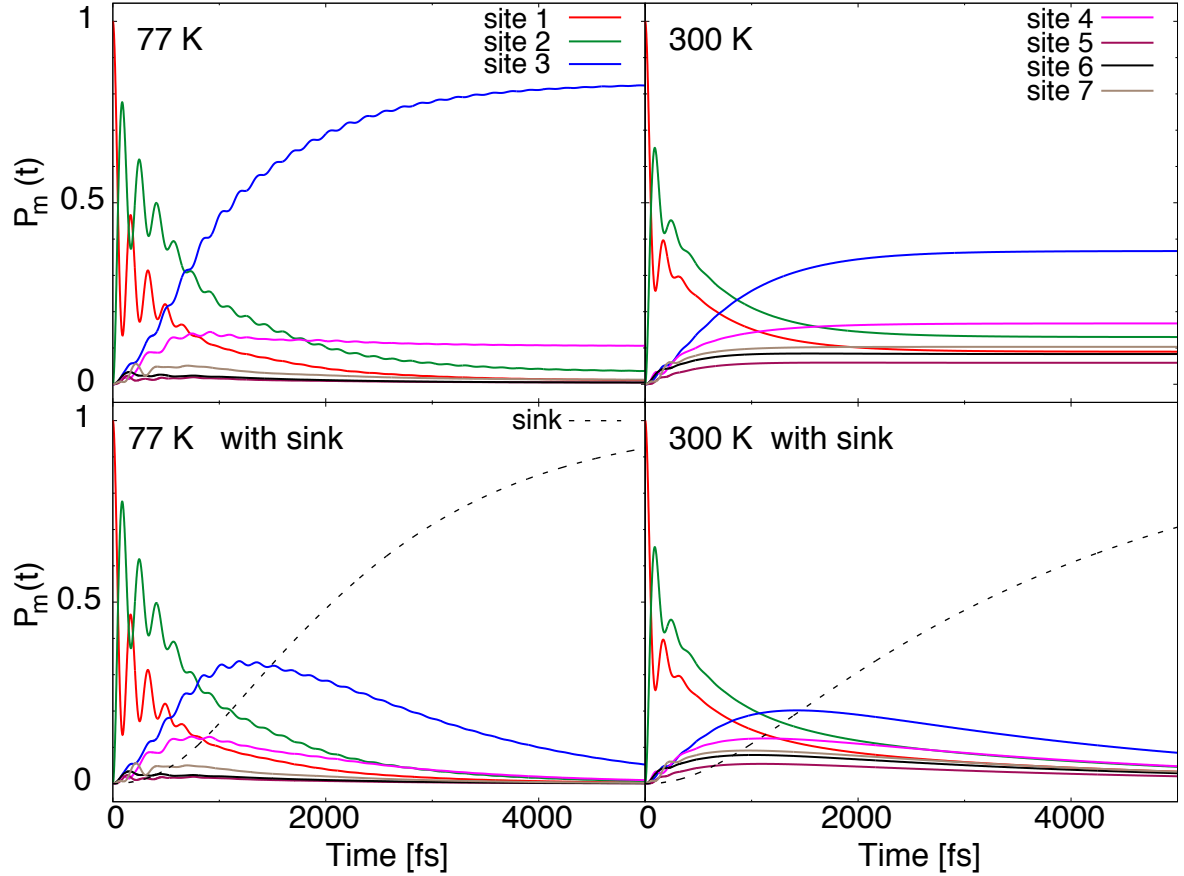


Figure III.3: Time evolution of the FMO site populations,  $P_m = \rho_{mm}$ , without explicit vibrational modes (model I) for  $T = 77\text{ K}$  (left column) and  $T = 300\text{ K}$  (right column) for the initial population  $\rho_{11}(0) = 1$ . The upper row gives the populations without the sink and the lower row with a sink attached to site  $m = 3$ .

is quickly and temporarily trapped at sites  $m = 4 - 7$ , which are not directly connected to the RC as it is the case for site  $m = 3$ . Figure III.3 will be taken as a reference for the following discussion of the influence from the inclusion of explicit vibrations.

In Fig. III.4 the TPA population dynamics of model II are compared with that of the bare electronic model I and the OPA without the sink. In total, inclusion of explicit vibrations results in changes according to the bare electronic case, which are of the order of 20% at  $T = 77\text{ K}$  and 35% at  $T = 300\text{ K}$ . Resulting from the more complicated level structure the oscillations between site  $m = 1$  and 2 are less regular, but still discernible at  $T = 77\text{ K}$ . At this temperature the vibrations accelerated clearly the trapping to the lowest site  $m = 3$ . However there is no pronounced acceleration at  $T = 300\text{ K}$ . In fact, the initial behaviour of the populations at sites  $m = 1$  and 2 indicate a transient trapping, which will be discussed below in the context of the density matrices. Comparing TPA and OPA in the lower panels of Fig. III.4 differences of about 15% and 7% are found at 77 K and 300 K, respectively. It is the most significant that the trapping to the lowest site  $m = 3$  is accelerated in the TPA as compared to the OPA at both temperatures.

Fig. III.5 compares the same population dynamics but with the sink. Overall, inclusion of

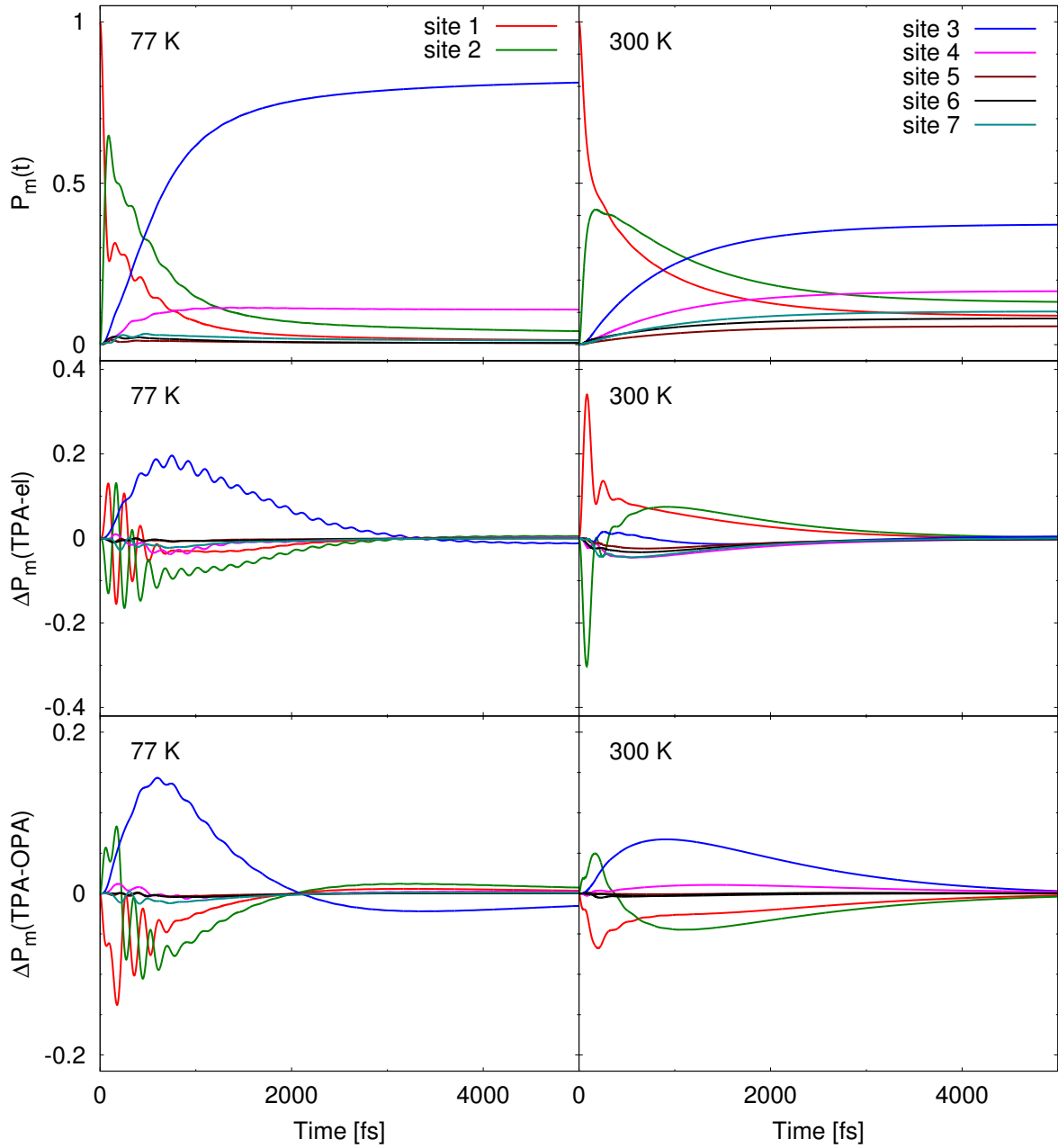


Figure III.4: Time evolution of the FMO site populations,  $P_m = \rho_{mm}$  without the sink for model II, in TPA approximation (upper panels). The population difference,  $\Delta P_m$ , with respect to the bare electronic and the OPA model is shown in the middle and lower panels, respectively. The initial condition is a vertical FC transition from the Boltzmann populated ground state at site  $m = 1$ .

explicit vibrations leads to the same changes for both the bare electronic and OPA cases. At  $T = 77$  K the change is of the order of 15%, and is 5% smaller than in the case without the sink in Fig. III.4. That is because there is an accelerated trapping at the RC with the sink from site 3, which is of the order of 15%. But there is no discernible change at  $T = 300$  K. In the lower panels comparing TPA and OPA, the RC trapping is accelerated in the TPA as compared

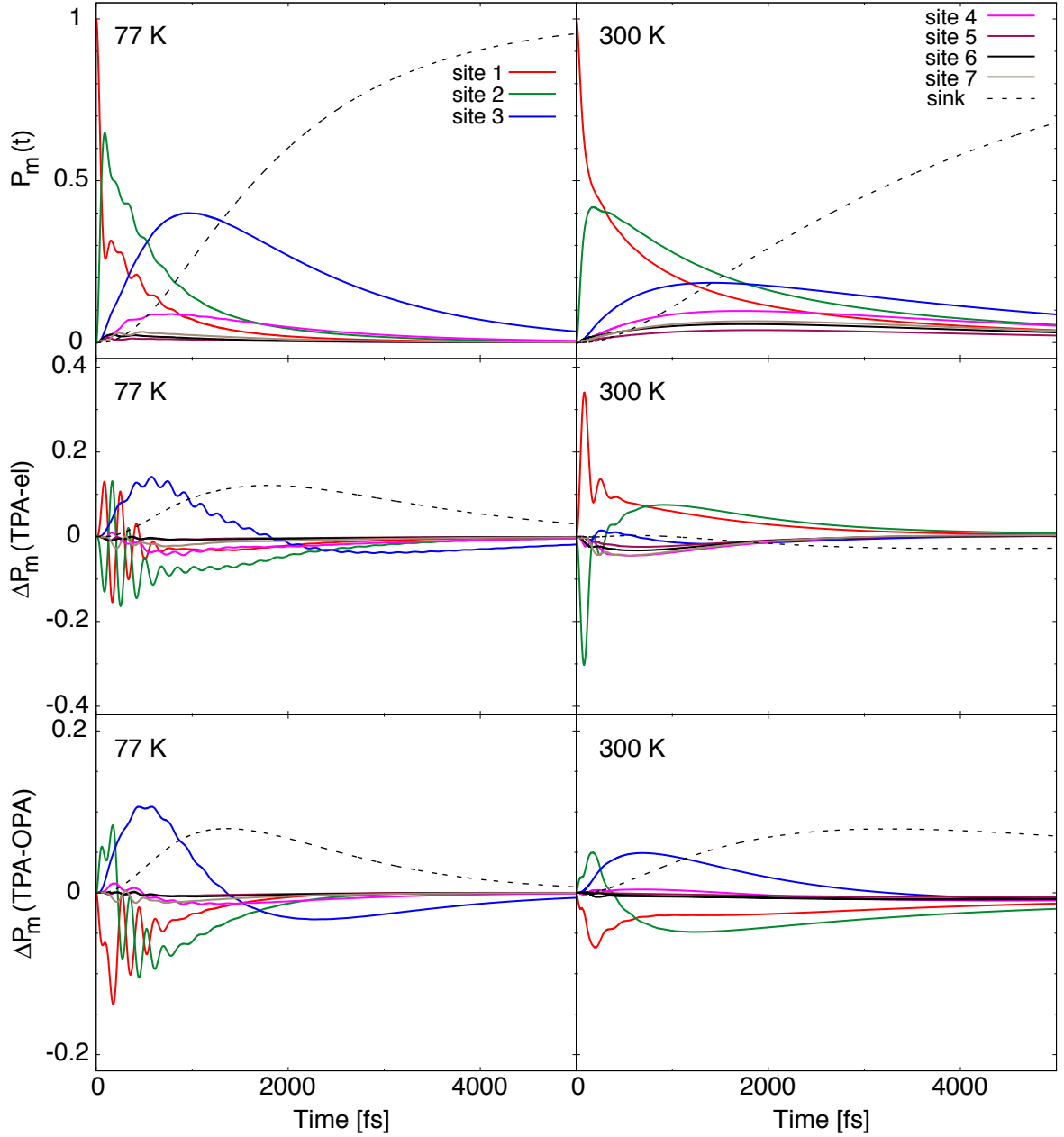


Figure III.5: Same as Fig. III.4 for system with the sink.

to the OPA at both temperatures. The difference is about 10% and 5% at 77 K and 300 K respectively. Also there are little changes at 77 K comparing with the case without the sink for the same reason. Overall the trapping at the sink doesn't change the trend of the influence of the vibrations.

Fig. III.6 shows the dependence of the population dynamics with the sink on the coupling strength  $\eta^{(H)}$  for  $T = 77$  K. At this temperature the vibrational relaxation time for the  $0 \rightarrow 1$  transition is 246 fs for the reference case  $\eta^{(H)} = 0.05$ . Panel (a) compares the population dynamics with that of  $\eta^{(H)} = 0.3$  (relaxation time 41 fs). The transition out of site 1 is decelerated in the first 200 fs, which is in the order of 14% , and then accelerated before 2000 fs in the order of 5%. During all the period the transition out from the site 2 is accelerated in the order of

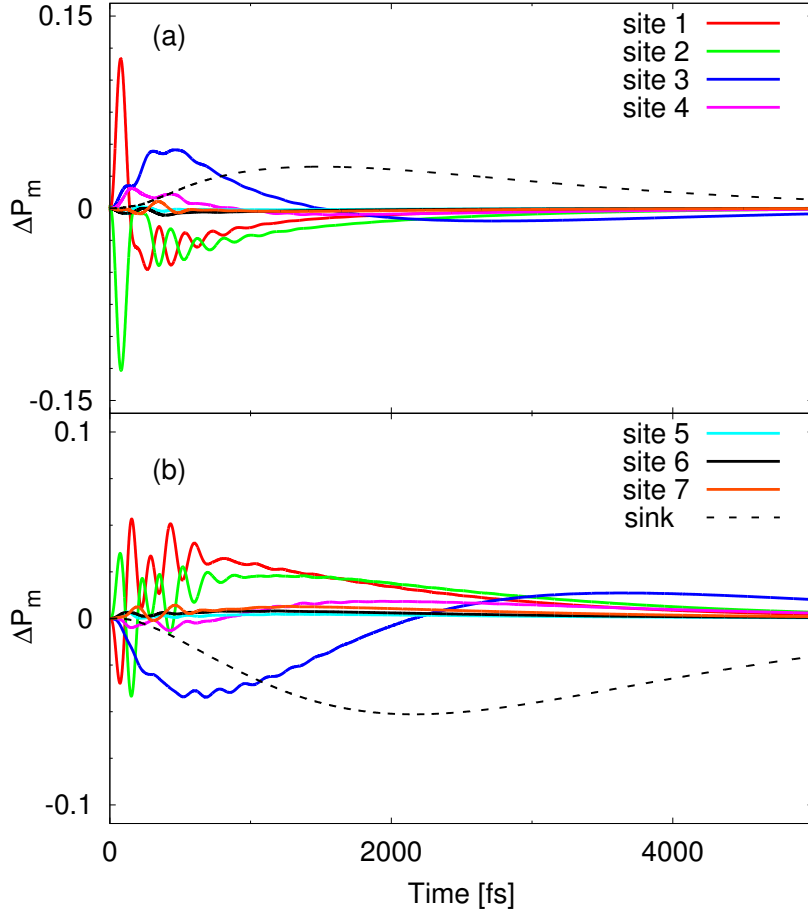


Figure III.6: Population difference of the exciton states in the local basis for different strength of the coupling  $\eta^{(H)}$  in Eq. (III.8). As a reference  $\eta^{(H)} = 0.05$  is used as before. Panel (a) and (b) show  $\Delta P_m = P_m(\eta^{(H)} = 0.3) - P_m(\eta^{(H)} = 0.05)$  and  $\Delta P_m = P_m(\eta^{(H)} = 0.005) - P_m(\eta^{(H)} = 0.05)$ , respectively. The temperature is  $T = 77$  K.

14%. Trapping at the site 3 and RC is also accelerated in the order of 5% and 3%. Panel (b) compares the population dynamics to the case of  $\eta^{(H)} = 0.005$  (relaxation time 2460 fs). For this case the transition out of the site 1 is accelerated during the first 200 fs in the order of 3% and decelerated before 2000 fs in the order of 5%. From  $t = 200$  fs to 400 fs, the transition out from site 2 is decelerated in the order of 3%. In all other period (from 0 fs to 200 fs and from 400 fs to 5000 fs) it is mostly accelerated in the order of 3% to the site 3 and RC are decelerated during all the time in the order of 5%. Overall, the changes are essentially below 10%. Decreasing the vibrational relaxation time leads to a more rapid population of site  $m = 3$  and therefore of the sink. If the relaxation time is increased the opposite behaviour is observed.

## VIBRONIC AND VIBRATIONAL DYNAMICS

The dynamics of vibronic excitations in model II is studied using the density matrix

$$\rho_{mM_{e_m}, nN_{e_n}}(t) = \sum_{M_{g_k}} \rho_{mM_{e_m} M_{g_k}, nN_{e_n} M_{g_k}}(t) \quad (\text{III.14})$$

where  $\mathbf{M}_{g_k}$  contains all vibrational quantum numbers for sites  $k \neq m, n$ . Notice that in OPA the quantum numbers are all equal to zero, however in TPA one of the  $M_{g_k}$  can be different from zero. The following results have been calculated for the case without inclusion of a sink.

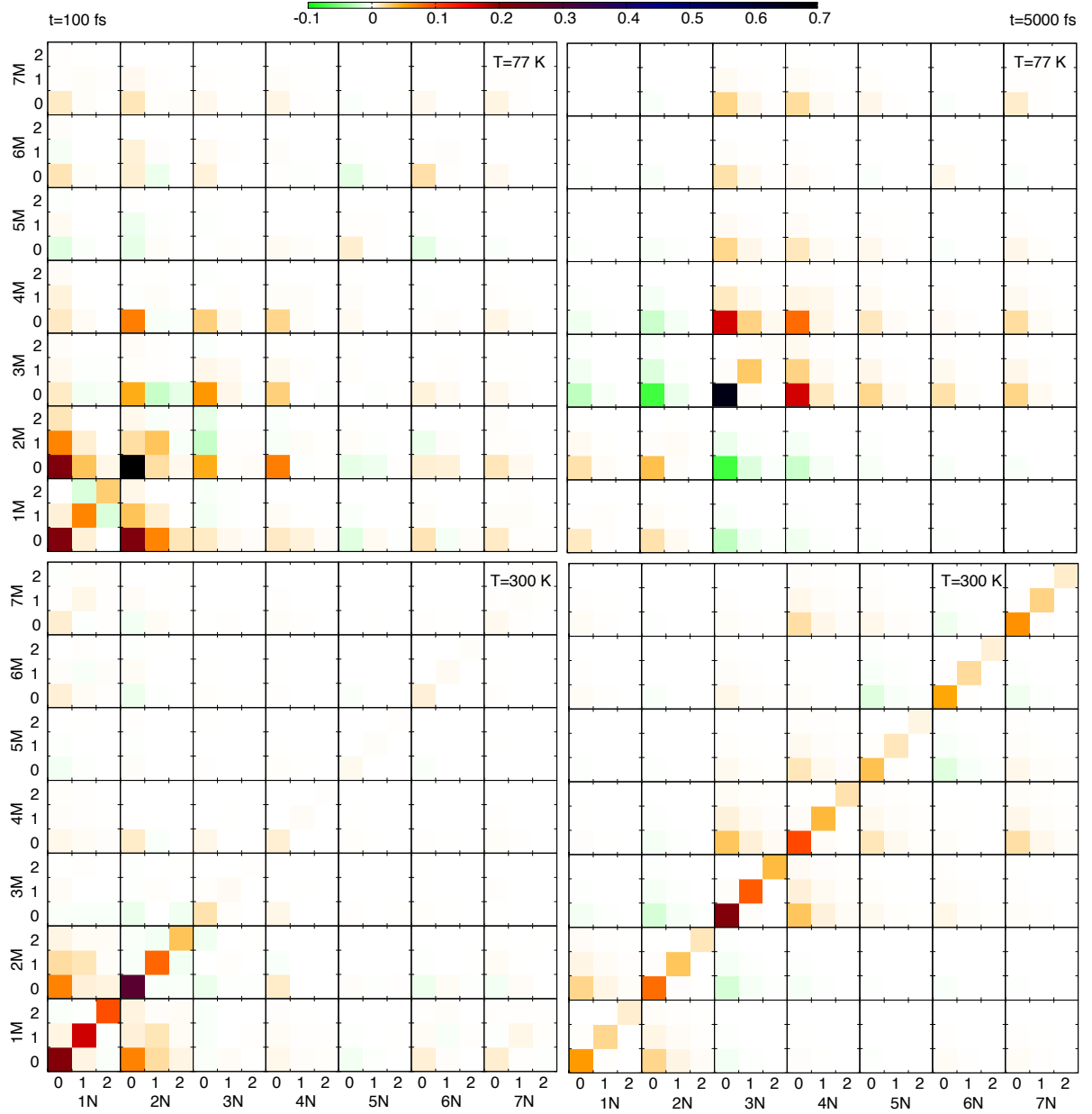


Figure III.7: Vibronic density matrix ( $\text{Re}\rho_{mM_{e_m}, nN_{e_n}}$ ) in TPA at  $t = 100$  and  $5000$  fs and for two temperatures,  $T = 77$  and  $300$  K.

The left column of Fig. III.7 shows the vibronic density matrix at  $100$  fs after an instantaneous FC transition at site  $m = 1$ . At  $T = 77$  K on-site coherences are found, which represent vibronic wave packet dynamics at sites  $m = 1$  and  $2$ . Furthermore, these sites are attached by inter-site coherences. There are weaker inter-site coherences between sites  $m = 1$  and  $2$  and essentially all other sites. Generally the inter-site coherences involving the vibronic ground state are strongest due to the smallness of the Huang-Rhys factor. If increasing the temperature to  $T = 300$  K

most of on-site and inter-site coherences are suppressed owing to the more rapid dephasing.

The right column of Fig. III.7 shows the vibronic density matrix at  $t = 5$  ps. At this time, with respect to Fig. III.3 the system is virtually equilibrated in the one-exciton vibrational manifold. Therefore, the density matrix reflects the projection of the thermally populated eigenstates onto the site basis. At  $T = 77$  K the vibronic density matrix is dominated by contributions from sites  $m = 3$  and 4, with pronounced inter-site coherences between  $m = 3$  and essentially all other sites. At  $T = 300$  K almost all sites are obviously populated with site  $m = 3$  still dominating. The almost equal population of sites causes a suppression of off-diagonal elements.

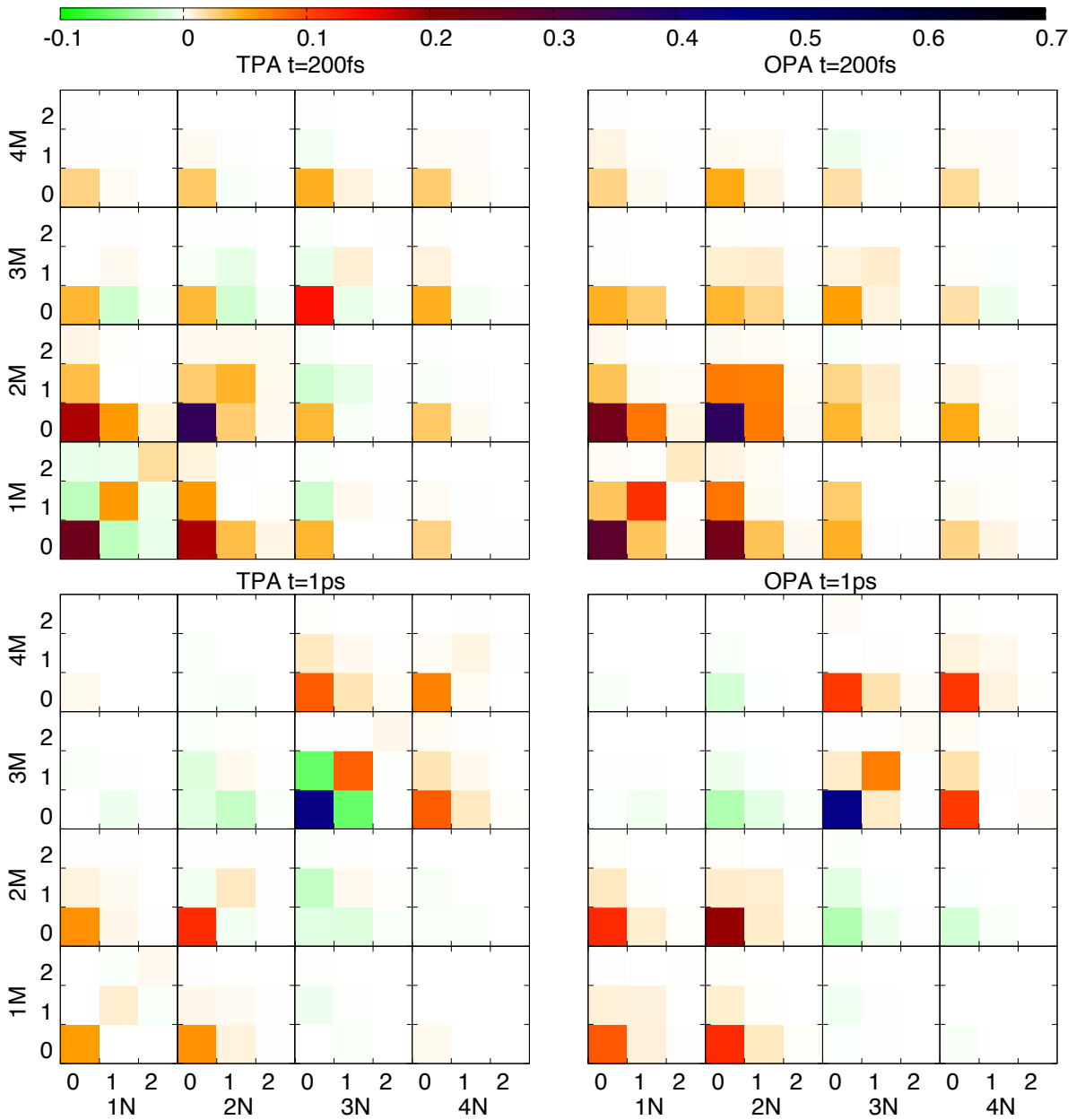


Figure III.8: Vibronic density matrix ( $\text{Re}\rho_{mM_{e_m},nN_{e_n}}$ ) in TPA and OPA at  $t = 200$  and  $1000$  fs and for  $T = 77$  K.

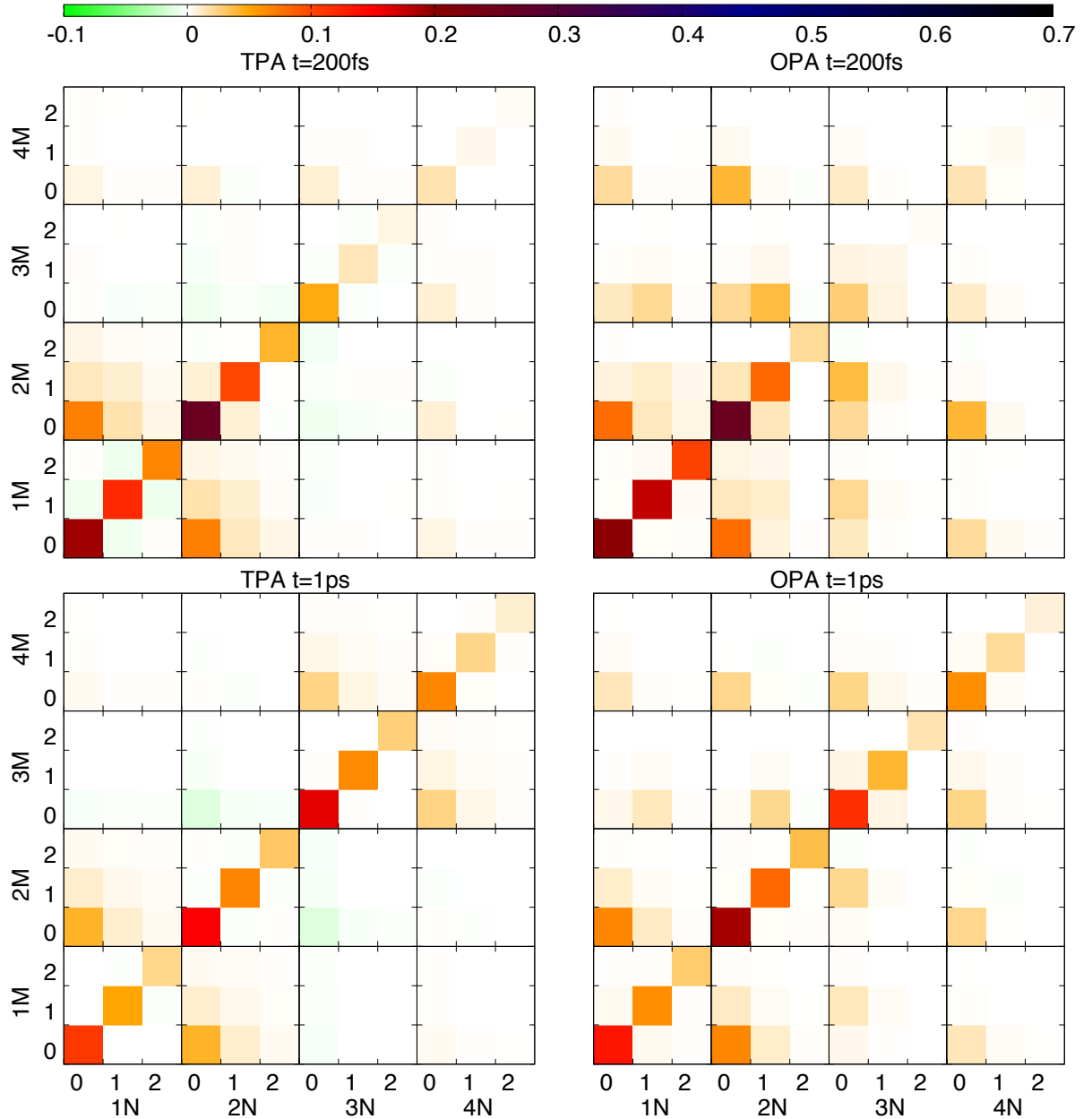


Figure III.9: Vibronic density matrix ( $\text{Re } \rho_{mM_{em}, nN_{en}}$ ) in TPA and OPA at  $t = 200$  and  $1000$  fs and for  $T = 300$  K.

In order to illustrate the difference between TPA and OPA important vibronic density matrix elements are shown for  $t = 200$  fs and  $1$  ps at  $T = 77$  K in Fig. III.8. It is simple to find that TPA and OPA give rather different results. At  $t = 200$  fs this concerns all matrix elements, some of them are not only different in amplitude but also in phase (sign). After  $1$  ps phase and energy relaxation have been effective, causing more similar OPA and TPA results. However, there are still important differences such as the different phase for the off-diagonal elements at site  $m = 3$ .

Fig. III.9 shows the similar situation at  $T = 300$  K. Here, the differences are not so noticeable for sites  $m = 1$  and  $2$ . Instead substantial differences exist in the inter-site coherences between

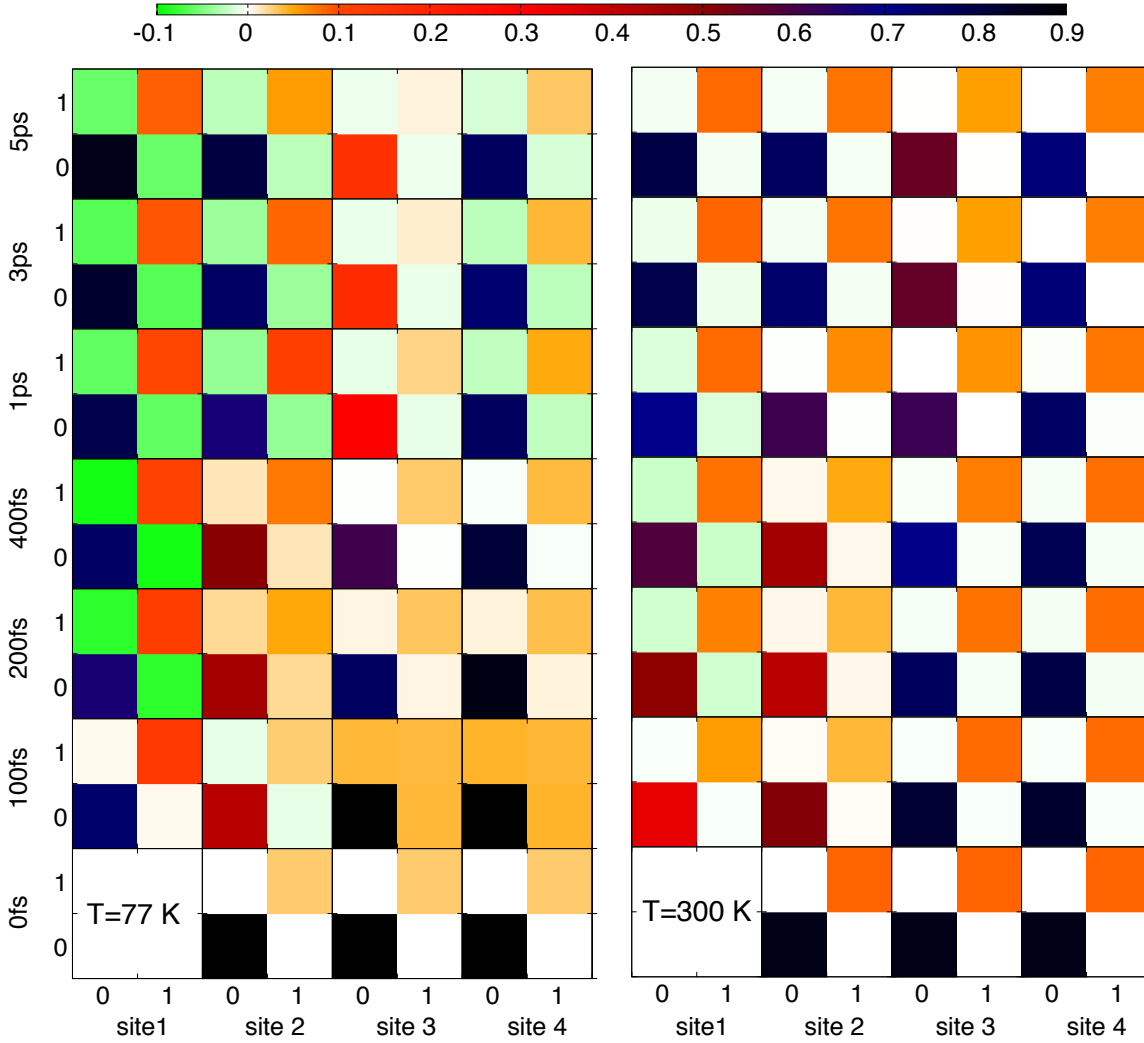


Figure III.10: Real part of the ground state vibrational density matrix, Eq. (III.15) at  $T = 77$  K (left panel) and 300 K (right panel) for different times as indicated. Shown are only the elements with  $M, N = 0, 1$  since others are rather small.

these two sites and sites  $m = 3$  and 4. These are predicted by the OPA to be more important. Evidently, the denser level structure on the TPA results in faster dephasing of the inter-site coherences. The faster relaxation at  $T = 300$  K causes more similar vibronic density matrix elements after 1 ps, though there are still differences, e.g., in the inter-site coherences between site  $m = 1, 2$  and  $m = 3, 4$ .

Compared with the OPA, the TPA allows for vibrational dynamics in the electronic ground states. Vibrational dynamics can be obtained from the RDM by tracing out the vibronic states. With respect to a single site this gives the electronic ground state density matrix

$$R_{M_{g_k}, N_{g_k}}(t) = \sum_{m \neq k} \sum_{M_{e_m}} \rho_{m M_{e_m} M_{g_k}, m M_{e_m} N_{g_k}}(t) \quad (\text{III.15})$$

Fig. III.10 shows the real part of this quantity for different propagation times and at  $T = 77$  K



(left panel) and 300 K (right panel). Because of the initial conditions, i.e. a vertical excitation at site  $m = 1$ ,  $R_{M_{g_1}, N_{g_1}}(0) = 0$ , whereas the population at all other sites is in the Boltzmann distribution. Subsequently, some coherent vibrational wave packet dynamics exist at  $T = 77$  K. Initially, this mostly is related with sites  $m = 1$  and 2. At the other sites triggered by the initial conditions, off-diagonal elements rapidly decay except at site  $m = 4$ . The vibrational relaxation time at 77 K is 246 fs (for an  $1 \rightarrow 0$  transition in site basis). However, vibrational coherences are regenerated continuously by the exciton transfer until the equilibrium is reached. The density matrix  $R_{M_{g_k}, N_{g_k}}$  at 5 ps mostly reflects the equilibrated state. Off-diagonal elements represent contributions from the site basis to the exciton-vibrational eigenstates. The vibrational relaxation time decreases to 147 fs at  $T = 300$  K. Therefore, the ground state density matrix  $R_{M_{g_k}, N_{g_k}}$  is essentially diagonal for all times except at site  $m = 1$ , where there are off-diagonal elements during the first 1 ps.

### DISCUSSION OF EXCITON TRANSFER

In order to discuss the excitonic site populations in the presence of explicit vibrational DOFs the site population at site  $m$  is considered to be obtained from the equations of motion in the absence of dissipation. In second order of the Coulomb coupling from Eq. (II.34) one obtains [64]

$$\begin{aligned} \frac{\partial}{\partial t} P_m &= -2\text{Re} \sum_n \sum_{M_{e_m}, M_{g_n}} \sum_{N_{e_n}, N_{g_m}} |J_{mn}|^2 |\langle M_{e_m} | N_{g_m} \rangle|^2 |\langle M_{g_n} | N_{e_n} \rangle|^2 \\ &\times \int_0^t d\tau e^{i[\omega_{mn} - \Omega^{(H)}(N_{g_m} - M_{e_m} + N_{e_n} - M_{g_n})]\tau} \\ &\times [P_{m, M_{e_m} M_{g_n}}(t - \tau) - P_{n, N_{g_m} N_{e_n}}(t - \tau)] \end{aligned} \quad (\text{III.16})$$

where  $\omega_{mn} = (E_m - E_n)$  is the bare excitonic transition frequency. Furthermore, the population of a certain exciton-vibrational state  $P_{m, M_{e_m} M_{g_n}}$  is introduced, which is the diagonal element of the respective density matrix. Thus the efficiency of transfer between sites  $m$  and  $n$  is decided by a sum over many vibrational channels, where the individual contribution is given by the FC mediated Coulomb coupling, the resonance condition  $\omega_{mn} - \Omega^{(H)}(N_{g_m} - M_{e_m} + N_{e_n} - M_{g_n}) \approx 0$ , and a population difference.

Due to the smallness of the Huang-Rhys factor of  $S^{(H)} = 0.027$  one would not expect an involvement of any vibrational or vibronic excitation. Here, the resonance condition plays its role in facilitating vibrationally assisted transfer. For the present model the relevant excitonic energy gaps represent  $\omega_{21} = 0.44\Omega^{(H)}$ ,  $\omega_{31} = 1.72\Omega^{(H)}$ , and  $\omega_{32} = 1.28\Omega^{(H)}$ . It is interesting that in terms of transfer between the local sites this is not at all optimal. In addition, the energy gap between sites  $m = 4$  and  $n = 3$  is  $\omega_{43} = \Omega^{(H)}$ , but the pathway via site  $m = 4$  is only of minor importance according to weak Coulomb couplings.

In accordance with this discussion let us return to the results shown in Figs. III.5-III.10. Comparing Fig. III.5 with III.7 it is noticed that at  $T = 77$  K since the FC excited vibronic states are partly off-resonant the initial depopulation for site  $m = 1$  is slowed down. Thus, vibronic relaxation is necessary for improving the resonance conditions. In the initial plan the channel involving two vibronic excitations is also active. However at later times there are only channels with one vibronic excitation in the transfer (Fig. III.8). From Fig. III.10 one could

observe the participation of ground state vibrations up to  $N = 1$ . This will reduce energy gaps if the vibronic excitation is too high. At  $T = 300$  K the phase and energy relaxation is more obvious and many channels are suppressed. This decelerates the depopulation of site  $m = 1$  considerably. Effectively no net acceleration of trapping at the sink is found if compared with the bare excitonic case (model I).

In case of the OPA, the summations in Eq. (III.16) are limited to  $M_{g_n} = 0$  and  $N_{g_m} = 0$ . Hence, no vibrational excitation can cause additional transfer channels via establishing resonance conditions, e.g. for higher excited vibronic levels. As a result OPA yields a slower depopulation of the initial site and thus a slower population of the sink site comparing with TPA (Fig. III.5).

## 2 LH2 OF *Alc. vinosum*: B800 BAND SPLITTING

There are different explanations for the B800 absorption band splitting shown in Fig. III.16. The two B800 sub-bands will be labelled as B800b (blue side) and B800r (red side). One indicates that the splitting may be due to the sample which contains a mixture of two spectrally different LH2 complexes which can't be separated [98]. The second hypothesis assumes that the two B800-type BChl *a* molecules in the individual LH2 complex have alternating distances, thus leading to excitonic dimerization. It is supported by polarization-resolved single-molecule spectroscopy [16]. However, in earlier transient absorption experiments the excitonic coupling and the simultaneous bleaching of the B800 bands upon selective excitation of one sub-band was not observed [99]. A third hypothesis is that due to the weakly and strongly hydrogen-bonded BChl chromophores for the two B800 sub-bands, proton dynamics will cause conformational changes under illumination, which is supported by hole-burning experiments [100]. In addition, some experiments supported the energetic heterogeneity of the B800 molecules. It plays a significant role during the B800 to B850 transfer leading to different transfer rates and the peak splitting [101, 102].

In Ref. [102], Schröter and coworkers presented unambiguous evidence for the excitonic interaction shaping the B800 band through crosspeaks appearing in 2DES. By using a global kinetic fitting procedure, they obtained the depopulation time for LH2 sub-bands in Fig. III.11. Note that depopulation times of 1800 fs for B800b $\rightarrow$ B850 and 2800 fs for B800b $\rightarrow$ B800r had been obtained in Ref. [99]. In the present work, an excitonic model is used to understand the possible origin of these time scales and their relation to the absorption spectrum.

### 2.1 MODEL SYSTEM

In principle, the crystal structure of LH2 can be obtained using X-ray crystallography combined with electron microscopy and there are different structures purified from different membranes. However the actual structure strongly depends on the preparation conditions [102]. In Ref. [102] the split B800 band exists in the absorption spectrum (black dotted line in Fig. III.16), which means the structure for LH2 in the experiment is probably close to the assumption of the paper of Löhner and his coworkers [16].

In Ref. [16] the arrangement of the B800 and B850 rings was developed from *Rps. molischianum* to reach the best agreement for their experiment for LH2 of *Alc. vinosum*. The subunits

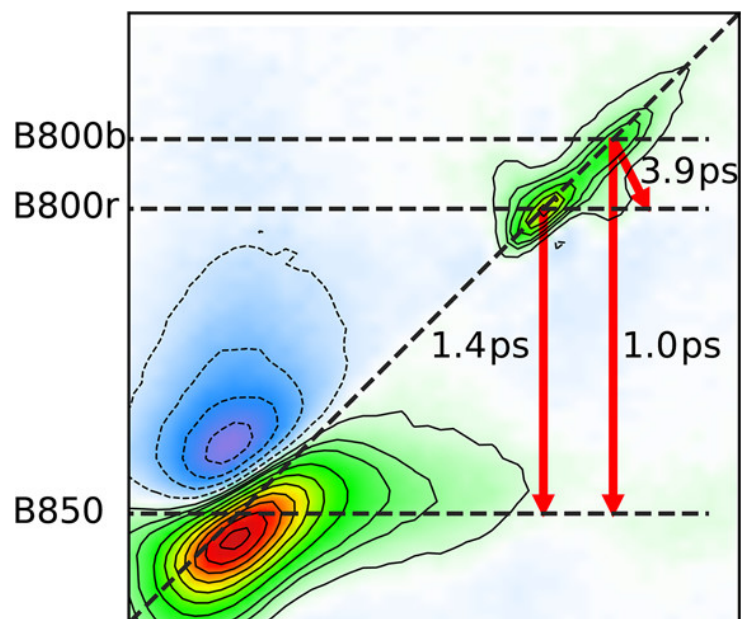


Figure III.11: Experimental scheme of energy transfer shown together with the 2DES. The main exciton (sub-) bands are in dashed horizontal lines and the energy transfer pathways are shown by the red arrows with the depopulation time. Reprinted with permission from M. Schröter, M. J. P. Alcocer, R. J. Cogdell, O. Kühn, and D. Zigmantas, Origin of the two bands in the B800 ring and their involvement in the energy transfer network of *allochromatium vinosum*, *J. Phys. Chem. Lett.* 9, 1340–1345 (2018). Copyright 2018 by the American Chemical Society.

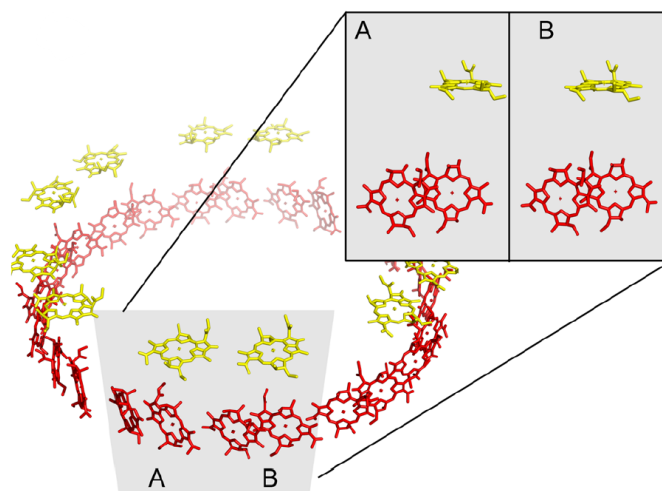


Figure III.12: Scheme of the BChl *a* molecular arrangement with B850 (red) and B800 (yellow) as proposed by Löhner et al. [16]. The inset shows the basic subunit for *A* and *B* on an expanded scale. Reprinted with permission from Springer: A. Löhner, A.-M. Carey, K. Hacking, N. Picken, S. Kelly, R. Cogdell, and J. Köhler, The origin of the split B800 absorption peak in the LH2 complexes from *allochromatium vinosum*, *Photosynth. Res.* 123, 23 (2015). Copyright 2015 by Springer Science Business Media Dordrecht. All Rights Reserved.

of BChl  $a$  molecules are arranged as shown in the Fig. III.12. One can find that there are two kinds of B800s in  $A$  and  $B$  subunits.  $A$ -kind B800 molecules are located vertically almost on top of one B850 molecule. A  $B$ -kind B800 is located vertically approximately on top of the center in between two B850 molecules. In the total structure B800/B850 molecules are all positioned on rings with radius  $38.5\text{\AA}$ . The center to center distance between B800 and B850 rings is  $17\text{\AA}$ . Three angles for the molecular dipole moment  $\vec{\mu}$  are fitted to match the absorption as shown in Fig. III.13:  $\alpha_m$  is the angle between the projection for dipole moment  $\vec{\mu}_m$  and local tangent  $\vec{n}_m$  of  $m$  molecule in ring-plane.  $\beta_m$  is the angle between the dipole moment  $\vec{\mu}_m$  and the cylinder axis  $\vec{z}$ . And  $\gamma$  is the rotation (torsion) angle between B800 and B850 rings.

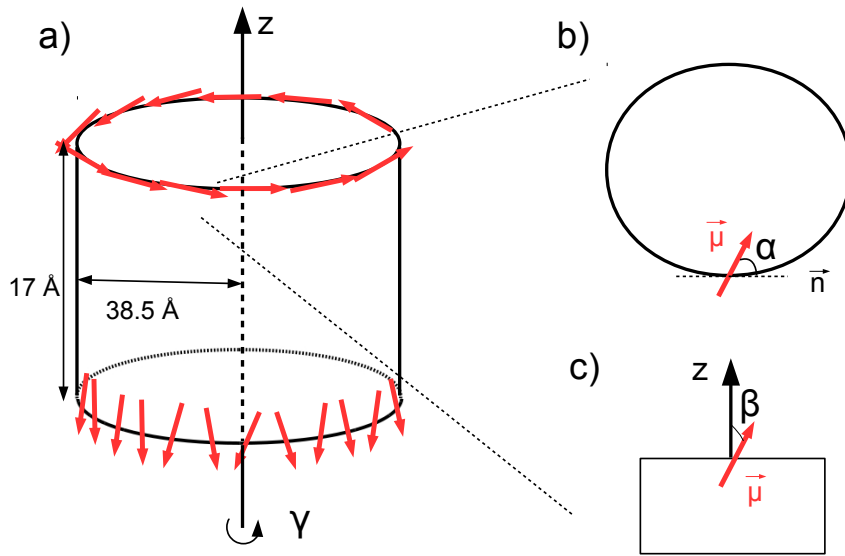


Figure III.13: Scheme of the set of angles for BChl  $a$  molecules (B850 or B800) in the LH2 rings. a) the direction of dipole moments for the B800 (top) and B850 (bottom) and torsion angle  $\gamma$ . b) the definition for angle  $\alpha$  between the tangent  $\vec{n}$  of the ring and projection of dipole moment  $\vec{\mu}$  in the ring plane. c) the angle  $\beta$  between  $\vec{\mu}$  and axis  $\vec{z}$ .

The fitting of the set of angles by Löhner et al. [16] has been performed using the fluorescence excitation spectrum for the complex embedded into a polymer matrix at 1.2 K. The authors also report a spectrum for LH2 in a buffer/glycerol matrix. Here the B800 double peak is more pronounced and in fact looks closer to the one reported in Ref. [102], also measured in glycerol, but at 77 K. Therefore, the parameters of Ref. [16] can't be used and a new parameterization according to the absorption spectrum of Ref. [102] is performed. Since a fit to the absorption alone is not necessarily unique, density matrix simulations of the population dynamics are performed and compared with the relaxation time scales reported in Ref. [102].

The LH2 complex will be treated using the system-bath model I from Eq. (III.4), which is studied as in Ref. [19]. For the spectral density an experimental result is used (see Fig. III.14), which was obtained from Ref. [103]. In the following, the single-exciton eigenstates without

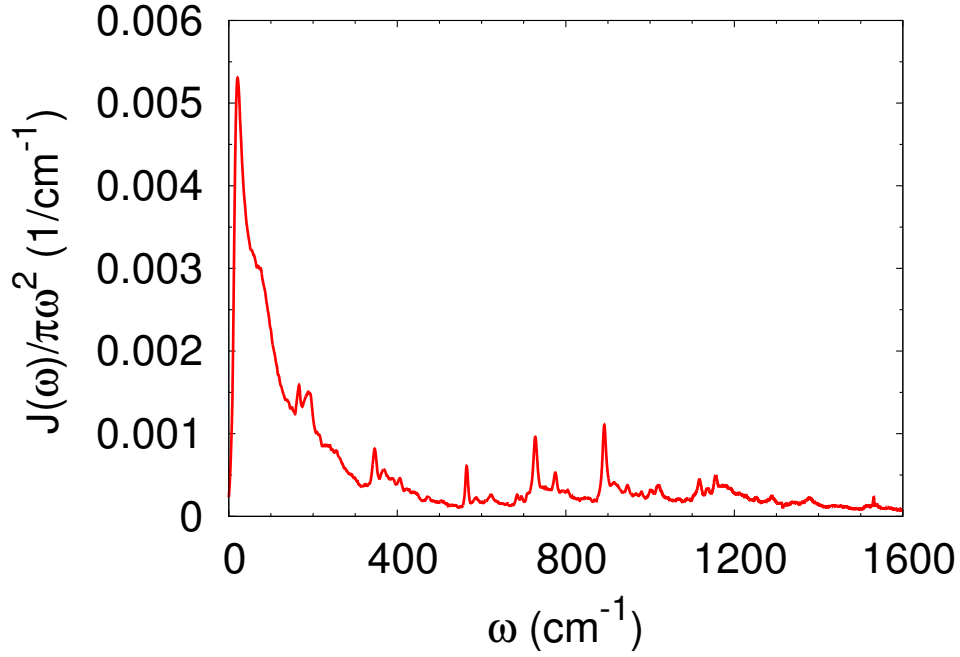


Figure III.14: The BChl *a* spectral density obtained from fluorescence line narrowing in Ref. [103].

vibrational states will be used. They are expressed as

$$|\alpha\rangle = \sum_m c_{m,\alpha} |m\rangle \quad (\text{III.17})$$

The respective transition dipole matrix elements are given by

$$\vec{\mu}_\alpha = \sum_m \vec{\mu}_{m,g} c_{m,\alpha} \quad (\text{III.18})$$

Restricting the model to population relaxation and coherence dephasing (Bloch model) only, the single-exciton terms for the relaxation matrix defined from Eq. (II.70) are given by

$$R_{\alpha\alpha,\beta\beta} = -k_{\beta\rightarrow\alpha} + \delta_{\alpha\beta} \sum_\gamma k_{\alpha\rightarrow\gamma} \quad (\text{III.19a})$$

$$R_{\alpha\beta,\alpha\beta} = \hat{\Gamma}_{\alpha\beta} + \frac{1}{2} \sum_{\gamma \neq \alpha} k_{\alpha\rightarrow\gamma} + \frac{1}{2} \sum_{\gamma \neq \beta} k_{\beta\rightarrow\gamma} \quad (\text{III.19b})$$

where  $k_{\alpha\rightarrow\beta}$  is the transition rate from Eq. (II.72). In the eigenstate basis the rates can be simplified as

$$k_{\alpha\rightarrow\beta} = \sum_m C_m(\omega_{\alpha\beta}) |c_{m,\alpha}|^2 |c_{m,\beta}|^2 \quad (\text{III.20})$$

The same shape of the spectral density is assumed for all sites (cf. Fig. III.14). Specificity is introduced via the coupling coefficient  $a_m$  between the bath and molecule  $m$ , such that the

correlation function  $C_m(\omega)$  from Eq. (II.63) becomes

$$C_m(\omega) = a_m C(\omega) \quad (\text{III.21})$$

In addition, the pure dephasing rate  $\hat{\Gamma}_{\alpha\beta}$ , as  $\Gamma_{aa,bb}(0)$  from Eq. (II.67), in eigenstate basis becomes

$$\hat{\Gamma}_{\alpha\beta} = \sum_m \hat{\Gamma}_m(T) (|c_{m,\alpha}|^2 - |c_{m,\beta}|^2)^2 \quad (\text{III.22a})$$

$$\hat{\Gamma}_{\alpha 0} = \sum_m \hat{\Gamma}_m(T) |c_{m,\alpha}|^4 \quad (\text{III.22b})$$

where  $\hat{\Gamma}_m(T)$  is pure dephasing rate for molecule  $m$  at temperature  $T$ . Thus the phase relaxation rates for the excitonic transitions from Eq. (II.73) read

$$\gamma_\alpha = \sum_{\beta \neq \alpha} k_{\alpha \rightarrow \beta} + 2\hat{\Gamma}_{\alpha 0} \quad (\text{III.23})$$

Inhomogeneous broadening is accounted for using the model of diagonal static disorder, which assumes an independent Gaussian distribution of site energies with variance  $\sigma_{\text{dis}}$ . The results presented below have been obtained by averaging over 5000 realizations. Thus the linear absorption spectrum of LH2 is obtained from

$$A(\omega) = \left\langle \sum_\alpha \frac{\gamma_\alpha |\vec{\mu}_\alpha|^2}{(\omega - \omega_\alpha)^2 + \gamma_\alpha^2/4} \right\rangle_{\text{disorder}} \quad (\text{III.24})$$

The equation of motion for the RDM with the external field  $\vec{E}_{\text{ext}}(t)$  is given by

$$\frac{d}{dt} \rho(t) = -i [H_S + H_{\text{field}}(t), \rho(t)] - R\rho(t) \quad (\text{III.25})$$

Thus based on the interaction with the external field  $H_{\text{field}}(t)$  according to Eq. (II.26) and the dissipative matrix  $R$  from Eq. (II.71), the equations of motion in the eigenstate basis reads

$$\begin{aligned} \frac{d}{dt} \rho_{\alpha\beta}(t) = & -i\omega_{\alpha\beta} \rho_{\alpha\beta}(t) - (1 - \delta_{\alpha\beta}) R_{\alpha\beta, \alpha\beta} \rho_{\alpha\beta}(t) - \delta_{\alpha\beta} \sum_{\alpha'} R_{\alpha\alpha, \alpha'\alpha'} \rho_{\alpha'\alpha'}(t) \\ & + i\vec{E}_{\text{ext}}(t) [\vec{\mu}_\alpha \rho_{0\beta}(t) - \vec{\mu}_\beta \rho_{\alpha 0}(t)] \end{aligned} \quad (\text{III.26a})$$

$$\frac{d}{dt} \rho_{\alpha 0}(t) = - (i\omega_{\alpha 0} + \gamma_\alpha) \rho_{\alpha 0}(t) + i\vec{E}_{\text{ext}}(t) [\vec{\mu}_\alpha \rho_{00}(t) - \sum_\beta \vec{\mu}_\beta \rho_{\alpha\beta}(t)] \quad (\text{III.26b})$$

$$\rho_{00}(t) = 1 - \sum_\alpha \rho_{\alpha\alpha}(t) \quad (\text{III.26c})$$

## 2.2 RESULTS

### ABSORPTION SPECTRA

The interaction in the B800 and B850 molecules are all simply obtained in the dipole-dipole approximation Eq. (II.25) using the geometry of Ref [16] (cf. Fig. III.12) with dipole moment

directions according to Fig. III.13. The various parameters for the models are summarized in Table III.1. The common parameters for all the models taken from Ref. [16] are as follows: all the site energies for B850 and B800 BChls  $a$  are set to  $E = 12900 \text{ cm}^{-1}$ . The angles for the dipole moment  $\vec{\mu}$  are  $\alpha_{800} = 0^\circ$  and  $\beta_{800} = 90^\circ$  for B800 BChls  $a$ ,  $\alpha_{850} = 10^\circ/170^\circ$  and  $\beta_{850} = 110^\circ/70^\circ$  for B850 BChls  $a$  (cf. two directions for B850 in Fig. III.13a), and  $\gamma = 10^\circ$ . Instead of changing the geometry, several parameters related to the energetics and the system-bath coupling are introduced for fitting the absorption spectrum at 77 K (see Table III.1). Here Ref. [16] corresponds to **Model 1** as far as the exciton Hamiltonian is concerned.  $E_s$  is the energy difference between the  $A$ - and  $B$ -kind B800 subunits,  $a_i$  ( $i = 800/850$  for B800/B850) is the coupling coefficient with the bath from Eq. (III.21) and  $\hat{\Gamma}_i$  is the pure dephasing  $\hat{\Gamma}_{i0}$  defined in Eq. (III.22), assuming  $a_i$  and  $\hat{\Gamma}_i$  are the same for all B800 or B850 BChls  $a$  in the complex. Finally, except for **Model 1** the magnitude of the monomeric transition dipole moment has been chosen as  $|\mu_{m,eg}| = 8.25 \text{ D}$ . In addition the B800-B850 coupling has been scaled by a factor of two in **Model 4**.

Table III.1: Parameters of the different models used in this work.

	<b>Model 1</b>	<b>Model 2</b>	<b>Model 3</b>	<b>Model 4</b>
B800 dipole moment (D)	8.25	8.25	8.25	8.25
Maximal B800-B800 interaction ( $\text{cm}^{-1}$ )	186	186	186	186
Pure dephasing rate $\hat{\Gamma}_{800}$ ( $\text{cm}^{-1}$ )	0	0	300	300
Coupling coefficient $a_{800}$	0.15	0.15	0.098	0.01
Energy shift $E_s$ for B800 ( $\text{cm}^{-1}$ )	0	-250	-250	-250
B850 dipole moment (D)	7.5	8.25	8.25	8.25
Maximal B850-B850 interaction ( $\text{cm}^{-1}$ )	629	761	761	761
Pure dephasing rate $\hat{\Gamma}_{850}$ ( $\text{cm}^{-1}$ )	0	0	1750	1750
Coupling coefficient $a_{850}$	0.15	0.15	0.098	0.01
Maximal B850-B800 interaction ( $\text{cm}^{-1}$ )	60	66	66	132

First, the different models are analysed in terms of their eigenvalue/eigenvectors for the case of no disorder. Fig. III.15 shows the eigenvalues, the coefficient  $c_\alpha = \sum_{m \in i} |c_{m,\alpha}|^2$  and oscillator strength for **Models 1-4**. Inspecting the mixture of the eigenstates one notices that there is a clear separation between B850-like and B800-like states. The former cluster at upper and lower band edges, while the latter are located in the band center. Due to the high symmetry, oscillator strength is distributed over a few transitions only. As far as the B800-like states are concerned one notices that going from the original **Model 1** to **Models 2,4** the ratio of oscillator strengths around 800nm is (approximately) reversed.

Using a Gaussian distribution of site energy with variance  $\sigma_{\text{dis}} = 150 \text{ cm}^{-1}$ , the averaged absorption spectra of 5000 simulated samples can be calculated by Eq. (III.24) for all models. Results are shown in Fig. III.16 together with absorption spectra from Ref. [102]. **Model 1** is using the original data from Ref. [16], whose spectrum is shown in Fig. III.16 a. (Note that in Ref. [16] a much simpler model for the linewidth has been assumed.) There is an obvious B800 band splitting, however, the spectrum doesn't agree with the experiment of Ref. [102] (see comment on sample preparation above). In contrast to Ref. [16] the intensity ratio of the peaks of B800 bands is different, and the splitting between the B800 peaks and the B850 peak is also

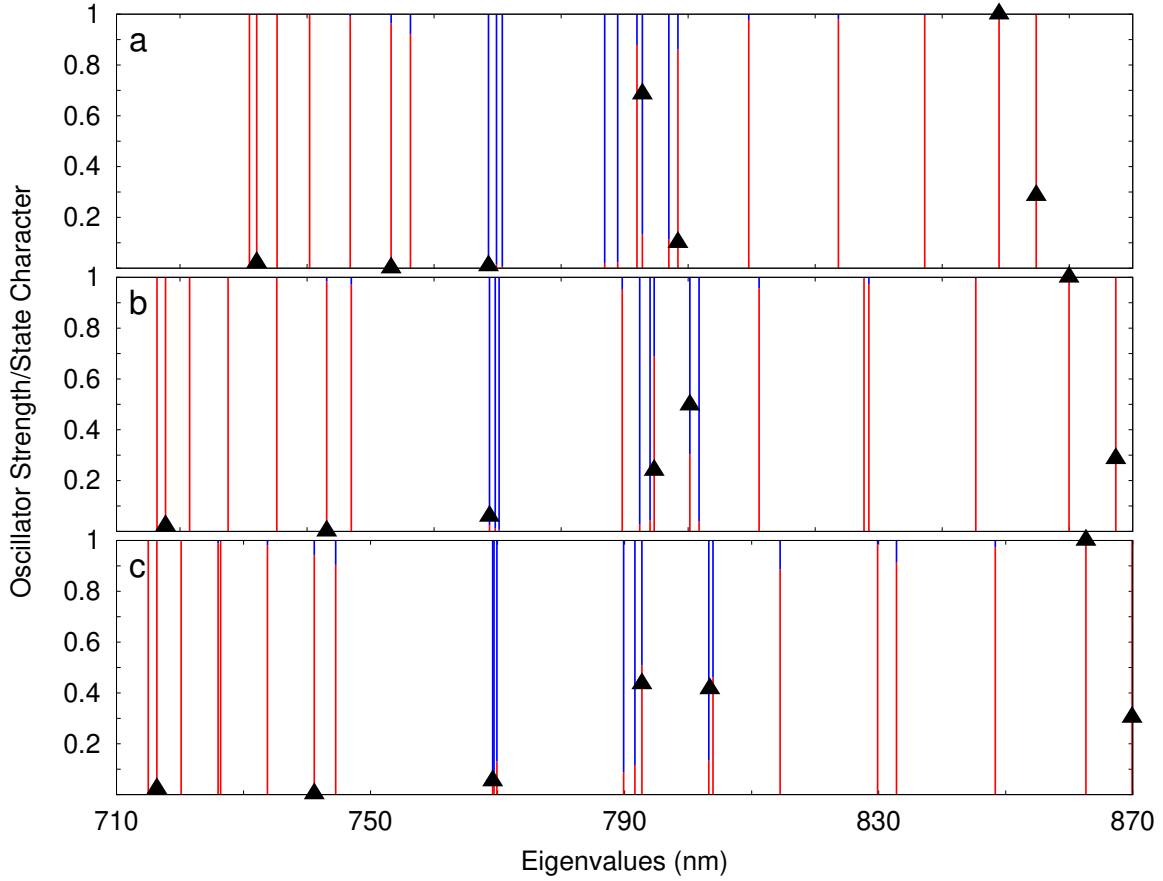


Figure III.15: Eigenvalues, state character as measured by the coefficient  $c_\alpha = \sum_{m \in i} |c_{m,\alpha}|^2$  (red line for  $i = \text{B850}$  and blue line for  $i = \text{B800}$  and oscillator strength (black triangles) for **Model 1** (a), **Model 2,3** (b) and **Model 4** (c).

different.

To improve the agreement, first it was found that the dipole moment for B850 BChls  $a$  must be increased from 7.5 D to 8.25 D (the same as B800) to match the B800-B850 splitting. Further once an energy shift  $E_s = -250 \text{ cm}^{-1}$  is introduced the ratio of the B800 peak heights is reversed, which is shown for **Model 2** in Fig. III.16 b. (In fact, introducing an energy shift between B800 and B850 subunits can match the splitting between B800 and B850, however, the ratio of the B800 peaks can't be matched due to the interdependence between the ratio and that energy shift.) However in **Model 2** compared with the experiment of Ref. [102], the peak for B800 is too high, and an extra peak appears near 765 nm. From Fig. III.15, it is found that the eigenvalues for the extra peak are mainly from B800 subunits.

Second, when the coupling coefficients  $a_i$  are in the magnitude of 0.01, the time scales for the population flow are close to the result in Fig. III.11. Of course, if the coupling with bath becomes so small (more than 10 times smaller than the original coefficient in **Model 1**), the spectra are very narrow. Thus, the pure dephasing rates  $\hat{\Gamma}_{800} = 300 \text{ cm}^{-1}$  and  $\hat{\Gamma}_{850} = 1750 \text{ cm}^{-1}$  are used to broaden the peaks to match the experiment data, which is shown for **Model 3** in Fig. III.16 c. Based on the Eqs. (III.19) and (III.26), the pure dephasing rates  $\hat{\Gamma}_{\alpha 0}$  don't affect the population flow. But there is no obvious splitting in the B800 bands for **Model 3**.



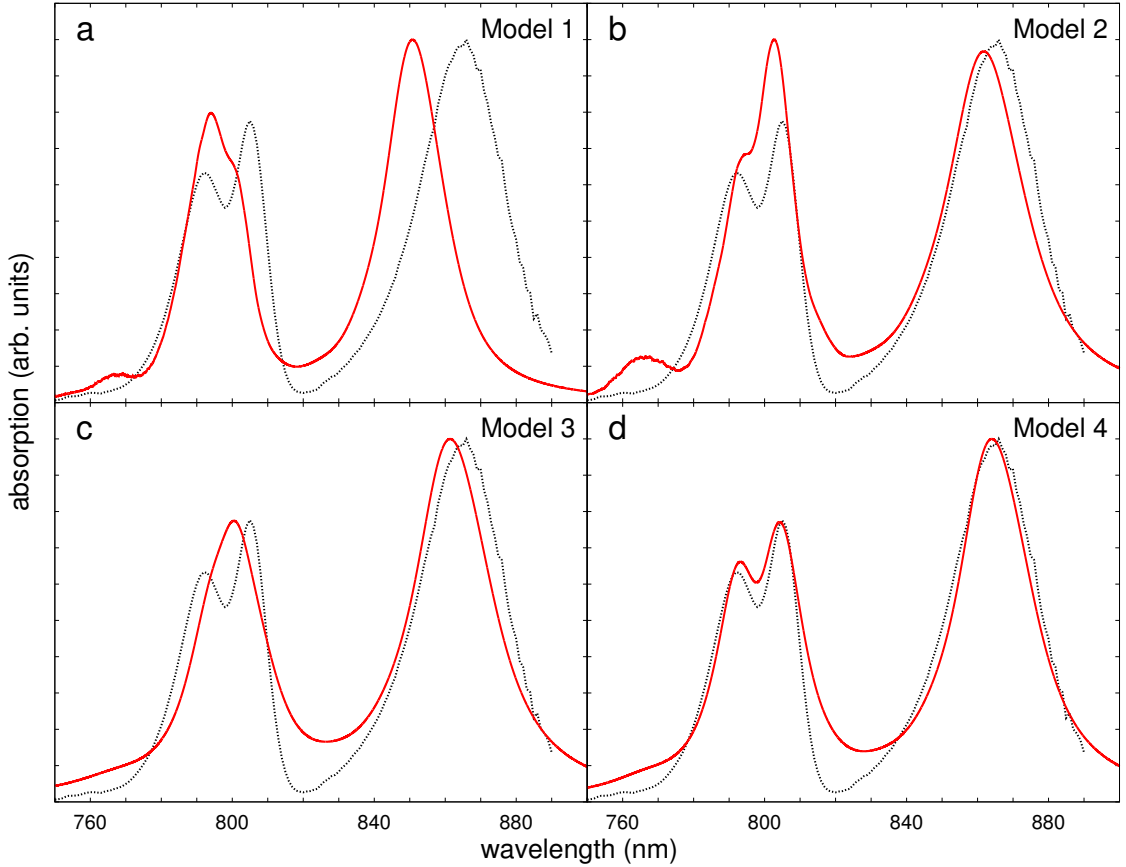


Figure III.16: Absorption spectra (full line) averaged from 5000 samples for 4 different models are compared with the experimental spectra (black dashed line) from Ref. [102]. Model parameters are given in Table III.1.

In principle, two coefficients can directly lead to excitonic dimerization, which are the energy shift  $E_s$  and the intramolecular coupling  $J_{800-850}$  between B800 and B850 BChls  $a$ . But the former is used to match the other requirements. It is found when the coupling  $J_{800-850}$  becomes two times larger with the maximum reaching  $132 \text{ cm}^{-1}$ , it gives the best agreement with the experimental absorption spectrum, which is shown for **Model 4** in Fig. III.16 d.

Fig. III.17 shows the phase relaxation rates  $\langle \gamma_\alpha \rangle$  and wavelengths  $\langle E_\alpha/hc \rangle$  for **Model 4** after averaging over an inhomogeneous ensemble (5000 realizations). From the data, one can find that although  $\hat{\Gamma}_i$  is large, the  $\gamma_\alpha$  is still in a reasonable range compared with data from Ref. [104].

## POPULATION DYNAMICS

In order to investigate the time scales of population flow in **Model 4**, an external field with a Gaussian pulse shape

$$\vec{E}_{\text{ext}} = \vec{E}_0 \cos(\omega t) \exp\left(-\frac{(t-t_0)^2}{2\sigma^2}\right) \quad (\text{III.27})$$

is introduced. Here  $\vec{E}_0 = 1.1 \times 10^7 \text{ V/m}$ ,  $t_0 = 200 \text{ fs}$  and  $\sigma = 42.5 \text{ fs}$  (i.e. the FWHM of the pulse is  $100 \text{ fs}$ .) have been used for illustration.

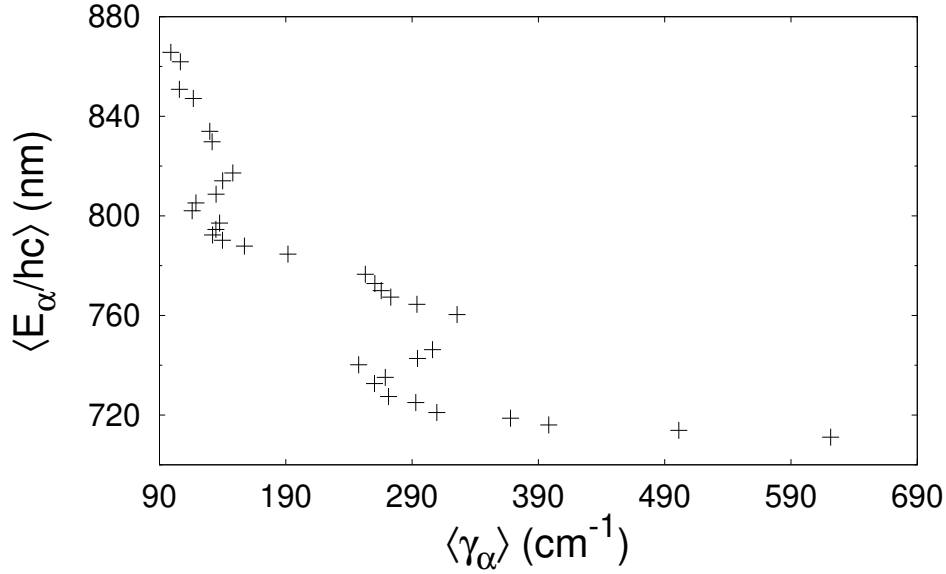


Figure III.17: The phase relaxation rates  $\langle \gamma_\alpha \rangle$  and wavelength  $\langle E_\alpha/hc \rangle$  after averaging over an inhomogeneous ensemble (5000 realizations) for **Model 4**.

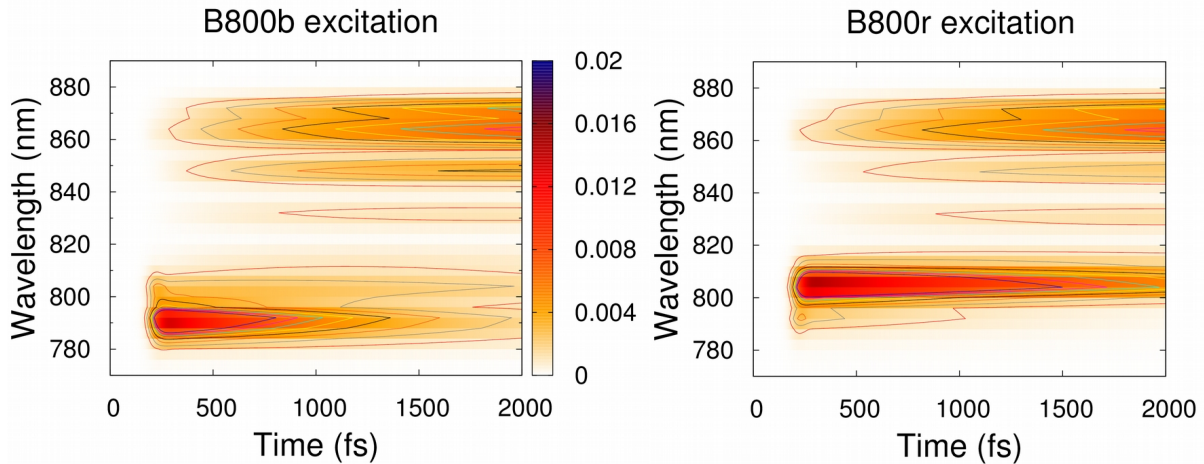


Figure III.18: The populations dynamics of **Model 4** from 760 nm to 900 nm (step 4 nm) for excitation at the two B800 band maximal.(contour value from 0.001 to 0.01 by 0.001).

Based on the Eq. (III.19), the Redfield tensor elements are calculated from the parameters in Table III.1 for **Model 4**. Then the population flow in LH2 can be obtained by solving Eq. (III.26) for the 5000 samples representing the Gaussian disorder. To account for the averaging over samples, population dynamics will be assigned to certain wavelength ranges as  $P_{ab} = \sum_\alpha \rho_{\alpha\alpha}$  if  $E_\alpha \in [\lambda_a, \lambda_b]$ . To focus on the time scales for the peaks of B800 BChls  $a$ , two excitation cases are introduced as follows: the case B800b/B800r excitation corresponds to excitation within the wavelength range [788,800] nm/[800,812] nm. In other words B800b and B800r matches the lower and higher wavelength peak, respectively. In both cases the direction and frequency of the external field are assumed to be the same as the direction and eigenvalue for the largest dipole moment  $\vec{\mu}_\alpha$  in the considered frequency range. The population dynamics for the two cases

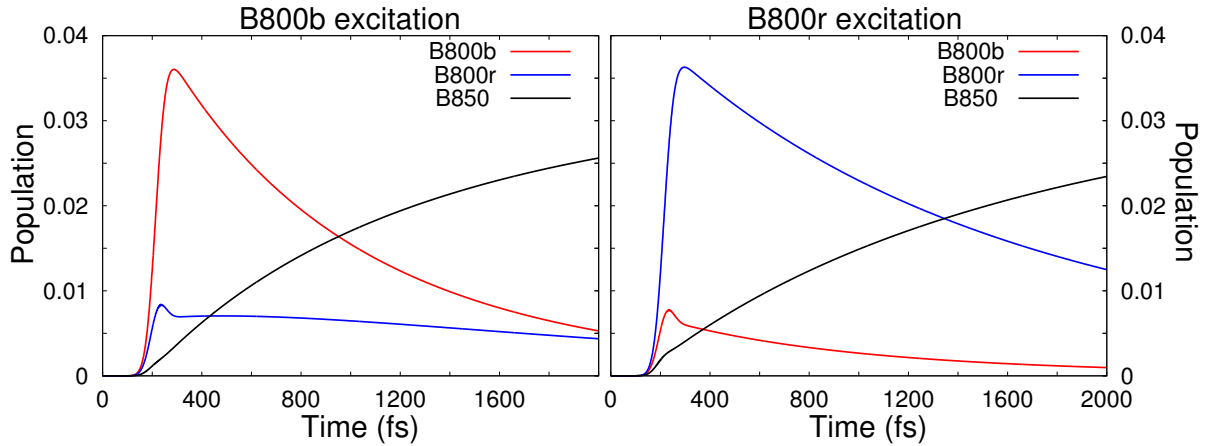


Figure III.19: The population for the three peaks in the LH2 absorption spectra, B800b:[788,800] nm, B800r:[800,812] nm and B850:[852,876] nm and the two excitation conditions of Fig. III.18.

during 2000 fs is shown in Fig. III.18. First, let's consider excitation of the lower wavelength band (B800b), cf. left panel of Fig. III.18. Here the states in B800b are dominantly excited and in B800r are weakly excited by the external pulse. After the pulse, the excitation energy transfers from B800b to B850 quickly. However, it's found that there is no obvious reduction of the populations in B800r range from 400 fs to 800 fs but after 1200 fs depopulation sets in, which is more clearly observed from the left panel of Fig. III.19. The reason is that shortly after the pulse the direct relaxation from B800b to B800r keeps the populations in B800r range approximately unchanged, but after some time there is not enough population flow to the B800r range to compensate the transition from B800r to B850. Second, we focus on the case where the higher wavelength band is excited (B800r), cf. right panels of Fig. III.18 and Fig. III.19. Here the states in B800b are weakly excited and in B800r are strongly excited by the external pulse. Using Fig. III.19, one can find that there is a difference for depopulation times for B800b and B800r excitation.

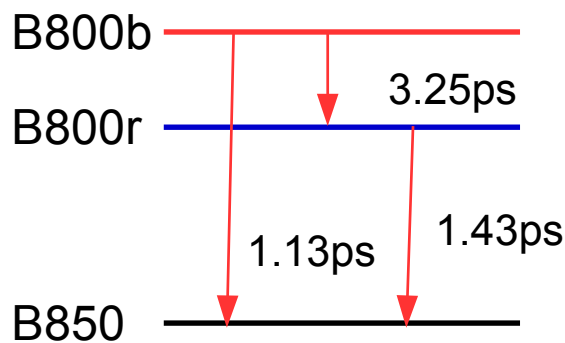


Figure III.20: The relaxation time for **Model 4** assuming an effective 3-level scheme.

In principle, the time scales for the population dynamics of the LH2 model can be simply obtained from the range population of B800b/r excitation in Fig. III.19. By fitting the population

of B800b in the left figure and B800r in the right figure, one can get the total depopulation time for B800b which is 840 fs and a depopulation time from B800r to B850 of 1430 fs. The depopulation time from B800b to B800r is 3250 fs by fitting the population of B800r in the left figure and from B800b to B850 is 1130 fs. In total, the depopulation time for **Model 4** is shown in Fig. III.20 which compares well with the results by a global kinetic fitting of the 2DES data in Fig. III.11.

Furthermore, the time scales for the population flow are calculated and compared with the experimental result. It is found that the energy transfer from B800b to B850 band is via two pathways: direct transfer to B850, which is the main pathway, and indirect transfer via B800r to B850. The obtained time scales are in accord with Ref. [102].

---

## Chapter IV

# Polarization Effects and Exciton Dynamics in Hybrid Systems

Due to the growing research in plasmonics, there is an interest to study the change of optical properties of single molecule or EET among molecules which are strongly modified by the nearby NSs. Field enhancement provides a means to manipulate photophysical and photochemical molecular dynamics, even in the weak field regime (see, e.g., [105, 106]). In fact, the nanostructure brought into close proximity with a molecule will not only enhance the field of an incident external laser pulse, but also react on the presence of the molecule's charge density via an additional polarization field. Vice versa, the electronic structure of the molecule will be modified by the nanostructure. Hence a self-consistent description is mandatory.

In Section IV.1, a DFTB-based exploratory study of the self-consistent interaction of a NS-molecule hybrid system is provided in the static limit. To that end the simplified test case of a metal NS in close proximity of molecules is considered. Whereas the molecular charge density is modelled via DFTB-based atom-centred Mulliken charges (cf. Sec. II.4.1), the response of the NS to the molecular charges is incorporated via a high-order multipole-expansion (cf. Sec. II.3).

Real time TDDFT applied to systems as complex as molecular aggregates is computationally rather demanding. Here, an alternative the considerably more efficient TDDFT [80] is employed to study the optical properties of the molecule near NSs in presence of a laser field. To reduce the computation, the external field in the molecule is assumed being uniform.

The time-dependent evolution of molecules in external laser was discussed in the Section II.4.2. Considering that the enhancement effect of a NS is very short-ranged, the molecule nearest to NS would be affected strongly by the enhancement of NS. Thus the simulation of the molecule nearest to NS is discussed in Section IV.2.

### 1 STATIC CASE

#### 1.1 MODEL SYSTEMS

Two model systems are studied in this approach: First, the neutral tetracene ( $C_{18}H_{12}$ ), abbreviated as TET in Fig. IV.1a, is considered as being a representative of molecular crystal forming

simple aromatic hydrocarbons [107]; Second, a cationic carbocyanine (CCY) dye, the positively charged 5,5',6,6'-Tetraethyloro-1,1',3,3'-Tetraethyl-Benzimidazolyl -Carbocyanine Chloride ( $[\text{C}_{21}\text{H}_{19}\text{Cl}_4\text{N}_4]^+$ ), is chosen. It is a simple derivative of the 5,5',6,6'-tetrachlorobenzimidazolo-carbocyanine (TBC) chromophore, see Fig. IV.1b. TBC derivatives have been widely studied [108, 109] and show, in particular, a rich aggregation behavior depending on the counter ion and pH, solvent and type of derivative [110, 111]. Note that, in order to focus on polarization effects due to a charged species, the counter ion is not considered here. Further the study does not focus on the practical realization of such systems, but on the principal effect of a nearby NS on the molecular charge density.

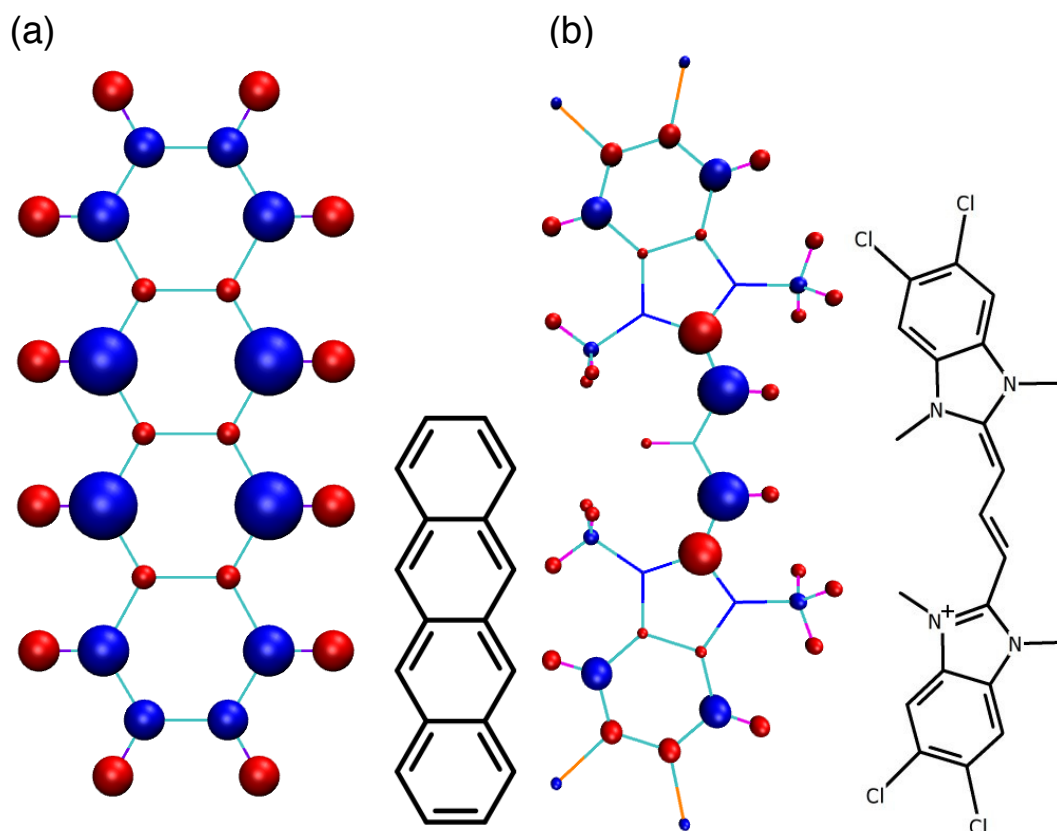


Figure IV.1: Mulliken charges for free TET (a) and CCY (b) together with the respective chemical structures. Blue and red color refer to negative and positive charge, respectively. The radii of the spheres are proportional to the magnitude of the respective charge. The maximum negative charge is  $-0.123 e$  and  $-0.273 e$  for panel (a) and (b), respectively.

The Mulliken charges at the DFTB equilibrium geometry in the electronic ground state are shown in Fig. IV.1. Compared with TET (panel a), the pattern of Mulliken charges in CCY (panel b) is considered to be more structured. A net charge of  $0.65 e$  is carried by each of two benzimidazolo moieties, whereas a net charge of  $-0.3 e$  is in the trimethine bridge. The HOMOs of both molecules reflect the extended  $\pi$  system (shown in Fig. IV.2) for the planar geometries (apart from methyl groups in case of CCY which conform to the  $C_s$  symmetry). TET has no permanent dipole moment, whereas a dipole moment of magnitude  $1.1 \text{ D}$  is oriented along the short axis of CCY. Finally, the dimension of the  $\pi$ -system is about  $11 \times 5 \text{ \AA}$  for TET and about

$17 \times 6 \text{ \AA}$  for CCY; in the following the lengths of the long axes will be represented as  $L_{\text{mol}}$ .

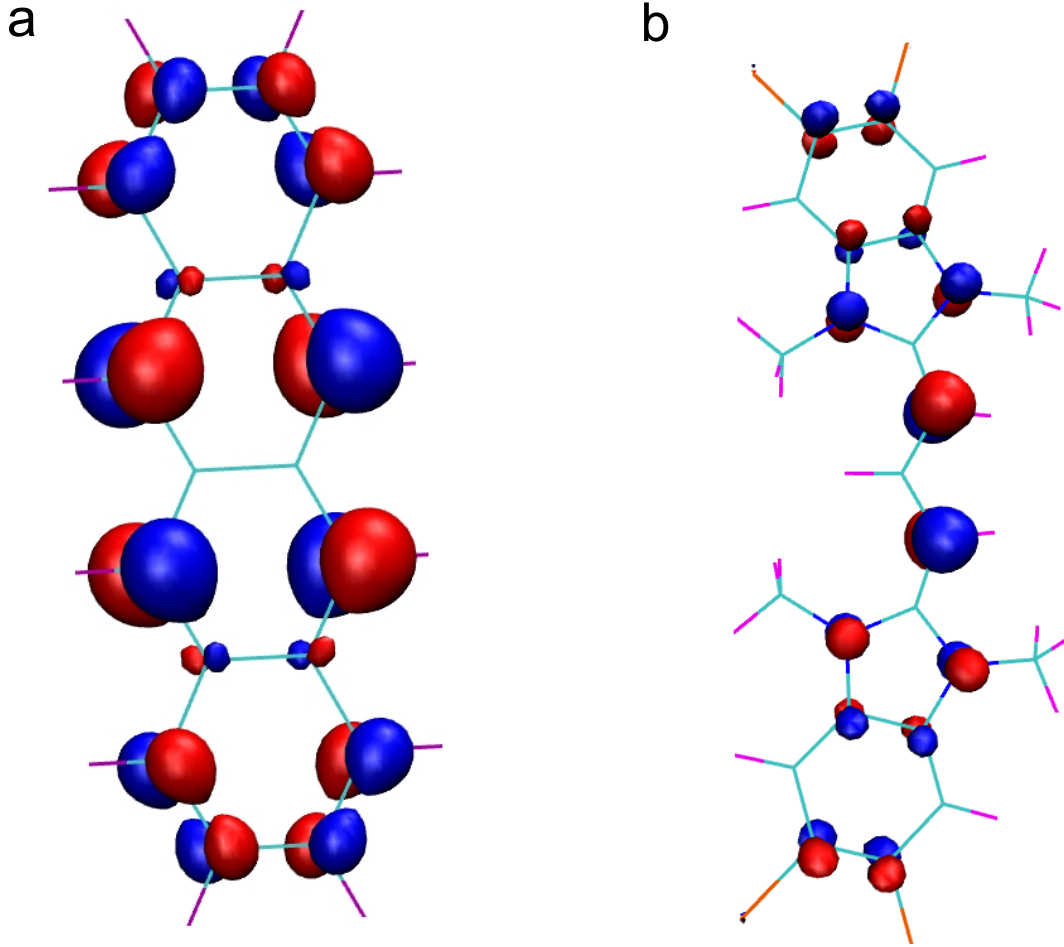


Figure IV.2: HOMO of TET (a) and CCY (b).

Since the investigated molecules are virtually planar, two geometries for the hybrid system are discussed as shown in Fig. IV.3, i.e. the perpendicular orientation and the parallel orientation where the normal vectors of the molecule's plane and the NS surface are perpendicular and parallel to each other, respectively. Further,  $d$  is the distance of the center of mass of the molecule to the surface. Based on the theory from Sec. II.4.1 and II.3, the electronic structure of TET and CCY with/without NS is calculated by the dftb+ code [108] together with the halorg-0-1 Slater-Koster parameter set [77, 112]. The code has been modified such as to include the potential (II.84), which by itself is calculated with a home-made program. Given some initial set of Mulliken charges obtained without the NS, potential and Mulliken charges are iteratively adjusted until self-consistency. The threshold for the latter was set to  $10^{-5}$  for changes in  $V_{\text{pol}}(\vec{r})$ . The self-consistent polarization energy  $E_{\text{pol}}^{\text{SC}}(r) = eV_{\text{pol}}(\vec{r})$  will be discussed below.

In the following, the influence of the polarization of the molecule due to the NS will be studied in dependence on the orientation and distance of the molecule and the radius of the NS. The analysis will be based on the change of Mulliken charges from Eq. (II.120) due to the interaction with the NS, i.e.  $\Delta q_A = q_\alpha - q_A^{\text{free}}$ , here  $q_A^{\text{free}}$  are the Mulliken charges of the bare

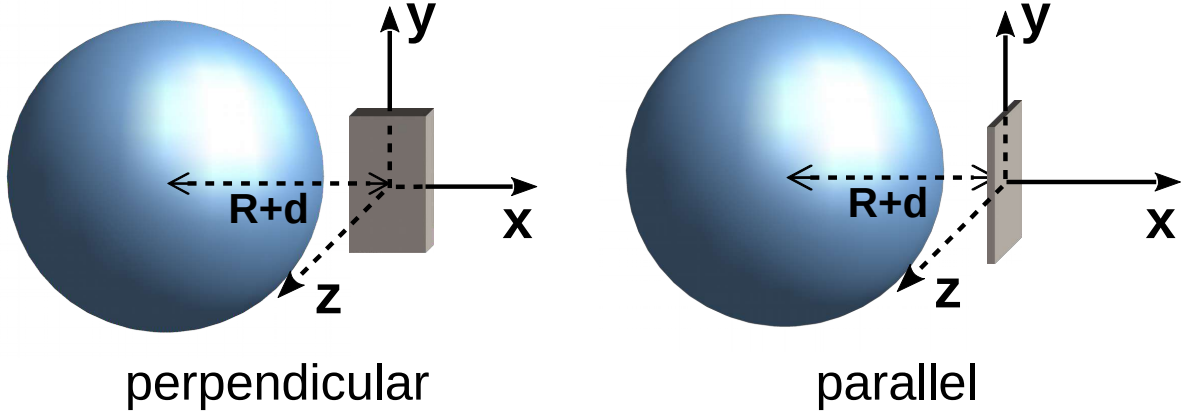


Figure IV.3: The perpendicular and parallel orientations of the molecule with respect to the spherical NS.  $R$  is the NS's radius and  $d$  is the distances from the sphere's surface to the molecule's center-of-mass. Within the respective planes the molecules are positioned such that the center-of-masses are at the origin of the molecule-fixed coordinate system as indicated and the principal axes point along the local  $x, y, z$ -axis.

atom. As a global measure the root-mean-squared deviation

$$\Delta q = \sqrt{\sum_A (q_A - q_A^{\text{free}})^2} \quad (\text{IV.1})$$

will be used. Further, the change in dipole moment is given by  $\Delta\boldsymbol{\mu} = \boldsymbol{\mu} - \boldsymbol{\mu}^{\text{free}}$ , and the fluctuation in total energy of the molecule due to the polarization potential of the NS is represented as  $\Delta E = E - E^{\text{free}}$ . Here,  $\boldsymbol{\mu}^{\text{free}}/E^{\text{free}}$  are from the case without the NS. Focusing on the energy change, i.e. the interaction energy, results from the solutions of the DFTB equations will be compared with the classical expression for the energy of the Mulliken charges in the polarization potential

$$E_{\text{pol}} = \sum_A q_A V_{\text{pol}}(R_A) \quad (\text{IV.2})$$

## 1.2 RESULTS

### CASE OF TETRACENE

The convergence of  $V_{\text{pol}}$  in Eq. (II.84) for the upper summation limit  $m$  is chosen with respect to changes with a threshold of  $10^{-5}$ . Typical values for the  $m$  are different due to the radius  $R$  of NS and distance  $d$ , which is shown in Tab. IV.1. From the numbers, one can find the order  $m$  needs to be higher to reach the threshold when the radius  $R$  becomes larger or the distance  $d$  becomes smaller.

Fig. IV.4a shows the polarization potential in the perpendicular orientation for a NS with radius  $R = 100 \text{ \AA} \gg L_{\text{mol}}$  and  $d = 3.5 \text{ \AA}$  (Noting the width across the short axis of TET is  $5 \text{ \AA}$ , in this case the distance for the closest atom of TET to the surface of NS is  $1 \text{ \AA}$ ). Thus  $E_{\text{pol}}^{\text{SC}}$  is shaped by the positive partial charges at the H atoms, which are closest to the NS. The maximum potential difference is about  $0.15 \text{ eV}$  across the short axis of the molecule. The change



Table IV.1: Expansion order  $m$  for TET with different  $R$  and  $d$  in the perpendicular/parallel orientations.

$d$ (Å)	$R$ (Å)				
	3	6	12	50	100
3.5	11/11	16/15	24/18	65/71	109/134
4	11/11	12/11	19/16	55/56	89/100
4.5	11/11	11/11	16/15	47/48	79/85
5.5	11/11	11/11	13/12	39/37	66/63
6.5	11/11	11/11	11/11	33/33	56/57
7.5	11/11	11/11	11/11	29/29	50/51
12.5	11/11	11/11	11/11	19/20	32/34
17.5	11/11	11/11	11/11	14/15	24/25

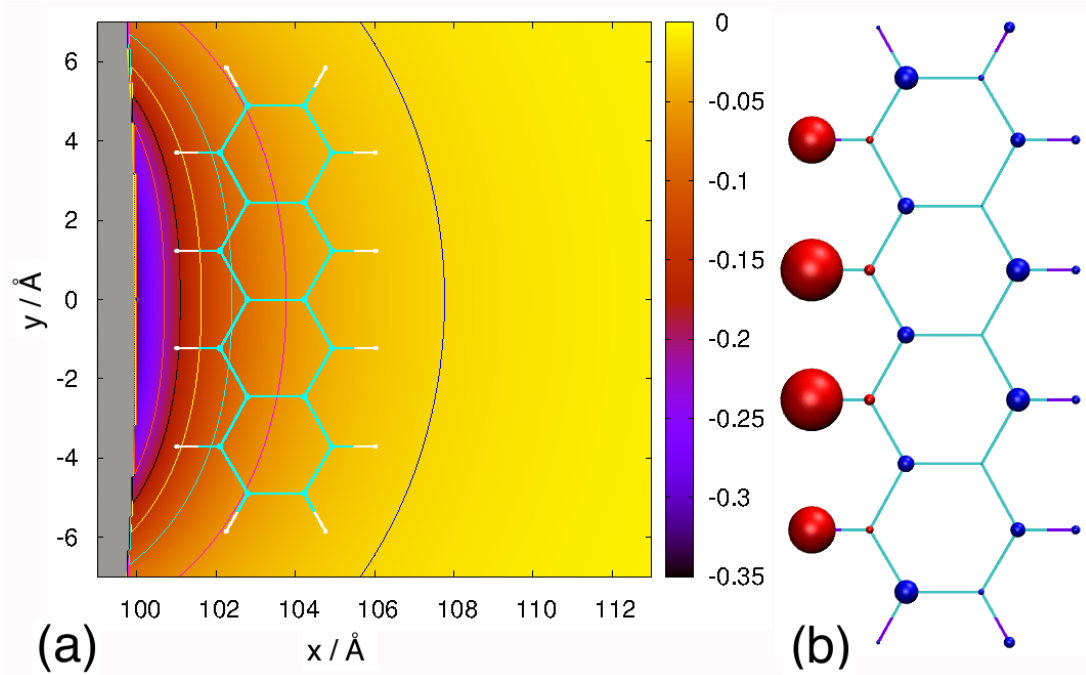


Figure IV.4: Left: The self-consistent polarization potential  $E_{\text{pol}}^{\text{SC}}$  (color bar in eV, contour values: -0.22, -0.18, -0.14, -0.1, -0.06, -0.02) for TET in perpendicular orientation and for  $R = 100$  Å and  $d = 3.5$  Å (The grey area corresponds to the NS.). Right: The change of Mulliken charges  $\Delta q_A$ ; maximum at  $0.0039 e$ .

in the electron density as expressed by the Mulliken charges is very small, which is shown in Fig. IV.4b. It reaches a maximum value of  $0.004 e$  or 5% in relative change for the close hydrogen atoms.

The influence from the NS on the molecule's electron density is more obvious if TET is in the parallel orientation as shown in Fig. IV.5. Here,  $E_{\text{pol}}^{\text{SC}}$  is shaped by the negative partial charges from the C atoms in the center of TET (cf. Fig. IV.1a). The change of  $E_{\text{pol}}^{\text{SC}}$  across the molecule is about 0.5 eV and causes the change in Mulliken charges of maximum up to  $0.02 e$ . Although still small in absolute number, it reaches a relative change of about 40%.

Figs. IV.6 – IV.7 show the results for  $R = 3$  Å  $< L_{\text{mol}}$  at the same distances and orientations as discussed before. In perpendicular orientation, the maximum potential difference is only

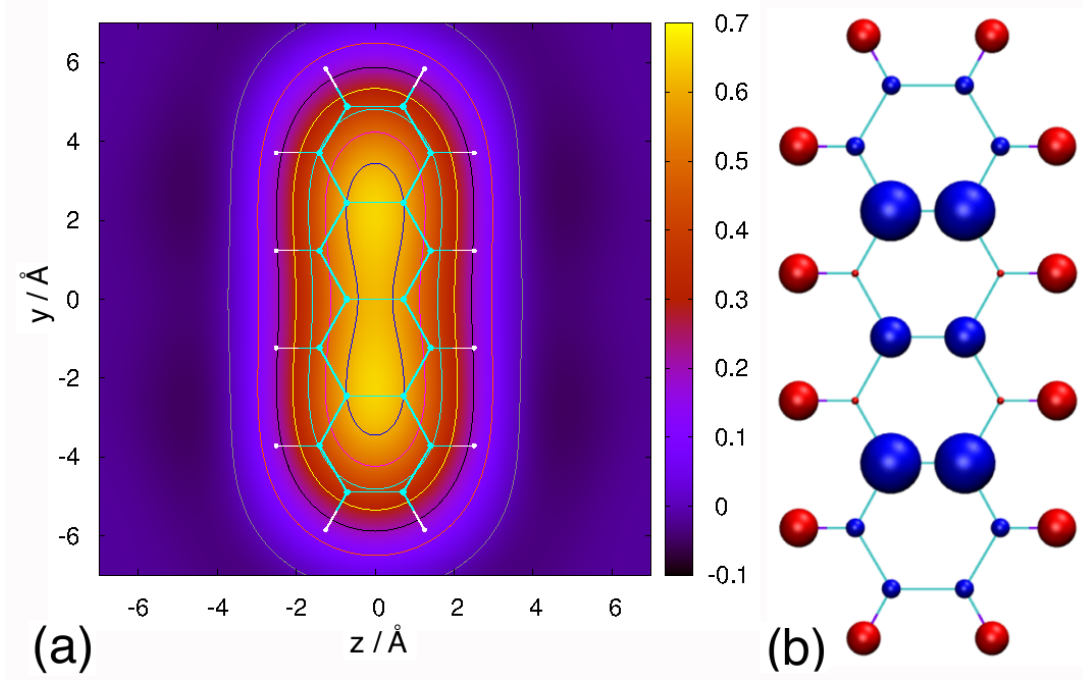


Figure IV.5: Left: The self-consistent polarization potential  $E_{\text{pol}}^{\text{SC}}$  (color bar units in eV, contour values: 0, 0.1, 0.2, 0.3, 0.4, 0.5, 0.6) for TET in parallel orientation and for  $R = 100 \text{ \AA}$  and  $d = 1.0 \text{ \AA}$ . Right: The change of Mulliken charges  $\Delta q$ ; maximum at  $0.0172 e$ .

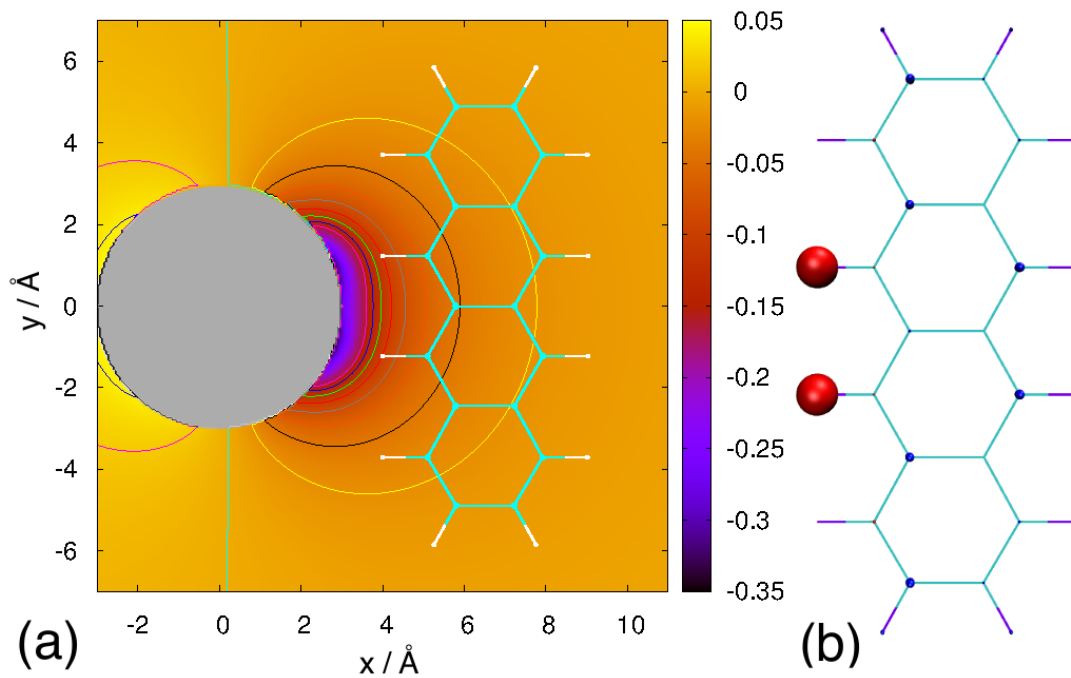


Figure IV.6: Left: The self-consistent polarization potential  $E_{\text{pol}}^{\text{SC}}$  (color bar in eV, contour values: -0.1, -0.08, -0.06, -0.04, -0.02) for TET in perpendicular orientation and for  $R = 3 \text{ \AA}$  and  $d = 3.5 \text{ \AA}$  (The grey area corresponds to the NS). Right: The change of Mulliken charges  $\Delta q_A$ ; maximum at  $0.0026 e$ .

about 0.08 eV across the short axis. And the change for the Mulliken charges reaches a maximum value of 0.003  $e$  or 3% in the relative change. In parallel orientation, the maximum potential difference is about 0.22 eV across the short axis. And the change for the Mulliken charges reaches a maximum value of 0.0089  $e$  or 21% in relative change. Comparing the results for different radii of NS from Figs. IV.4 – IV.7, one finds that the polarization potential and the magnitude of the changes in Mulliken charges will decrease when the radius of the NS become smaller. And the trend for the change of Mulliken charge is very similar in the perpendicular orientation. However the changes in the parallel case are only on the nearest two carbon orientation due to the small radius and distance from the surface of NS.

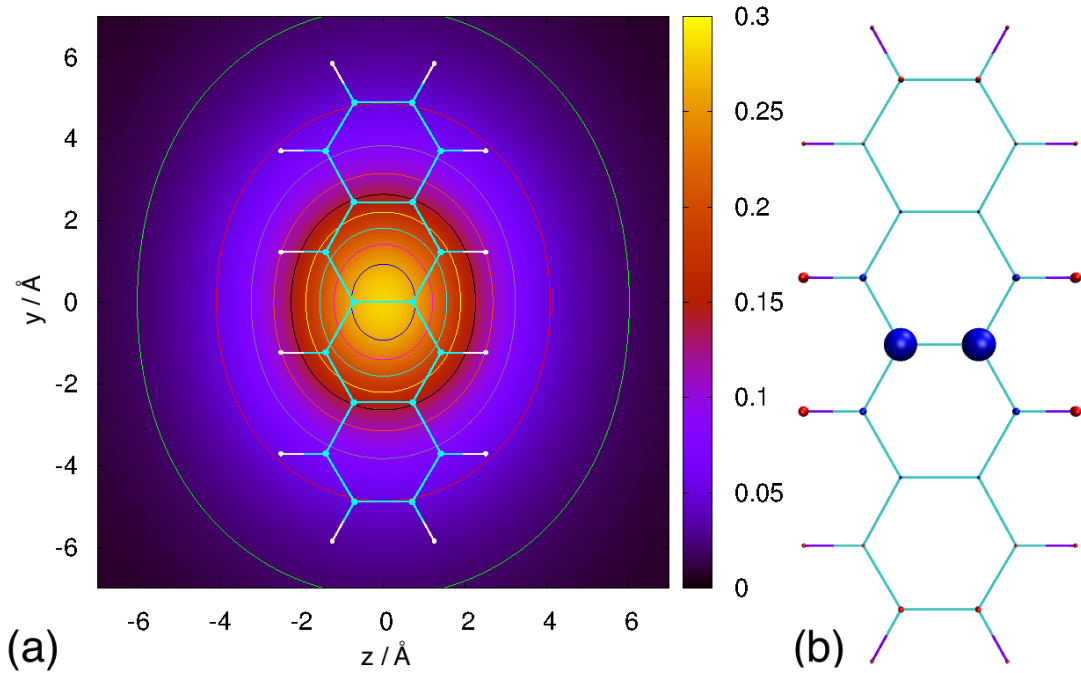


Figure IV.7: Left: The self-consistent polarization potential  $E_{\text{pol}}^{\text{SC}}$  (color bar units in eV, contour values: 0.02, 0.05, 0.08, 0.11, 0.14, 0.17, 0.2, 0.23, 0.26) for TET in parallel orientation and for  $R = 3 \text{ \AA}$  and  $d = 1.0 \text{ \AA}$ . Right: The change of Mulliken charges  $\Delta q$ ; maximum at 0.0089  $e$ .

Fig. IV.8 shows the dependence of  $\Delta E$ ,  $\Delta q$ , and  $\Delta\mu$  on the distance from the NS and the different NS radii. In total, the effect of the NS on the molecular charge density is short-ranged and the influence on  $\Delta E$  and  $\Delta q$  is larger in the parallel orientation as compared with the perpendicular one. In addition, the influence of the NS could be neglected essentially once the distance to the closest atom exceeds about 5  $\text{\AA}$ , independent on the radius of the NS. More specifically the distance dependence of  $\Delta E$  is determined by the actual orientation. Using numerical fitting, one finds for short distances as shown in Fig. IV.8  $\Delta E \propto d^{-7}$  and  $\propto d^{-8}$  for  $R = 3 \text{ \AA}$  and 100  $\text{\AA}$ , respectively, in case of the perpendicular orientation. For the parallel orientation it is roughly  $\Delta E \propto d^{-2}$  in both cases.

Looking at the dependence on the NS radius  $R$ , we notice that the changes in interaction energy and Mulliken charges decrease in magnitude with increasing  $R/L_{\text{mol}}$ . Closer inspection shows that in this case parts of the molecule are essentially too far away from the now much smaller NS, such that the respective charge densities do not contribute to the polarization field.

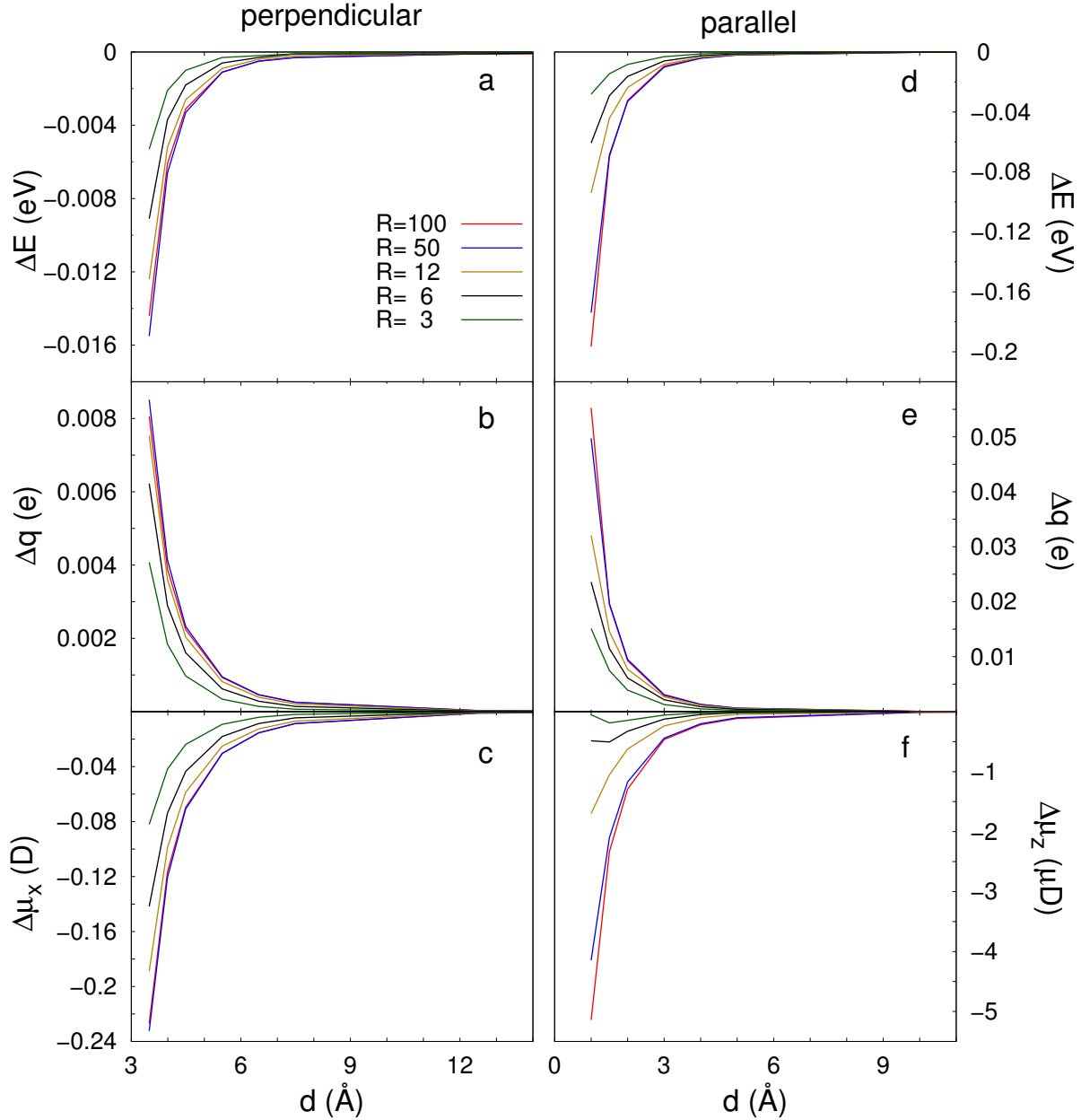


Figure IV.8: The dependence of interaction energy,  $\Delta E$ , change of Mulliken charge,  $\Delta q$ , and dipole moment,  $\Delta\mu$ , on the distance,  $d$ , from the surface of the NS and its radius (in Å) for the case of TET.

The quantum mechanical DFTB interaction energy  $\Delta E$ , can be compared to the classical expression in Eq. (IV.2). The difference  $\Delta E_{\text{com}} = \Delta E - E_{\text{pol}}$  is shown in Fig. IV.9. Differences occur only for short distances and are very small. In fact for all perpendicular cases and around  $d \approx 4 - 5$  Å  $E_{\text{pol}}$  contributes above 95 % to  $\Delta E$ , whereas for the parallel cases it is above 90 %.

The dipole moment is also changed by the polarization field as shown in panels c and f of Fig. IV.8. In the perpendicular orientation (plane of molecule is  $xy$ ) the  $x$ -component of

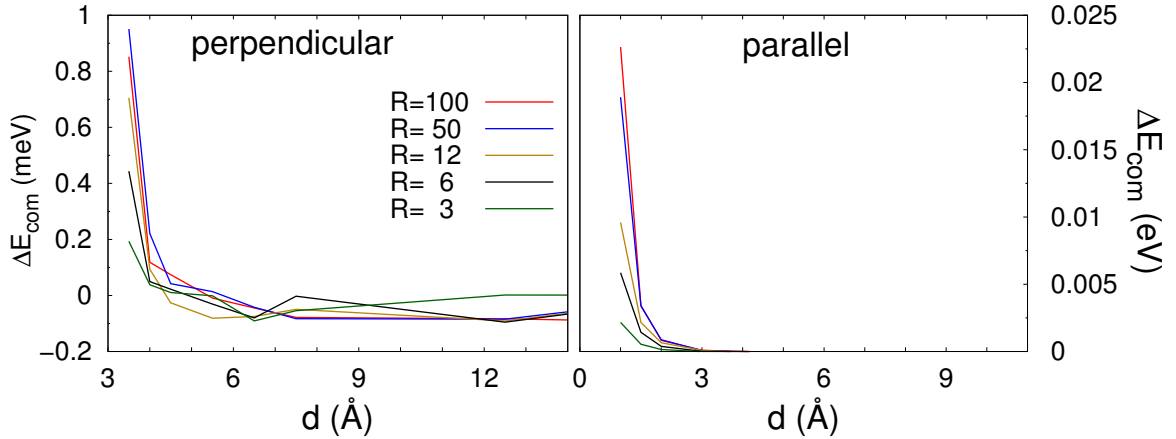


Figure IV.9: The dependence of energy difference  $\Delta E_{\text{com}}$  between  $\Delta E$  and  $E_{\text{pol}}$  on the distance,  $d$ , from the surface of the NS and its radius (in  $\text{\AA}$ ) for the case of TET.

dipole moment for TET changes due to the positive charge accumulation close to the NS (cf. Fig. II.84). In the parallel orientation (plane of molecule is  $yz$ ) there is not an obvious change in the dipole moment, which is a consequence of the symmetry of the setup.

#### CASE OF CCY

The charge neutrality of TET yielded the effect of the NS on the electron density to be rather small. The situation is expected to change for CCY, which carries a net charge of  $+1 e$ . The convergence of  $V_{\text{pol}}$  in Eq. (II.84) for the upper summation limit  $m$  is also chosen with respect to changes with a threshold of  $10^{-5}$ . Typical values for the  $m$  are also different due to the radius  $R$  of NS and distance  $d$  for TET, which is shown in Tab. IV.2. From the number, one can find the order  $m$  needs to be higher to reach the threshold when the radius  $R$  becomes larger or the distance  $d$  becomes smaller.

Table IV.2: Expansion order  $m$  for CCY with different  $R$  and  $d$  in the perpendicular/parallel orientations.

$d$ ( $\text{\AA}$ )	$R$ ( $\text{\AA}$ )			
	9	18	36	100
4	31/32	64/61	124/115	286/294
4.5	24/25	45/47	76/85	196/167
5	20/19	35/33	63/60	151/150
6	16/16	27/28	48/49	114/121
7	14/14	23/23	39/40	92/89
8	12/12	19/19	33/32	75/72
13	11/11	13/13	21/20	46/45
18	11/11	11/11	16/16	35/35

Fig. IV.10 shows the polarization potential  $E_{\text{pol}}^{\text{SC}}$  in the parallel orientation for a NS with radius  $R = 100 \text{ \AA} \gg L_{\text{mol}}$  and  $d = 4 \text{ \AA}$  (Noting the width across the short axis of CCY is  $6 \text{ \AA}$ , in this case the distance for the closest atom of CCY to the surface of NS is also  $1 \text{ \AA}$ ). Overall, the potential change across the molecule is about  $2 \text{ eV}$  and the maximum change in Mulliken

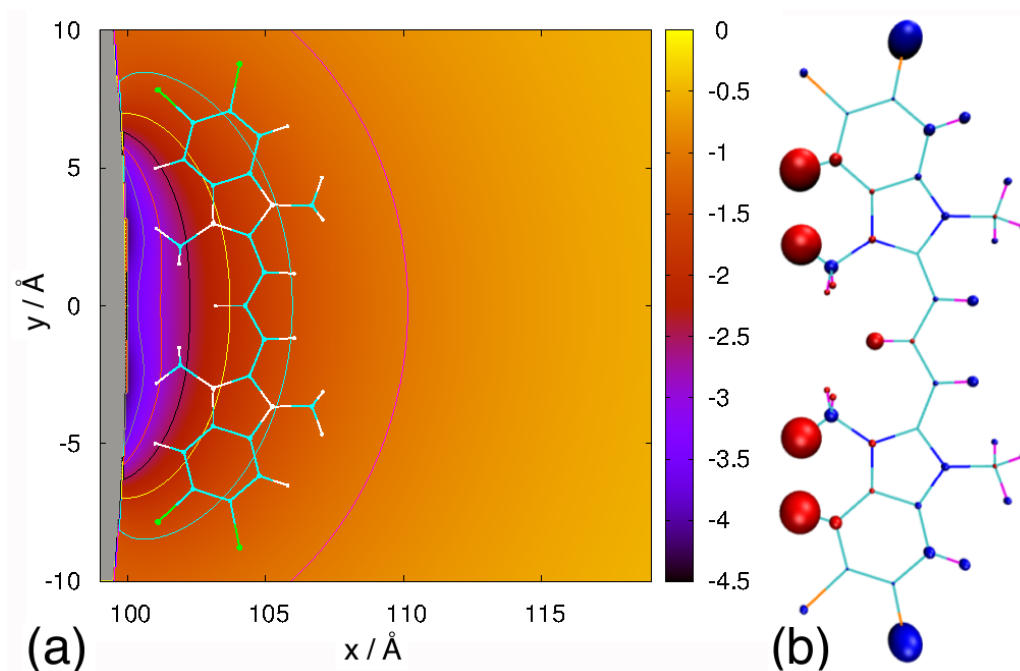


Figure IV.10: Left: The self-consistent polarization potential  $E_{\text{pol}}^{\text{SC}}$  (color bar units in eV, contour values: -3.5, -3, -2.5, -2, -1.5, -1) for CCY in perpendicular orientation and for a  $R = 100 \text{ \AA}$  and  $d = 4.0 \text{ \AA}$ . Right: The change of Mulliken charges  $\Delta q$ ; maximum at  $0.0291 e$ .

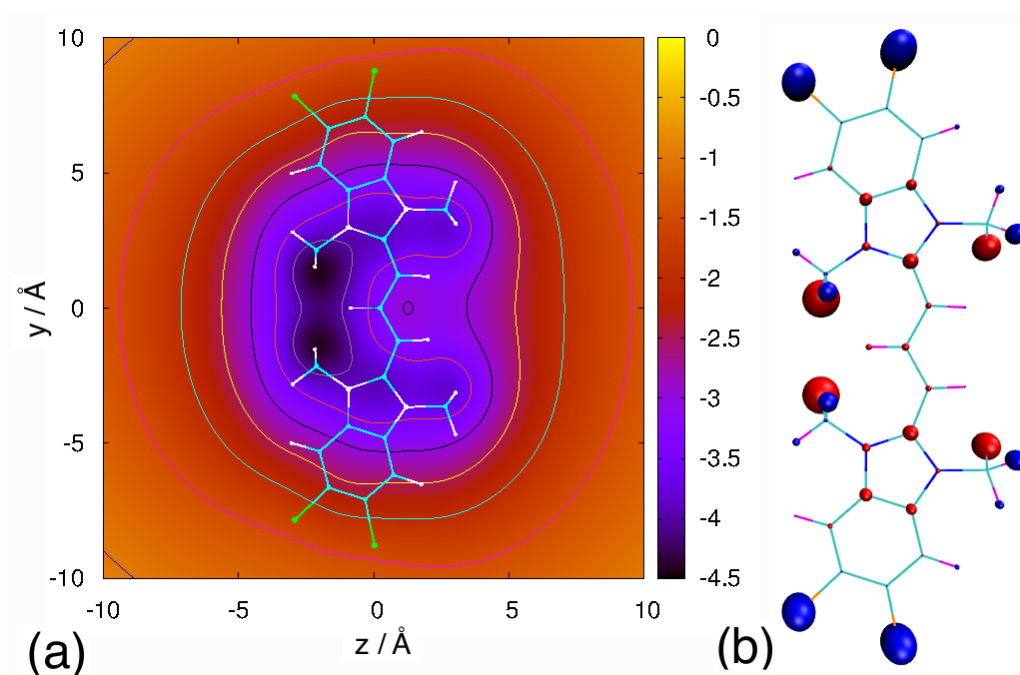


Figure IV.11: Left: The self-consistent polarization potential  $E_{\text{pol}}^{\text{SC}}$  (color bar units in eV, contour values: -4, -3.5, -3, -2.5, -2, -1.5) for CCY in parallel orientation and for a  $R = 100 \text{ \AA}$  and  $d = 1.9 \text{ \AA}$ . Right: The change of Mulliken charges  $\Delta q$ ; maximum at  $0.0343 e$ .

charge is  $0.029 e$ , i.e. 42% in relative change. The largest change occurs for the H-atoms, which are closest to the NS. In addition, negative charge is accumulated at the Cl-atoms.

In the parallel orientation from the results shown in Fig. IV.11 one first notices that compared with TET the polarization potential has a significantly lower symmetry in accord with the different symmetry group the two molecules belong to. The potential changes about 3 eV across the molecule and maximum changes of the Mulliken charges reach 0.034  $e$  or 50% in relative change. They are especially pronounced for those H-atoms which are out of the molecular plane and thus closest to the surface of the NS. Moreover Cl-atoms acquire some extra negative charge.

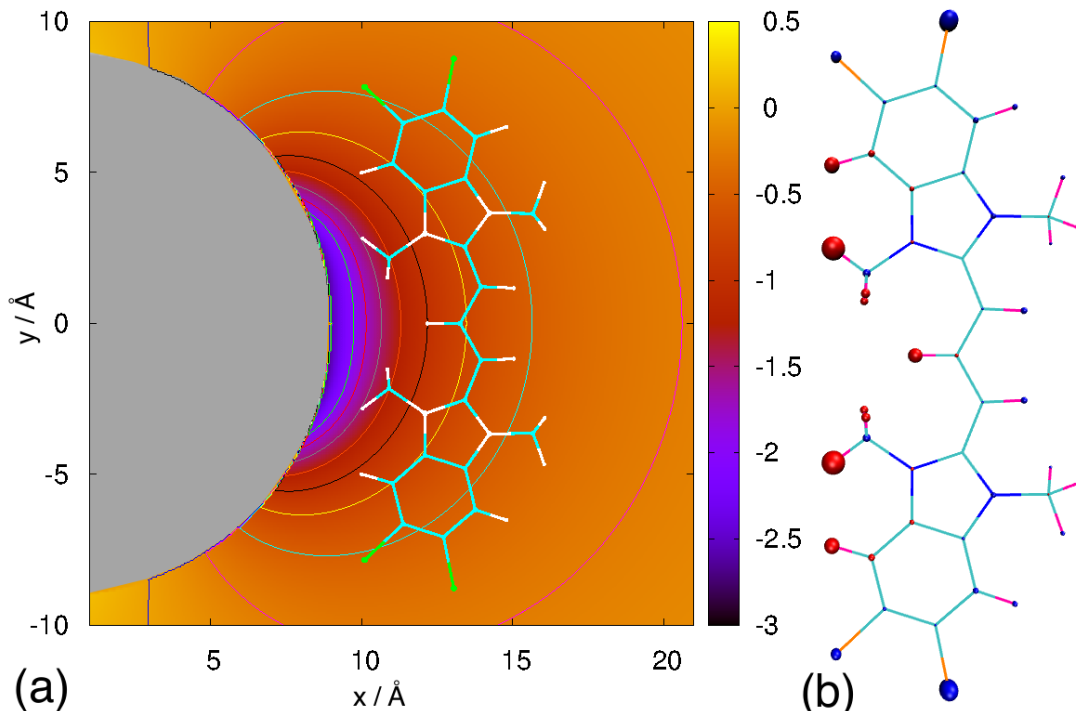


Figure IV.12: Left: The self-consistent polarization potential  $E_{\text{pol}}^{\text{SC}}$  (color bar units in eV, contour values: -1.5, -1.25, -1, -0.75, -0.5, -0.25) for CCY in perpendicular orientation and for a  $R = 9 \text{ \AA}$  and  $d = 4.0 \text{ \AA}$ . Right: The change of Mulliken charges  $\Delta q$ ; maximum at 0.0151  $e$ .

Figs. IV.12 – IV.13 show the polarization potential with radius  $R = 9 \text{ \AA} < L_{\text{mol}}$  in the same distance and orientations. Overall, the potential change across the molecule is about 1.3 eV and the change in Mulliken charge is 0.015  $e$ , i.e. 22 % in relative change for the perpendicular orientation case. And in parallel orientation, the potential change across the molecule is about 1.5 eV and the change in Mulliken charge is 0.024  $e$ , i.e. 35 % in relative change. Comparing with the result for different radius of NS, one can find the polarization potential and the change will decrease with the decreasing radius, and the trend is very similar in both orientations.

Fig. IV.14 shows the dependence of  $\Delta E$ ,  $\Delta q$ , and  $\Delta \mu$  on the distance  $d$  from the NS for different radii  $R$ . First, we note that the effect of the NS is not as short-ranged as in the case of TET due to the presence of a net charge. Further, for  $\Delta E$  and  $\Delta q$  the orientation is much less important than in the case of TET. Only the orientation dependence of  $\Delta \mu$  is as pronounced for CCY as it is for TET.

Inspecting the distance dependence of  $\Delta E$  in the ranges shown in Fig. IV.14 one finds by numerical fitting irrespective of the NS's radius  $\Delta E \propto d^{-2}$  and  $\Delta E \propto d^{-1}$  in case of the perpendicular and parallel orientation, respectively. Comparing with the result for TET in

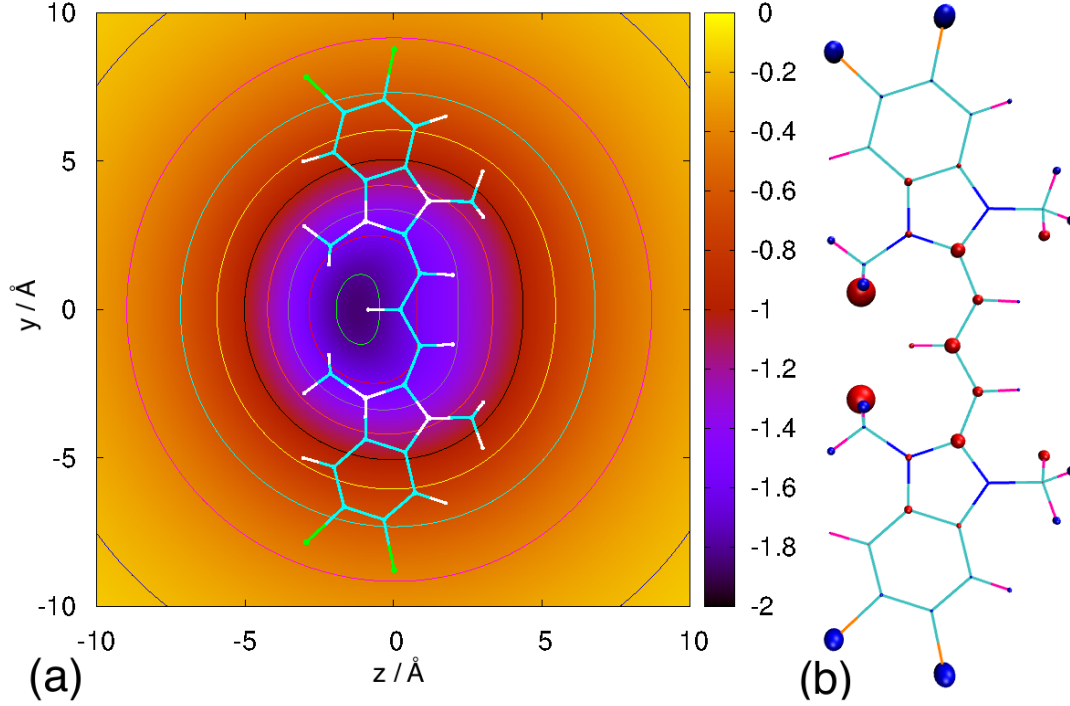


Figure IV.13: Left: The self-consistent polarization potential  $E_{\text{pol}}^{\text{SC}}$  (color bar units in eV, contour values: -1.8, -1.6, -1.4, -1.2, -1, -0.8, -0.6, -0.4, -0.2) for CCY in parallel orientation and for a  $R = 9 \text{ \AA}$  and  $d = 1.9 \text{ \AA}$ . Right: The change of Mulliken charges  $\Delta q$ ; maximum at  $0.0239 e$ .

Fig. IV.8, one can find that the changes for CCY are larger than for TET. Especially even if the distance from the closest atom to the surface of NS exceeds  $10 \text{ \AA}$ , the energy change is  $\Delta E \approx -0.5 \text{ eV}$  in both orientation, i.e. for CCY the effect of the polarization potential of the NS is long-ranged.

Concerning the dependence on the radius of the NS, the trend is rather similar to the case of TET, i.e. for NSs with  $R \ll L_{\text{max}}$  parts of the molecular charge density are located outside the range of effective interaction. Fig. IV.15 shows the difference  $\Delta E_{\text{com}}$  between the DFTB interaction energy  $\Delta E$  and the classical expression  $E_{\text{pol}}$  from Eq. (IV.2). For all perpendicular cases and around  $d \approx 4 - 5 \text{ \AA}$   $E_{\text{pol}}$  also contributes above 95 % to  $\Delta E$ .

### SOME ESTIMATES

In the following the previous results will be compared with a simple classical model. In particular, the dependencies on the different distances and the sphere radius observed for the charged CCY and the neutral TET will be discussed. Two classical cases for the polarization energy from Eq. (IV.2) are considered to investigate CCY and TET, i.e. a single point charge and a dipole oriented along the surface normal. The results for the classical cases can be simple obtained from an ideal uncharged metal sphere, which has the following analytical solution

$$E_{\text{ideal}}(r) = \frac{qq'}{4\pi\epsilon_0} \left( \frac{1}{r-r'} - \frac{1}{r} \right) \quad (\text{IV.3})$$

with the image charge  $q' = -qR/r$  at position  $r' = R^2/r$ .



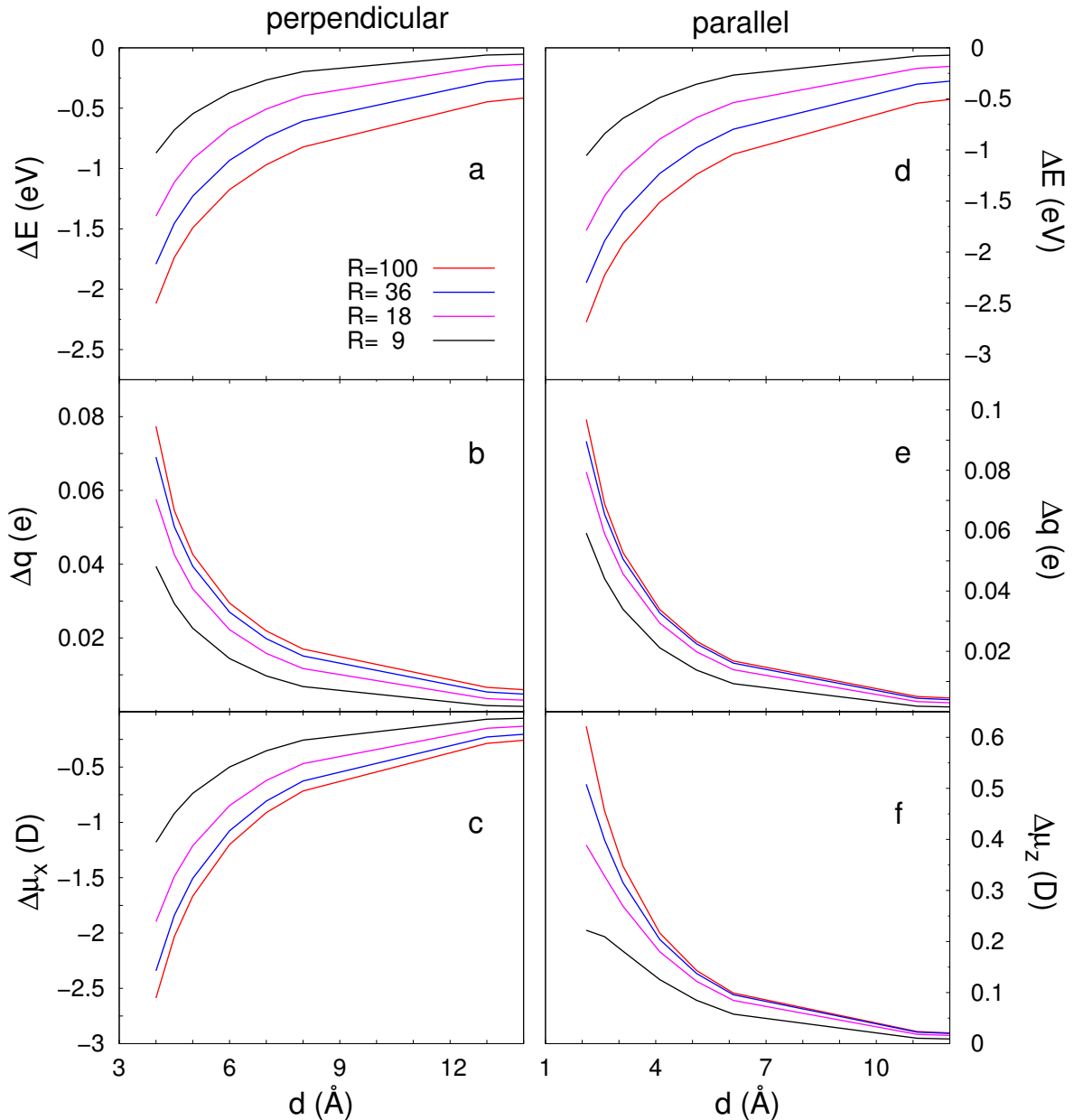


Figure IV.14: The dependence of interaction energy,  $\Delta E$ , change of Mulliken charge,  $\Delta q$ , and dipole moment,  $\Delta\mu$ , on the distance from the surface of the NS and its radius for the case of CCY.

Fig. IV.16 shows the distance and sphere radius dependence for the two ideal cases, CCY and TET in the perpendicular orientation. One notices that for large distances the interaction energy  $\Delta E$  for TET tends to the ideal dipole model and for CCY tends to the ideal point charge model. However, in the short distance for TET the interaction energy from DFTB is smaller than the ideal result. It is understood easily that when TET very close to the NS, TET is more like some point charges for the NS than the ideal dipole moment and should have lower energy.

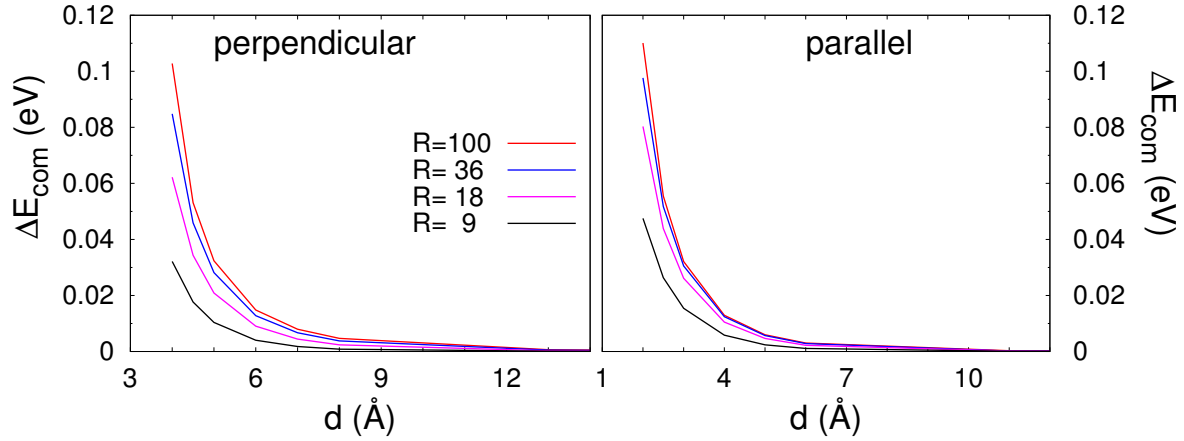


Figure IV.15: The dependence of energy difference  $\Delta E_{\text{com}}$  between  $\Delta E$  and  $E_{\text{pol}}$  on the distance,  $d$ , from the surface of the NS and its radius (in  $\text{\AA}$ ) for the case of CCY.

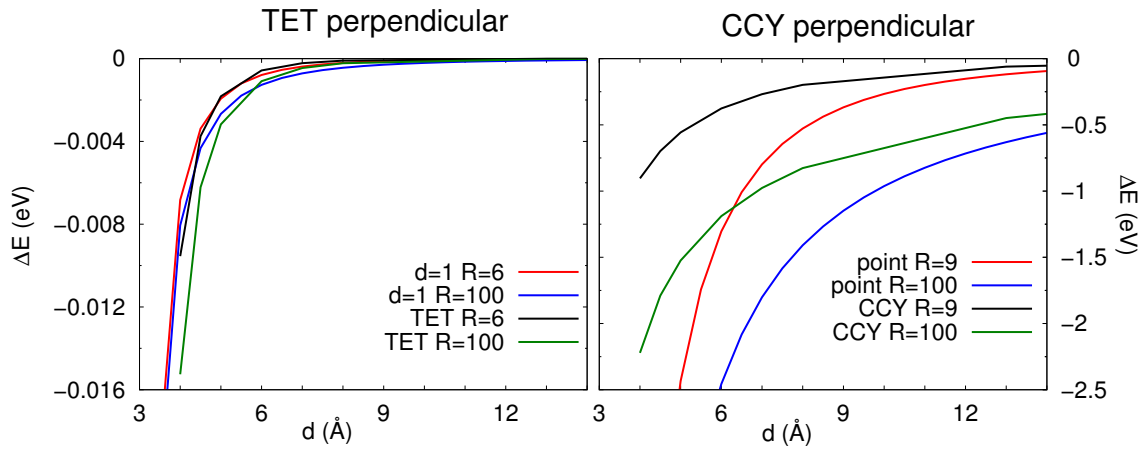


Figure IV.16: Left panel: the dependence of the polarization energy from Eq. (IV.3) for a dipole of strength  $d = 1$  D (dipole oriented parallel to the surface normal) on the distance  $d$  from the surface of a NS is compared with the interaction energy  $\Delta E$  for TET in the perpendicular orientation with different radius  $R$ . In right panel the ideal polarization energy for a single charge  $q = 1 e$  is compared with the interaction energy  $\Delta E$  for CCY in the perpendicular orientation.

Similarly, for CCY when very close to the NS, CCY could not be assumed as single ideal point charge. This is the reason for the polarization energy of an ideal point charge being lower than  $\Delta E$  for small distances. Similar results are obtained for the parallel orientation.

## 2 EXTERNAL FIELD DRIVEN DYNAMICS

### 2.1 MODEL SYSTEM

The scheme of the hybrid system in the external field is shown in Fig. IV.17. From the result in Sec. IV.1, it is clear that the effect of the NS on the molecule is small enough to be neglected for distances  $> 15 \text{\AA}$ . In addition, the enhancement of the external field  $E_{\text{ext}}$  due to the NS is proportional to  $(R/r)^3$  from Eq. (II.91). So the NS's near-field approximately affects the nearest

molecule only. Thus it is not necessary to calculate the hybrid system all in TDDFT, but to use the Frenkel exciton theory from Sec. II.2.1. Thus it is assumed that all molecules except the nearest one are not affected by the near-field  $E_{\text{nf}}$  of NS. In the following the near-field is understood to contain the polarization field, from  $E_{\text{pol}} = -\nabla V_{\text{pol}}$  from Eq. (II.84) as well as the enhancement field from Eq. (II.91), i.e.

$$E_{\text{nf}}(\vec{r}, t) = \frac{2E_{\text{ext}}(t)(\varepsilon_r - 1)R^3}{(\varepsilon_r + 2)r^3} \cos \theta - \sum_{A=1}^N \sum_{l=1}^m \frac{q_A(t)(1 - \varepsilon_r)l}{(1 + \varepsilon_r)l + 1} \frac{R^{2l+1}}{r^{l+1}R_A^{l+1}} \left[ \frac{(l+1)\vec{r}P_l(\cos \theta)}{r^2} + \frac{l(\cos \theta P_l(\cos \theta) - P_{l-1}(\cos \theta))}{\sin^2 \theta} \left( \frac{\vec{R}_A}{rR_A} - \frac{\vec{r} \cos \theta}{r^2} \right) \right] \quad (\text{IV.4})$$

Hence the molecule next to the NS experiences the total field

$$E_{\text{tot}}(\vec{r}, t) = E_{\text{ext}}(t) + E_{\text{nf}}(\vec{r}, t) \quad (\text{IV.5})$$

whereas all other molecules interact with the external field only. Note that according to Eq. (II.39) the time dependent fields are taken to be constant across the molecule, i.e. with the value at its center of mass.

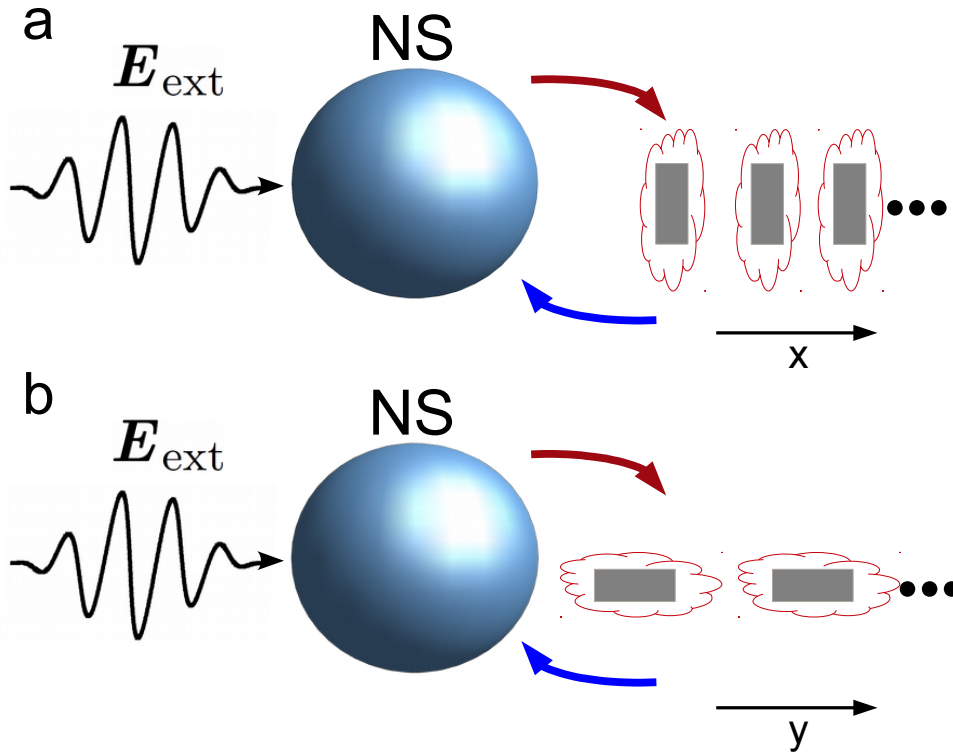


Figure IV.17: The scheme of the hybrid system in an external field  $E_{\text{ext}}$ . a) for TET and b) for CCY. Blue and red arrows indicate the interaction via the NS's near-field. Note that different orientations of the coordinate axes are used for better comparison of the molecular properties with Sec. IV.1.

Based on this assumption to build the Frenkel system, the hybrid system can be described

by three parts. First part is the NS, which is treated by classical electrodynamics as in Sec. II.3. Second part is the molecule nearest to the NS. Its charge distribution is affected by the total field  $E_{\text{tot}}$  in Eqs. (II.123) and (II.139), which is shown as the red arrow in Fig. IV.17. In addition the change of Mulliken charges will affect the NS via Eq. (II.84), which is assumed as the feed back from the nearest molecule to the NS, blue arrow in Fig. IV.17. Thus the nearest molecule need to be analysed by the approximate TDDFT (using a code from T. Niehaus [80]) to obtain the information for the Frenkel system. Note that only the static polarization field will be described self-consistently, similar to Sec. IV.1. During the TDDFT propagation the feed back loop is as follows. At each time step ( $\Delta t = 2.4$  as) the Mulliken charges are calculated in the total field, which contains the polarization field obtained from Eq. (II.123) using the Mulliken charges from the previous time step. The third part consists of the other molecules, which are not directly affected by the  $E_{\text{nf}}$  of NS. They are connected with the molecule nearest to the NS and among themselves by Coulomb couplings (Eq. (II.19)) as obtained from linear response TDDFT. For the propagation of the aggregate in the external field, a Frenkel exciton description in terms of single particle excitations is performed.

## 2.2 DYNAMICS OF THE MOLECULE NEAREST TO THE NS

As discussed in Sec. IV.2.1, one molecule near the NS (i.e. parts one and two) is simulated first to check the influence from the nearby NS in the external pulse. The external field is chosen as

$$E_{\text{ext}}(t) = E_0 \cos(\omega t) \sin^2\left(\frac{2\pi t}{t_{\text{max}}}\right) \theta(t)\theta(t_{\text{max}} - t) \quad (\text{IV.6})$$

where  $E_0$  is the field strength,  $\omega$  is the frequency,  $t_{\text{max}}$  is the duration time, i.e.  $E_{\text{ext}}(t) = 0$  when  $t > t_{\text{max}}$ .

First to prepare for a description of the molecule in the Frenkel basis, the molecular orbitals and absorption spectra need to be analysed, which is shown in Fig. IV.18 for TET and CCY. The results are obtained from the linear response TDDFT code [80] together with the halorg-0-1 Slater-Koster parameter set [77, 112]. In the figure, the first excited state  $E_1$  for TET is at 2.24 eV with the transition weight 99.93% from HOMO to LUMO and transition dipole moment  $\vec{\mu}_1 = (2.23, 0, 0)$  D. For CCY the first excited state  $E_1$  is at 2.67 eV with the transition weight 99.86% from HOMO to LUMO with the transition dipole moment  $\vec{\mu}_1 = (0, 12.91, 0.003)$  D (assuming the short axis of the molecule as  $x$ -direction and long axis as  $y$ -direction). Thus single electron molecular orbitals (HOMO and LUMO) are sufficient for an effective model if the field is resonant to the first excited state.

In the following the arrangements of the NS and molecules will be used as shown in Fig. IV.17a for TET and Fig. IV.17b for CCY. The dynamics will be analysed by taking the molecular orbitals for the free molecule as the reference, which means that the time evolution of the basis for the nearest molecule need to be projected into the reference framework. Note that the coefficient  $b_{\mu i}$  in Eq. (II.129) is time-dependent in the external field however the occupation number  $N_{\text{occ}}$  is time-independent from Sec. 4.2 in approximate TDDFT [80]. Thus from Eq. (II.129) the time-dependent occupation number  $N_{\text{occ}}^{\text{f}}(i, t)$  for the nearest molecule in the free molecular

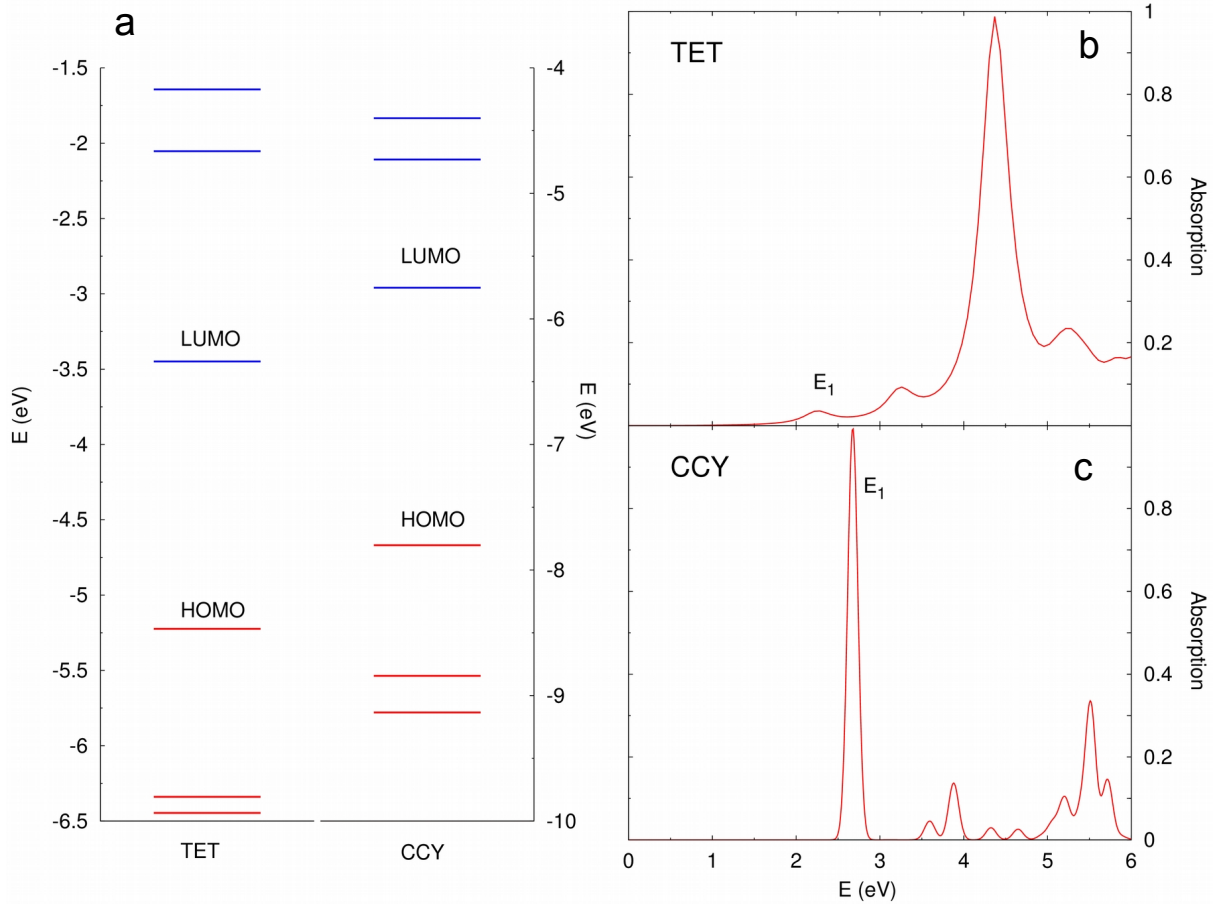


Figure IV.18: The molecular orbitals from HOMO-2 to LUMO+2 and absorption spectrum for free TET and CCY. The first excited state  $E_1$  is at 2.24 eV for TET and at 2.67 eV for CCY. The absorption spectrum of TET is a bit red-shifted as compared to the available low-resolution experimental data (first peak around 2.9 eV) [113]. For CCY no gas phase experimental data are available. DFT calculations for a closely related compound yield the maximum absorption at 2.5 eV [114].

state basis  $\Psi_i^f(\vec{r})$  reads

$$N_{\text{occ}}^f(i, t) = \sum_j^{\text{occ}} N_{\text{occ}}(j) \langle \Psi_i^f(\vec{r}) | \Psi_j(\vec{r}, t) \rangle \langle \Psi_j(\vec{r}, t) | \Psi_i^f(\vec{r}) \rangle = \sum_j N_{\text{occ}}(j) C_{ij}^*(t) C_{ik}(t) \quad (\text{IV.7})$$

with the coefficients overlap

$$C_{ij}(t) = \langle \Psi_j(\vec{r}, t) | \Psi_i^f(\vec{r}) \rangle = \sum_{\mu\nu} b_{\mu j}^*(t) \phi_{\mu}^* b_{\nu i}^f \phi_{\nu} = \sum_{\mu\nu} b_{\mu j}^*(t) b_{\nu i}^f S_{\nu\mu} \quad (\text{IV.8})$$

Results for the time dependent of occupation numbers of molecular orbitals ( $i = \text{HOMO} - 2, \dots, \text{LUMO} + 2$ ) for TET and CCY with an external pulse resonant to the first excited state  $E_1$ , are shown in Fig. IV.19. Here,  $t_{\text{max}} = 20$  fs, for TET  $E_0 = (5, 0, 0) \times 10^9$  V/m and  $\omega = 2.24$  eV with a  $R = 100$  Å NS at a distance of  $d = 3.5$  Å, and for CCY  $E_0 = (0, 5, 0) \times 10^8$  V/m and  $\omega = 2.67$  eV at  $d = 9.5$  Å. One can find that the transition are almost of HOMO-LUMO type

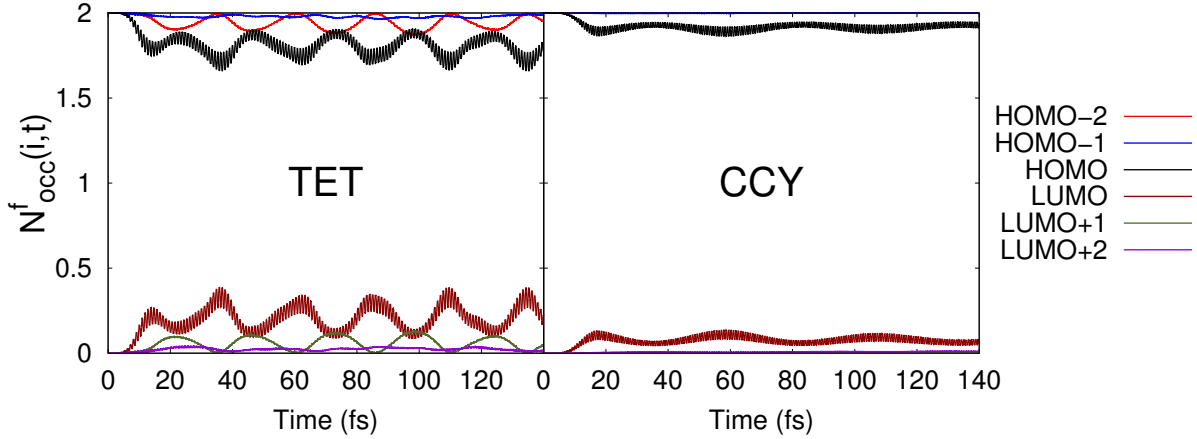


Figure IV.19: Time-evolution for molecular orbital occupation  $i = \text{HOMO} - 2, \dots, \text{LUMO} + 2$  for TET and CCY for a  $R = 100 \text{ \AA}$  NS with an external pulse  $t_{\text{max}} = 20 \text{ fs}$ , for TET  $E_0 = (5, 0, 0) \times 10^9 \text{ V/m}$  and  $\omega = 2.24 \text{ eV}$  at a distance of  $d = 3.5 \text{ \AA}$ , and for CCY with  $E_0 = (0, 5, 0) \times 10^8 \text{ V/m}$  and  $\omega = 2.67 \text{ eV}$  at  $d = 9.5 \text{ \AA}$ .

for CCY. However, for TET although the HOMO-LUMO transition is dominant, there are also noticeable transitions such as from HOMO-2 to LUMO+1 due to the strong external field.

Fig. IV.20 shows the time evolution for the hybrid of a NS and one TET molecule with a strong external field as in Fig. IV.19. In Fig. IV.20b the  $x$ -component of the polarization field  $E_{\text{pol},x}$  obtained from Eq. (II.84) is taken at the mass center of TET as the reference to show the changes. One can find that the polarization field oscillates with the frequency of the external field and a phase shift about  $136^\circ$ . There is also an oscillation with the same frequency for the dipole moment of TET, whose  $x$ -component,  $\mu_x$ , is shown in Fig. IV.20c. Fig. IV.20d shows the change of Mulliken charges  $\Delta q$  from Eq. (IV.1). It is found that the oscillation of  $\Delta q$  is driven by the external field. After the pulse one observes several oscillation frequencies according to the particular charge rearrangement in the molecule.

To check the influence from the NS, the  $x$ -component of the polarization field  $E_{\text{pol},x}$  at the mass center and the dipole moment  $\mu_x$  for TET are shown for different distances  $d$  in Fig. IV.21. Due to the different self-consistent electron distributions for TET coupled with the NS (Sec. IV.1) there are different initial polarization fields and dipole moments, which are found at  $t = 0$  from Fig. IV.21. However, the initial polarization field is so small that though it changes the molecular orbitals, there is no obvious difference for the resonant energy (smaller than  $0.001 \text{ eV}$ ). From the left panel, it is found that the oscillation amplitude of the polarization field becomes smaller with distance, but the oscillating frequency is independent of the distance and only dependent on the frequency of the external pulse. In the right panel due to the fact that  $|E_{\text{pol}}| \ll |E_{\text{ext}}|$  the difference in the oscillation amplitude of the dipole moment is very small for different distances. From Figs. IV.20 and IV.21, the effect of the NS on the molecule is mainly on the follows. First, due to the classical enhancement of the external field from the metal NS by Eq. (II.91), the molecule is more strongly excited than without NS. Second, due to the polarization field calculated from Eq. (II.84), after the pulse there is also a change of the oscillations of the Mulliken charges  $\Delta q$ , which means that weak excitation occurs by the

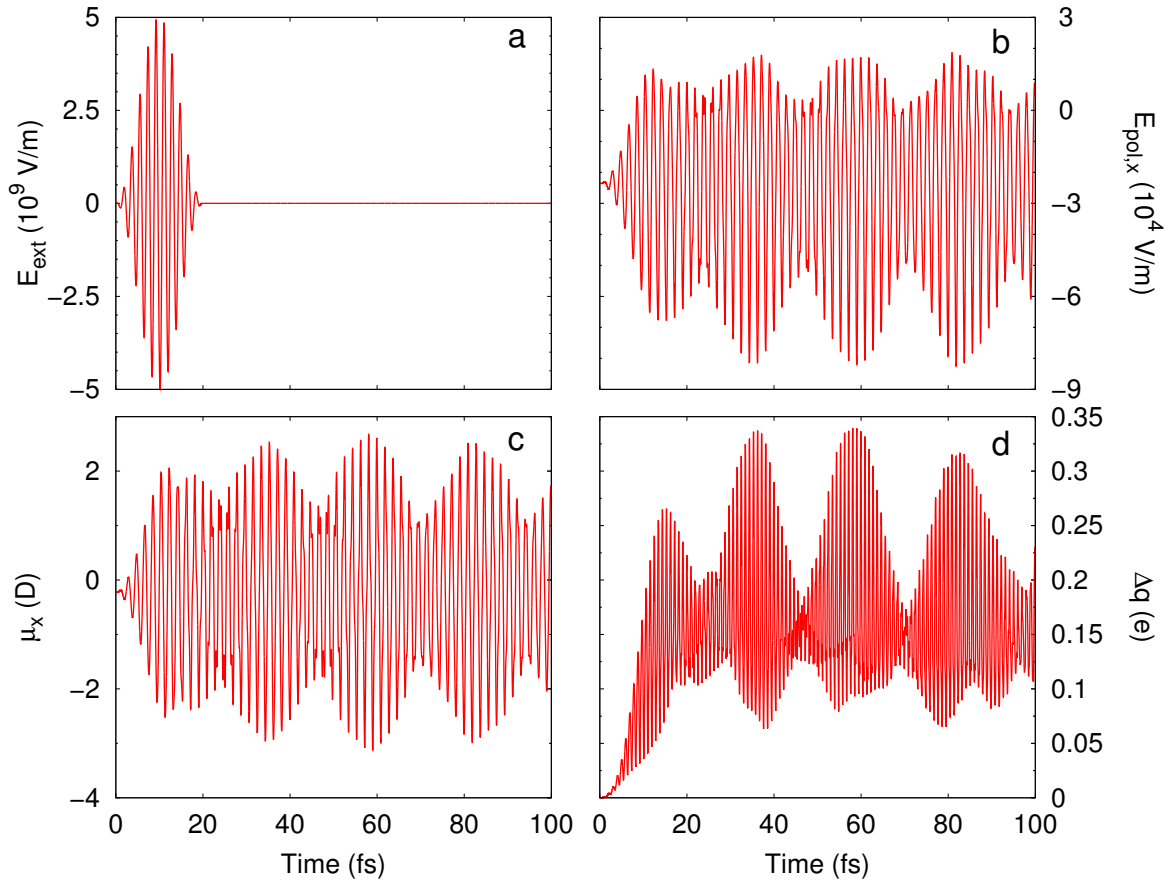


Figure IV.20: The time evolution for the external field  $E_{\text{ext}}$ , the  $x$ -component of the polarization field  $E_{\text{pol},x}$  at the mass center,  $x$ -component of the dipole moment  $\mu_x$  and change of Mulliken charges  $\Delta q$  for TET in arrangement as shown in Fig. IV.17a with a  $R = 100 \text{ \AA}$  NS and a distance of  $d = 3.5 \text{ \AA}$ .

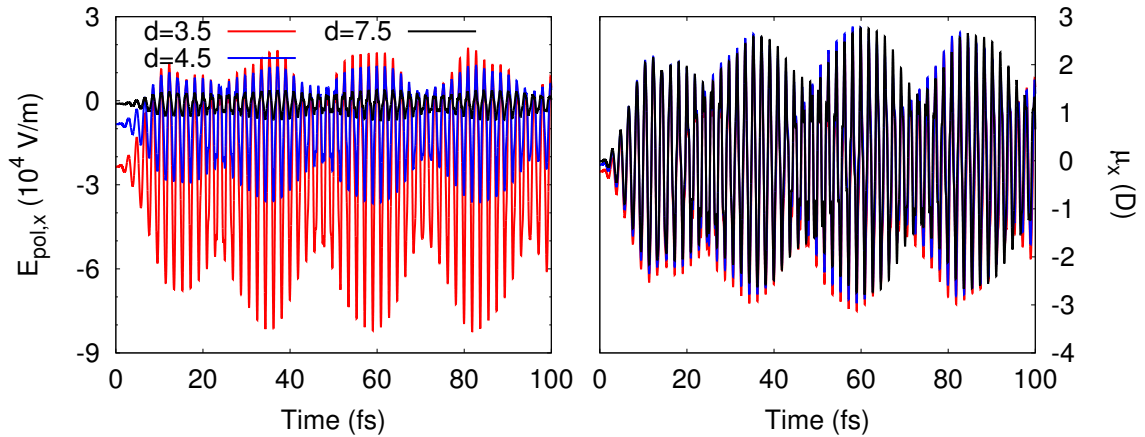


Figure IV.21: The time evolution for the polarization field at the mass center and the dipole moment the  $x$ -direction of TET at different distances of  $d = 3.5 \text{ \AA}$ ,  $d = 4.5 \text{ \AA}$  and  $d = 7.5 \text{ \AA}$  with a  $R = 100 \text{ \AA}$  NS.

polarization field.

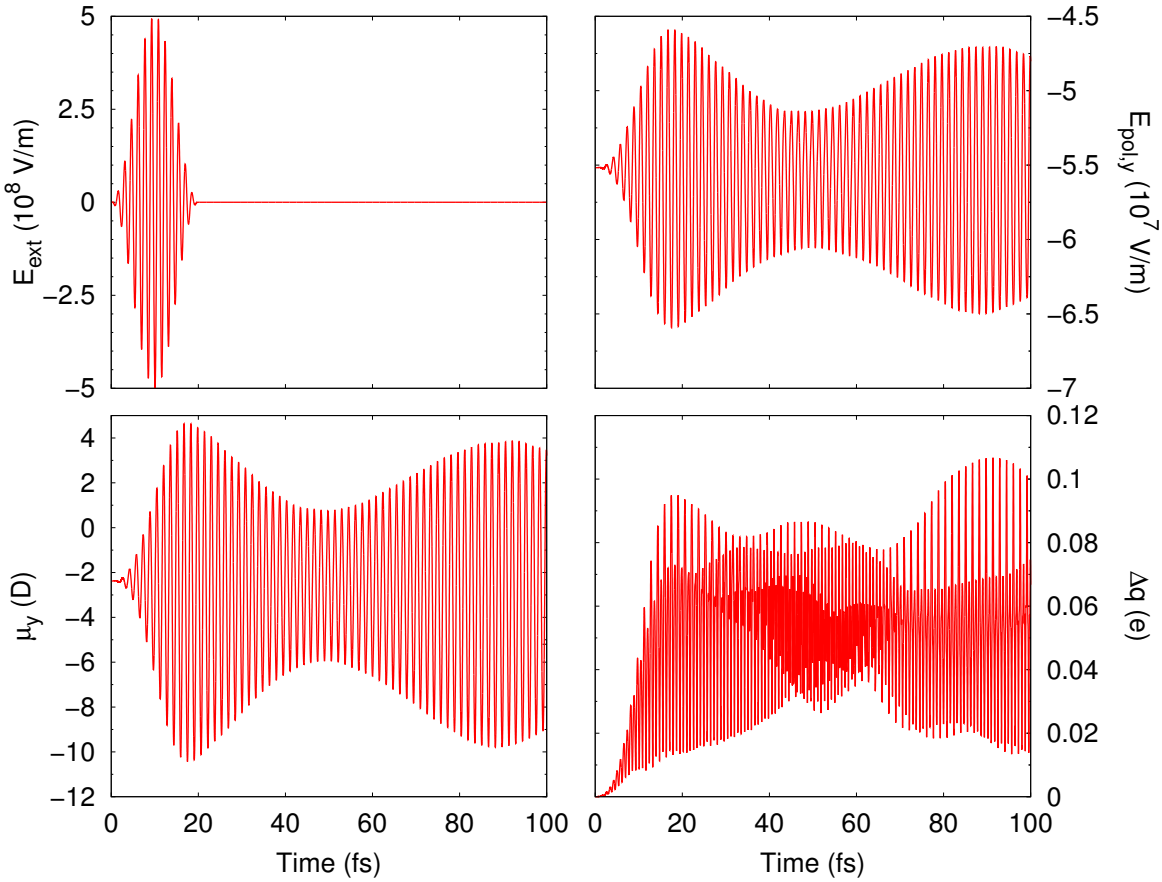


Figure IV.22: The time evolution for the external pulse  $E_{\text{ext}}$ , the  $y$ -component of the polarization field  $E_{\text{pol},y}$  at the mass center,  $y$ -component of the dipole moment  $\mu_y$  and change of Mulliken charges  $\Delta q$  for CCY in arrangement as shown in Fig. IV.17b nearby a  $R = 100$  Å NS with a distance of  $d = 9.5$  Å.

Considering the charged CCY which has a larger first transition dipole moment  $\vec{\mu}_1 = (0, 12.91, 0.003)$  D and oscillator strength of absorption spectra (Fig. IV.18c), Fig. IV.22 shows the weaker pulse mentioned for CCY in Fig. IV.19 polarized along  $y$ -direction to excite the hybrid of a NS and one CCY molecule. From Fig. IV.22, there is also an obvious oscillation of the polarization field, dipole moment and charges with the frequency of the external pulse and a phase shift about  $259^\circ$ . Compared to the case of TET in Fig. IV.20 the oscillations are simpler except for  $\Delta q$  where a multitude of frequencies are found.

Fig. IV.23 shows the  $y$ -component of the polarization field  $E_{\text{pol},y}$  at the mass center of the molecule and the dipole moment  $\mu_y$  for different distances  $d$  for CCY. Due to large difference for the initial CCY electronic structure, there are obvious shifts in the polarization field and dipole moment for different distances at  $t = 0$  fs. Importantly, one can find though the fast oscillation frequency is also independent on the distance, the slow oscillation frequency becomes larger with increasing distance.

Next the influence from the feed back on the nearest molecule in the external field is investigated. To this end the case of no feed back (nfb) is introduced, which neglects the effect from



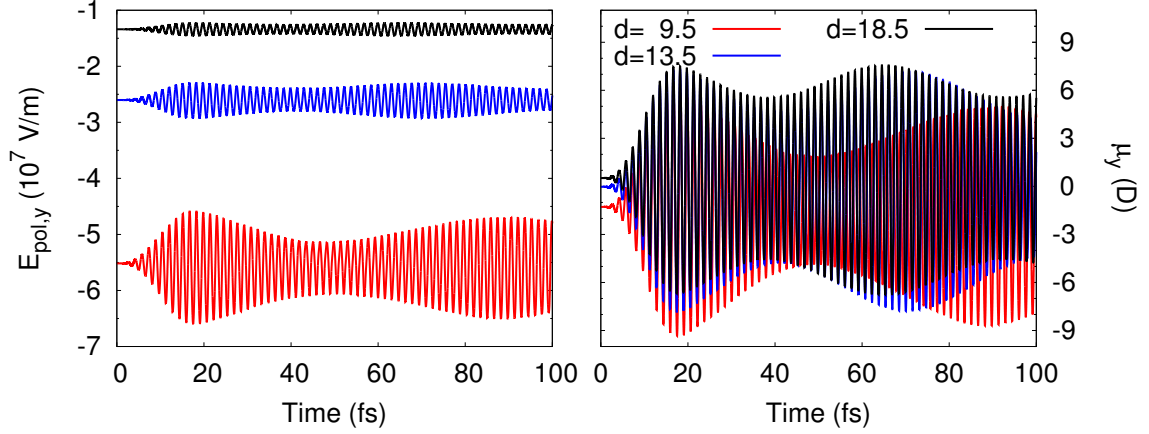


Figure IV.23: The time evolution for the  $y$ -component of the polarization field at the mass center and dipole moment for CCY at different distances of  $d = 9.5$  Å,  $d = 13.5$  Å and  $d = 18.5$  Å with a  $R = 100$  Å NS.

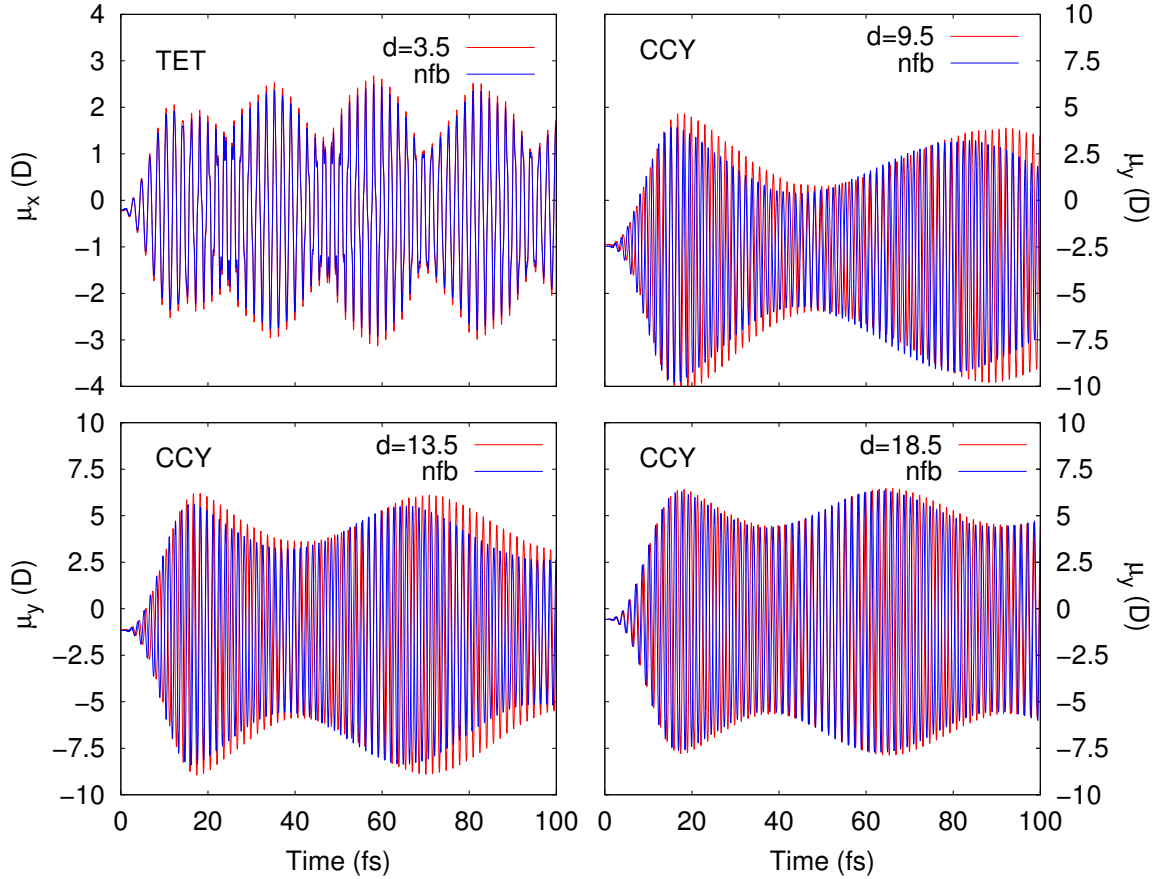


Figure IV.24: The time evolution for dipole moment in  $x$ -direction  $\mu_x$  of TET with  $d = 3.5$  Å, and in  $y$ -direction  $\mu_y$  of CCY with  $d = 9.5$  Å,  $d = 13.5$  Å and  $d = 18.5$  Å compared with the case of no feedback (nfb).

the charge distribution of molecule on the metal NS, i.e. during all time the polarization field is assumed to be constant at the initial polarization field from the static case. (Note that in the

other case at each time step the charge distribution is calculated in the total field, which contains the polarization field obtained from Eq. (II.123) using the charge distribution from the previous time step). From Fig IV.24, one can find even when the distance is very small, the difference between the with and without feed back cases are very small due to the small polarization field for the neutral TET. However, for the charged CCY with distances  $d = 9.5 \text{ \AA}$  and  $d = 13.5 \text{ \AA}$ , the two cases are obviously different.

### 2.3 EXCITON DYNAMICS IN A MODEL AGGREGATE

In the previous section, the influence of a NS on a neighbouring molecule was discussed. From Fig. IV.24, the effect from the NS on a neighbouring TET is very small. Thus a hybrid system of a  $R = 100 \text{ \AA}$  NS and CCY molecules with the nearest distance  $d = 9.5 \text{ \AA}$  is calculated as an example to study EET. As seen from Figs. IV.18 and IV.19, there is only a HOMO-LUMO transition in CCY excited by the external field for both, free molecules and molecule near NS. So the hybrid system consisting of CCY molecules and a metal NS is reduced to the Frenkel model in the HOMO and LUMO basis. From the approximate solution of TDDFT in Sec. II.4.2 and Mulliken analysis, the transition density for molecule  $m$  from occupied single-particle orbital HOMO ( $h$ ) to unoccupied LUMO( $l$ ) is

$$\rho_m^{hl}(\vec{r}) = \langle \Psi_l^f(\vec{r}) | \Psi_h^f(\vec{r}) \rangle \approx \sum_{A \in m} \frac{q_A^{hl}}{N_A} \sum_{\mu \in A} |\varphi_\mu(\vec{r})|^2 = \sum_{A \in m} q_A^{hl} \Upsilon_A(\vec{r}) \quad (\text{IV.9})$$

with the quantity  $N_A$  being the number of basis functions on the atom  $A$  and  $\Upsilon_A(\vec{r})$  is defined from the function Eq. (II.116). The transition charge  $q_A^{hl}$  for atom  $A$  from  $h$  to  $l$  reads

$$q_A^{hl} = \frac{1}{2} \sum_{\mu \in A} \sum_{\nu} \left[ b_{\mu h}^{f*} b_{\nu l}^f S_{\mu\nu} + b_{\nu h}^{f*} b_{\mu l}^f S_{\nu\mu} \right] \quad (\text{IV.10})$$

Thus the transition dipole moment for molecule  $m$  in Mulliken approximation is

$$\vec{d}_m^{hl} = \langle \Psi_l^f(\vec{r}) | \hat{n}(\vec{r}) | \Psi_h^f(\vec{r}) \rangle \approx \sum_{A \in m} q_A^{hl} X_A \quad (\text{IV.11})$$

with the one-particle electron density operator  $\hat{n}(\vec{r})$  and the coordinate  $X_A$  of atom  $A$  in molecule  $m$ . Using this expressions the Coulomb coupling elements between molecule  $m$  and  $n$  from Eq. (II.19) read (for a derivation of this expression in terms of the many-electron transition charges, see Ref. [115])

$$J_{mn}(lh, lh) = \sum_{a \in m} \sum_{b \in n} q_a^{lh} q_b^{hl} \zeta_{ab} \left( |\vec{R}_a - \vec{R}_b| \right) \quad (\text{IV.12})$$

with the function

$$\zeta_{ab} \left( |\vec{R}_a - \vec{R}_b| \right) = \iint \frac{\Upsilon_a(\vec{r}) \Upsilon_b(\vec{r}')}{|\vec{r} - \vec{r}'|} \quad (\text{IV.13})$$

In the following, the analysed hybrid system consists of a  $R = 100 \text{ \AA}$  NS and seven CCY molecules which are positioned linearly in head-to-tail configuration like in Fig. IV.17b with the distance  $d = 9.5 \text{ \AA}$  from NS to the neighbouring CCY molecule (labelled as 1) and  $20 \text{ \AA}$  (long

axis of CCY is 17 Å) between the center of CCY molecules. Based on the DFTB simulation for the hybrid of a NS and one CCY in the previous section, one obtains the Coulomb coupling from Eq. (IV.12) between the molecule 1 and others, Mulliken charges for HOMO and LUMO states, excitation energy  $E_1 = 2$  eV, and the transition dipole moment  $\vec{\mu}_1 = (0.06, 11.65, 0.003)$  D for molecule 1 from Eq. (IV.11) from the self-consistent static case. For the other molecules, a separate calculation of the free molecule is done using HOMO-LUMO DFTB-values. This gives the Coulomb coupling between the other molecules (except the molecule 1), excitation energy  $E_m = 2.02$  eV and  $\vec{\mu}_m = (0, 12.91, 0.003)$  D ( $m = 2, 3, \dots$ ). In the following an aggregate of seven monomers will be considered.

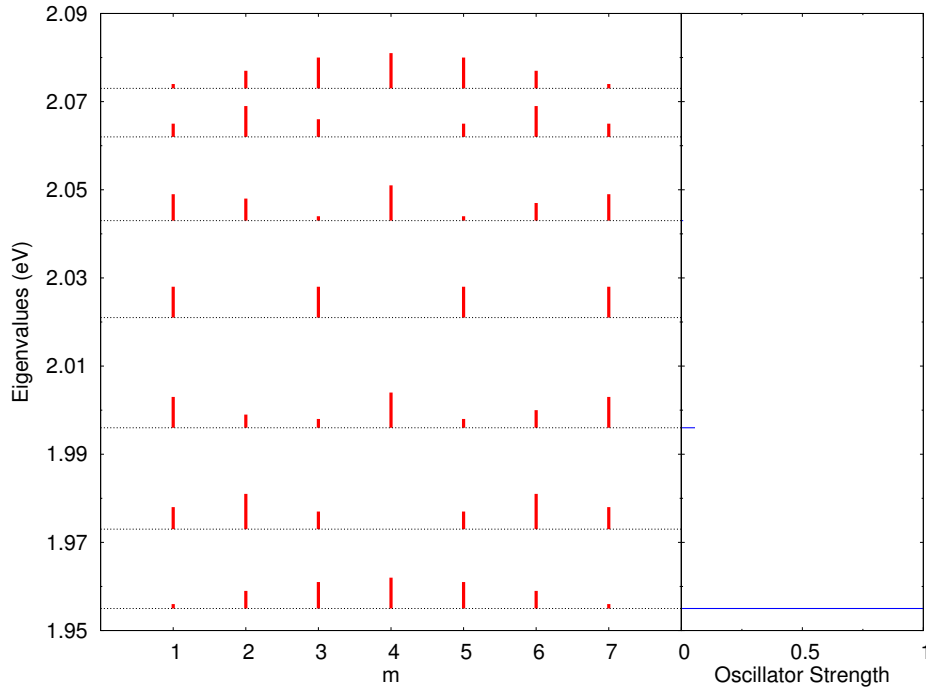


Figure IV.25: Eigenvalues (dotted line), the state character  $|c_{m,\alpha}|^2$  (red) and oscillator strength (blue) of seven site model system described by the Hamiltonian Eq. (IV.14). The onsite energies are  $E_1 = 2$  eV and  $E_{m=2,\dots,7} = 2.02$  eV.

To build the Frenkel system of the hybrid system, the HOMO orbital is assumed as ground state and the LUMO orbital as excited state configuration for all CCY. With the data mentioned above, the Hamiltonian of the hybrid system is obtained from the Frenkel exciton theory in Sec. II.2.1. The Hamiltonian without ground state  $H_S$  reads (in units of  $\text{cm}^{-1}$ )

$$H_S = \begin{pmatrix} 16177 & -247 & -24 & -7 & -3 & -1.5 & -0.9 \\ -247 & 16290 & -254 & -26 & -7.8 & -3.3 & -1.7 \\ -24 & -254 & 16290 & -254 & -26 & -7.8 & -3.3 \\ -7 & -26 & -254 & 16290 & -254 & -26 & -7.8 \\ -3 & -7.8 & -26 & -254 & 16290 & -254 & -26 \\ -1.5 & -3.3 & -7.8 & -26 & -254 & 16290 & -254 \\ -0.9 & -1.7 & -3.3 & -7.8 & -26 & -245 & 16290 \end{pmatrix} \quad (\text{IV.14})$$

Here, it is assumed that the possible effect of intervening molecules can be neglected when calculating the Coulomb coupling between non-neighboring molecules. Fig. IV.25 shows the eigenvalues, the state character  $|c_{m,\alpha}|^2$  and oscillator strength. Due to the small difference in site energies and couplings, this system pretty much follows the general result obtained for a linear chain [64].

The time-evolution of the hybrid system of NS and CCY molecules is obtained by the Eq. (II.55) with an Ohmic spectral density from Eq. (III.8) with  $\omega_c = 180 \text{ cm}^{-1}$  and  $\eta^H = 0.05$  shown as the black in Fig. III.2 for the following three cases: first, include the feed back between the Mulliken charge and polarization field from NS (only for molecule 1) at each time step, abbreviated as “with PF”, i.e. for molecule 1 at each time step the Mulliken charges are summed up from Eq. (II.120) by using the time-dependent populations in the total field (Eq. (IV.5)). The latter contains the polarization field obtained from Eq. (II.123) using the Mulliken charges from the previous time step. The other molecules are simulated only in the external field. Second, only the enhancement part from Eq. (II.91) is considered for molecule 1, abbreviated as “without PF”. Third, only the bare Hamiltonian Eq. (IV.14) in the external field is considered, abbreviated as “without NS”.

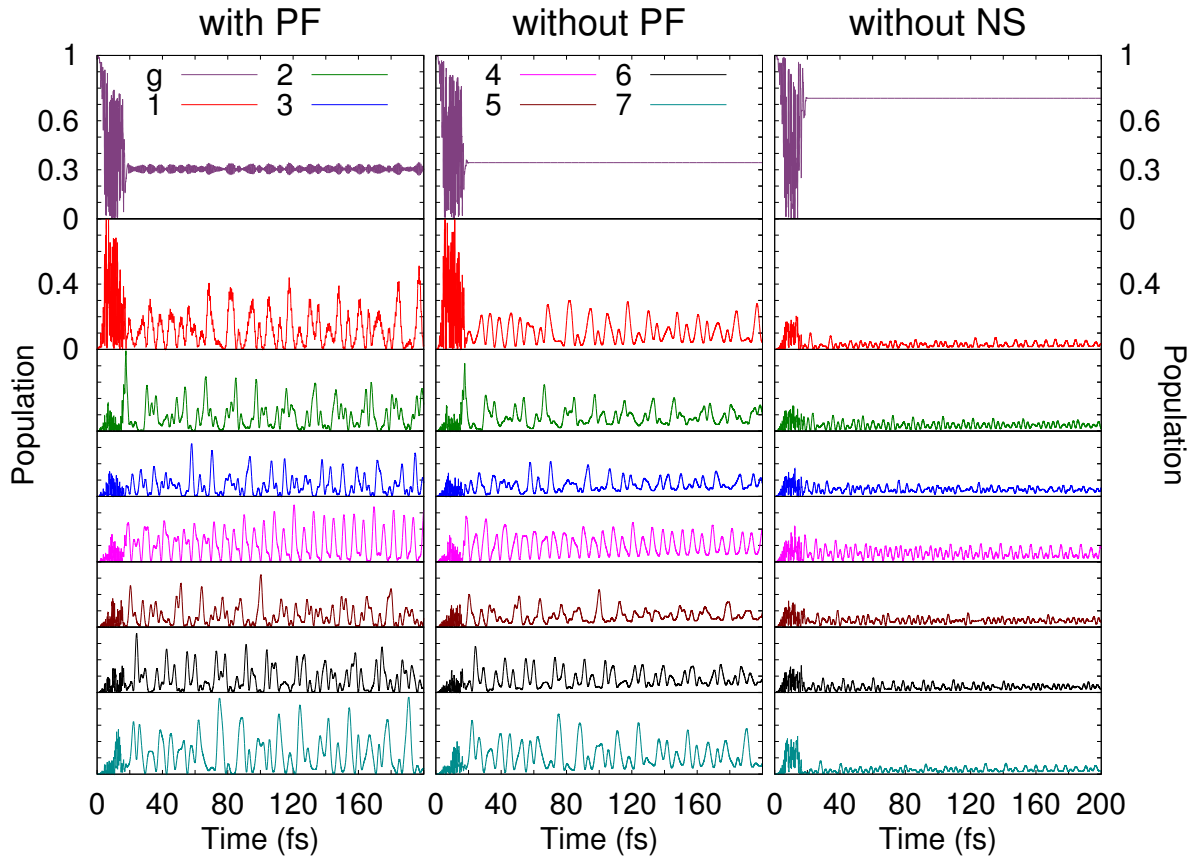


Figure IV.26: Time-evolution for the population of CCY molecules nearby a  $R = 100 \text{ \AA}$  NS at a distance of  $d = 9.5 \text{ \AA}$  driven by a pulse with  $t_{\text{max}} = 20 \text{ fs}$ ,  $E_0 = (0, 5, 0) \times 10^8 \text{ V/m}$  and  $\omega = 2 \text{ eV}$  with/without PF and without NS (tick spacing for the vertical axes is 0.1).

The population results are shown in Fig. IV.26. From the figure the excited state population

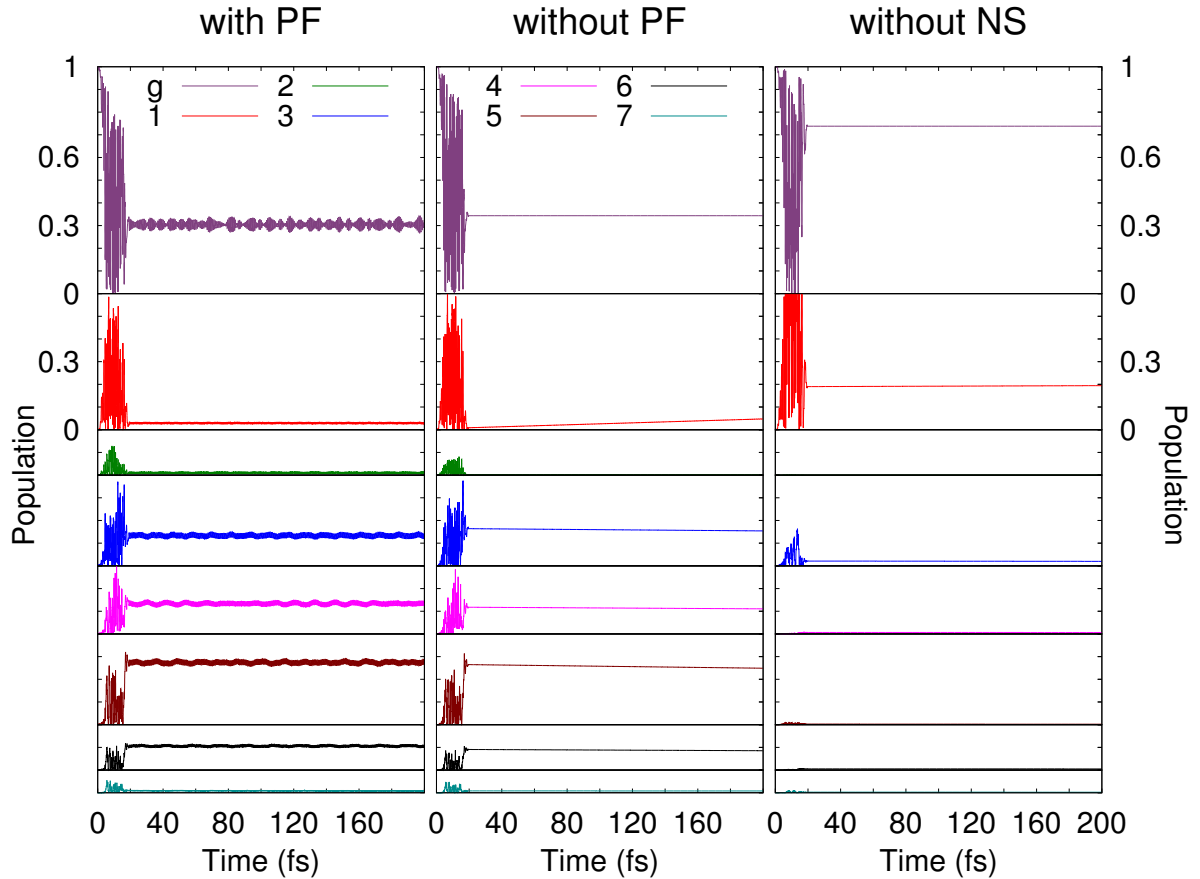


Figure IV.27: Time-evolution for the population in eigenbasis of CCY molecules in the same system as Fig. IV.26 (tick spacing for the vertical axes is 0.1).

induced by the external field is largest for the molecule 1 due to the near-field enhancement by a factor of 3.5. There are oscillations for both “with PF” and “without PF/NS” cases. For “without PF” case, it is obvious that the oscillation amplitude of all molecules become smaller with time. This is not observed for the “with PF” case during 200 fs. In addition, it is clearly found that after the pulse, there is still excitation between ground state and molecule 1 for “with PF” case.

The populations in eigenbasis are shown in Fig. IV.27. It is found that the nearby NS changes the absorption characteristic and dynamics of the CCY molecules. The polarization field acts as a driving force for the polarization dynamics even after the external field is switched off. Overall, however, the effect of the polarization field is modest only. More dramatic are the changes due to the NS’s near field. In the right panel of Fig. IV.27 the excitation of the aggregate follows the distribution of oscillator strength in Fig. IV.25. Including the near field which acts on the  $m = 1$  molecule only (middle and left panels of Fig. IV.27) breaks the symmetry such that the selection rules of the bare aggregate no longer apply.



---

## Chapter V

# Conclusions and Outlook

In this work, exciton dynamics photosynthetic light-harvesting complexes as well as in artificial hybrid system, composed of a metal nanosphere and a dye aggregate have been studied.

In Sec. III.1, the coupling of one-exciton states to vibrational DOFs has been investigated for a model of the FMO complex with a QME approach using different levels of approximation, i.e. the one- and the two-particle description as well as purely excitonic description. In the purely excitonic systems (model I), we only consider the excitation in the bare electronic basis with a spectral density fitted by the low temperature fluorescence line narrowing spectra of B777 complex. In model II, a single intramolecular harmonic vibrational mode is included in the OPA and TPA basis with a selected Ohmic spectral density around  $180 \text{ cm}^{-1}$  yielding the coupling between vibrational mode and protein environment. The focus was on the influence of vibrational and vibronic excitations on the exciton transfer and trapping dynamics. It has been found that the trapping to the RC is accelerated by non-equilibrium exciton-vibrational dynamics at low temperature. At room temperature rapid on-site relaxation causes a transient trapping at site  $m = 1$ , which accelerates the transport to the RC. Therefore, the rate of population in the latter case is not much different comparing with that in the bare electronic case. These observations are only true for the TPA. According to the more approximate OPA the trapping is accelerated at both temperatures. To sum up, explicit EVC indeed modifies the transport characteristics of the FMO complex. However the details not only depend on temperature but also on the level of approximation in the exact exciton-vibrational wave function.

Having access to the exciton-vibrational density matrix, the magnitude of on- and inter-site coherences has been studied. While on-site coherences indicate vibronic or vibrational wave packet dynamics in the site basis, inter-site coherences are key to understand the coupling between different sites of the complex. It is not surprising that such coherences are very important for the strong coupling between sites  $m = 1$  and 2. However, vibronic inter-site coherences connecting the latter two with sites  $m = 3$  and 4 are also of sizeable magnitude. It is important to emphasize that the OPA predicts a qualitatively different behavior as far as magnitude and phase of the vibronic density matrix elements are concerned. Further, vibrational wave packet dynamics in the electronic ground states has been found, which cannot be described by the OPA at all.

It should be pointed out that, of course, the explicit inclusion of vibrational and vibronic non-equilibrium dynamics comes at the expense of sacrificing the non-Markovianity of the total

system. Therefore, a direct comparison with the OPA-like results of Nalbach and coworkers [36, 92] is problematic. In addition in Refs. [36, 92] the exciton Hamiltonian was taken from Adolphs and Renger [96], which was different from the present one. Nevertheless, within the used model the discrepancy between OPA and TPA is pronounced. In this respect the recently introduced multi-configuration time-dependent Hartree description of exciton-vibrational dynamics [89] might, with temperature effects, provide a means for accurate explicit simulation of exciton-vibrational dynamics in photosynthetic complexes.

In Sec. III.2 the model for LH2 developed by Löhner and coworkers [16] is used to discuss the experimental results on the population dynamics of Ref. [102]. The original parameters are changed to fit the peaks of the split B800 bands and the time scales for the population flow. Besides accounting for different sample preparation, the model of Ref. [16] is supplemented by a system-bath description of phase and energy relaxation.

In **Model 4** of Table III.1, an energy shift  $E_s$  between  $A$ - and  $B$ -kind B800 led to a change of the ratio of B800r and B800b peaks. The coupling coefficients  $a_i$  are changed to meet with the time scales for the population flow. Pure dephasing rates  $\hat{\Gamma}_i$  are introduced to broaden the peaks of B800 and B850 bands. Finally, the Coulomb coupling  $J_{800-850}$  has to be chosen 2 times larger than the dipole approximation to reach the best agreement as shown in Fig. III.16d.

By calculating the state character  $c_\alpha$  in Fig. III.15, one finds that the B800 double peaks are in a range where B800 and B850 eigenstates are mixed. This provides evidence that the splitting of B800 bands is related to the excitonic coupling of B800 and B850 BChls  $a$ .

Furthermore, the time scales for the population flow are calculated and compared with the experimental result. It is found that the energy transfer from B800b to B850 band is via two pathways: direct transfer to B850, which is the main pathway, and indirect transfer via B800r to B850. The obtained time scales are in accord with Ref. [102].

In Chap.IV, a proof-of-principle study has been presented to reveal effects of a NS on the QM charge distribution of a molecule and focus on its dynamics. In the static case, a classical macroscopic self-consistent description of the polarization potential between a NS and molecules was combined with a QM model for the charge density in a molecular system. Key to the model has been a discrete representation of the molecular charge density in terms of Mulliken charges. They are obtained using the DFTB method, where they constitute the basic quantity for self-consistent solution of the electronic Schrödinger equation. The latter has been linked to the polarization field, also in a self-consistent manner.

The approach was applied to two exemplary systems, containing dyes typically used for building supramolecular structures or molecular crystals. Whereas for the charge neutral TET the influence of the NS in the hybrid system has been moderate, the positively charged CCY showed rather pronounced effects. A qualitative comparison yielded a rather different dependence on the distance from the NS's surface, e.g. the interaction energy decays more rapidly for TET as compared with CCY. If the molecule's plane faces the NS (parallel case), the difference in distance dependence is only moderate. The dependence on the radius of the NS is similar for the two dyes, i.e. the interaction energy decreases with decreasing radius, which is due to the fact that parts of the molecular charge density move effectively out of the range of interaction. It has also been noticed that the charged system shows a less pronounced orientation dependence



of the interaction energy. The distance dependence has been contrasted to that of an ideal metal NS, interacting with a point charge and a dipole.

In the time-dependent external field case, an approximate TDDFT propagation is used to describe the self-consistent influence between a NS and the nearest molecules. The exciton dynamics molecules are calculated approximately in the molecular orbital basis by the Redfield theory. Because of the limitation for the approximate TDDFT implementation, the external field was not spatially different across the nearest molecule. In this case the influence from the near-field of the NS is very small for the neutral TET. However, the effect on the charged CCY is obvious not only for the nearest molecule (Fig. IV.24) but also for the EET (Fig. IV.26). Future work should be directed towards the inclusion of a spatially varying near field into the calculation of the molecular charge density.

---

---

# References

- [1] R. van Grondelle, J. P. Dekker, T. Gillbro, and V. Sundstrom, “Energy transfer and trapping in photosynthesis,” *Biochim. Biophys. Acta*, vol. 1187, no. 1, pp. 1–65, 1994.
- [2] V. Sundström, T. Pullerits, and R. van Grondelle, “Photosynthetic Light-Harvesting: reconciling dynamics and structure of purple bacterial LH2 reveals function of photosynthetic unit,” *J. Phys. Chem. B*, vol. 103, no. 13, pp. 2327–2346, 1999.
- [3] Y.-C. Cheng and G. R. Fleming, “Dynamics of light harvesting in photosynthesis,” *Annu. Rev. Phys. Chem.*, vol. 60, no. 1, pp. 241–262, 2009.
- [4] B. R. Green and W. W. Parson, *Light-Harvesting Antenna in Photosynthesis*. Kluwer, Dordrecht, 2003.
- [5] R. E. Blankenship, *Molecular Mechanisms of Photosynthesis*. Wiley Blackwell, 2014, 2nd ed.
- [6] H. G. Trüper, “Prokaryotes: an overview with respect to biodiversity and environmental importance,” *Biodivers. Conserv.*, vol. 1, no. 4, pp. 227–236, 1992.
- [7] R. Blankenship, M. Madigan, and C. Bauer, *Anoxygenic Photosynthetic Bacteria*. Springer, Dordrecht, 1995.
- [8] B. Matthews, R. Fenna, M. Bolognesi, M. Schmid, and J. Olson, “Structure of a bacteriochlorophyll *a*-protein from the green photosynthetic bacterium *Prosthecochloris aestuarii*,” *J. Mol. Biol.*, vol. 131, no. 2, pp. 259–285, 1979.
- [9] J. M. Olson, “Chlorophyll organization and function in green photosynthetic bacteria,” *Photochem. Photobiol.*, vol. 67, no. 1, pp. 61–75, 1998.
- [10] Y. Li, W. Zhou, R. Blankenship, and J. Allen, “Crystal structure of the bacteriochlorophyll *a* protein from *Chlorobium tepidum*,” *J. Mol. Biol.*, vol. 271, no. 3, pp. 456–471, 1997.
- [11] D. E. Tronrud, J. Wen, L. Gay, and R. E. Blankenship, “The structural basis for the difference in absorbance spectra for the FMO antenna protein from various green sulfur bacteria,” *Photosynth. Res.*, vol. 100, no. 2, pp. 79–87, 2009.
- [12] T. Mirkovic, E. E. Ostroumov, J. M. Anna, R. van Grondelle, Govindjee, and G. D. Scholes, “Light absorption and energy transfer in the antenna complexes of photosynthetic organisms,” *Chem. Rev.*, vol. 117, no. 2, pp. 249–293, 2017.

- [13] G. McDermott, S. M. Prince, A. A. Freer, A. M. Hawthornthwaite-Lawless, M. Z. Papiz, R. J. Cogdell, and N. W. Isaacs, "Crystal structure of an integral membrane light-harvesting complex from photosynthetic bacteria," *Nature*, vol. 374, pp. 517–521, 1995.
- [14] J. Koepke, X. Hu, C. Muenke, K. Schulten, and H. Michel, "The crystal structure of the light-harvesting complex II (B800–850) from *Rhodospirillum rubrum*," *Structure*, vol. 4, no. 5, pp. 581–597, 1996.
- [15] S. Kereiche, L. Bourinet, W. Keegstra, A. A. Arteni, J.-M. Verbavatz, E. J. Boekema, B. Robert, and A. Gall, "The peripheral light-harvesting complexes from purple sulfur bacteria have different 'ring' sizes," *FEBS Lett.*, vol. 582, no. 25, pp. 3650–3656, 2008.
- [16] A. Löhner, A.-M. Carey, K. Hacking, N. Picken, S. Kelly, R. Cogdell, and J. Köhler, "The origin of the split B800 absorption peak in the LH2 complexes from *Allochromatium vinosum*," *Photosynth. Res.*, vol. 123, no. 1, pp. 23–31, 2015.
- [17] T. Renger and V. May, "Ultrafast exciton motion in photosynthetic antenna systems: The FMO-complex," *J. Phys. Chem. A*, vol. 102, no. 23, pp. 4381–4391, 1998.
- [18] O. Kühn and S. Mukamel, "Probing the two-exciton manifold of light-harvesting antenna complexes using femtosecond four-wave mixing," *J. Phys. Chem. B*, vol. 101, no. 5, pp. 809–816, 1997.
- [19] O. Kühn and V. Sundström, "Energy transfer and relaxation dynamics in light-harvesting antenna complexes of photosynthetic bacteria," *J. Phys. Chem. B*, vol. 101, no. 17, pp. 3432–3440, 1997.
- [20] O. Kühn and V. Sundström, "Pump–probe spectroscopy of dissipative energy transfer dynamics in photosynthetic antenna complexes: A density matrix approach," *J. Chem. Phys.*, vol. 107, no. 11, pp. 4154–4164, 1997.
- [21] W. M. Zhang, T. Meier, V. Chernyak, and S. Mukamel, "Exciton-migration and three-pulse femtosecond optical spectroscopies of photosynthetic antenna complexes," *J. Chem. Phys.*, vol. 108, no. 18, pp. 7763–7774, 1998.
- [22] V. Novoderezhkin, R. Monshouwer, and R. van Grondelle, "Electronic and vibrational coherence in the core light-harvesting antenna of *Rhodospseudomonas viridis*," *J. Phys. Chem. B*, vol. 104, no. 50, pp. 12056–12071, 2000.
- [23] T. Förster, "Energiewanderung und fluoreszenz," *Naturwissenschaften*, vol. 33, pp. 166–175, 1946.
- [24] T. Förster, "Zwischenmolekulare energiewanderung und fluoreszenz," *Ann. Phys.*, vol. 437, pp. 55–75, 1948.
- [25] J. R. Lakowicz, *Principles of fluorescence spectroscopy*. Kluwer, Academic/Plenum, 1999, 2nd ed.

- [26] H. J. Dutton, W. M. Manning, and B. M. Duggar, "Chlorophyll fluorescence and energy transfer in the diatom *nitzschia closterium*," *J. Phys. Chem.*, vol. 47, no. 4, pp. 308–313, 1943.
- [27] G. S. Engel, T. R. Calhoun, E. L. Read, T.-K. Ahn, T. Manal, Y.-C. Cheng, R. E. Blankenship, and G. R. Fleming, "Evidence for wavelike energy transfer through quantum coherence in photosynthetic systems," *Nature*, vol. 446, pp. 782–786, 2007.
- [28] H. Lee, Y.-C. Cheng, and G. R. Fleming, "Coherence dynamics in photosynthesis: Protein protection of excitonic coherence," *Science*, vol. 316, no. 5830, pp. 1462–1465, 2007.
- [29] T. R. Calhoun, N. S. Ginsberg, G. S. Schlau-Cohen, Y.-C. Cheng, M. Ballottari, R. Bassi, and G. R. Fleming, "Quantum coherence enabled determination of the energy landscape in light-harvesting complex II," *J. Phys. Chem. B*, vol. 113, no. 51, pp. 16291–16295, 2009.
- [30] E. Collini, C. Y. Wong, K. E. Wilk, P. M. G. Curmi, P. Brumer, and G. D. Scholes, "Coherently wired light-harvesting in photosynthetic marine algae at ambient temperature," *Nature*, vol. 463, pp. 644–647, 2010.
- [31] G. Panitchayangkoon, D. Hayes, K. A. Fransted, J. R. Caram, E. Harel, J. Wen, R. E. Blankenship, and G. S. Engel, "Long-lived quantum coherence in photosynthetic complexes at physiological temperature," *Proc. Natl. Acad. Sci. U.S.A.*, vol. 107, no. 29, pp. 12766–12770, 2010.
- [32] M. Mohseni, P. Rebentrost, S. Lloyd, and A. Aspuru-Guzik, "Environment-assisted quantum walks in photosynthetic energy transfer," *J. Chem. Phys.*, vol. 129, no. 17, p. 174106, 2008.
- [33] F. Caruso, A. W. Chin, A. Datta, S. F. Huelga, and M. B. Plenio, "Highly efficient energy excitation transfer in light-harvesting complexes: The fundamental role of noise-assisted transport," *J. Chem. Phys.*, vol. 131, no. 10, p. 105106, 2009.
- [34] J. Cao and R. J. Silbey, "Optimization of exciton trapping in energy transfer processes," *J. Phys. Chem. A*, vol. 113, no. 50, pp. 13825–13838, 2009.
- [35] S. Huelga and M. Plenio, "Vibrations, quanta and biology," *Contemp. Phys.*, vol. 54, no. 4, pp. 181–207, 2013.
- [36] P. Nalbach, C. Mujica-Martinez, and M. Thorwart, "Vibronically coherent speed-up of the excitation energy transfer in the Fenna-Matthews-Olson complex," *Phys. Rev. E*, vol. 91, no. 2, p. 022706, 2015.
- [37] A. P. Alivisatos, "Semiconductor clusters, nanocrystals, and quantum dots," *Science*, vol. 271, no. 5251, pp. 933–937, 1996.
- [38] S. Link and M. A. El-Sayed, "Shape and size dependence of radiative, non-radiative and photothermal properties of gold nanocrystals," *Int. Rev. Phys. Chem.*, vol. 19, no. 3, pp. 409–453, 2000.

- [39] D. Y. Godovski, *Electron behavior and magnetic properties of polymer nanocomposites*. Berlin, Heidelberg: Springer Berlin Heidelberg, 1995.
- [40] L. Brus, “Semiconductor colloids: individual nanocrystals, opals and porous silicon,” *Curr. Opin. Colloid Interface Sci.*, vol. 1, no. 2, pp. 197–201, 1996.
- [41] S. Suresh, “Semiconductor nanomaterials, methods and applications: A review,” *Nanosci. Nanotechnol.*, vol. 3, pp. 62–74, 2013.
- [42] D. Gramotnev and S. Bozhevolnyi, “Nanofocusing of electromagnetic radiation,” *Nat. Photonics*, vol. 8, pp. 13–22, 2014.
- [43] M. Fleischmann, P. J. Hendra, and A. J. McQuillan, “Raman spectra of pyridine adsorbed at a silver electrode,” *Chem. Phys. Lett.*, vol. 26, pp. 163–166, 1974.
- [44] L. Jensen, L. L. Zhao, and G. C. Schatz, “Size-dependence of the enhanced Raman scattering of pyridine adsorbed on Agn ( $n = 2-8, 20$ ) clusters,” *J. Phys. Chem. C*, vol. 111, no. 12, pp. 4756–4764, 2007.
- [45] G. C. Schatz, “Using theory and computation to model nanoscale properties,” *Proc. Natl. Acad. Sci. USA*, vol. 104, no. 17, p. 6885–6892, 2007.
- [46] H. Chen, J. M. McMahon, M. A. Ratner, and G. C. Schatz, “Classical electrodynamics coupled to quantum mechanics for calculation of molecular optical properties: a RT-TDDFT/FDTD approach,” *J. Phys. Chem. C*, vol. 114, no. 34, p. 14384–14392, 2010.
- [47] N. L. Gruenke, M. F. Cardinal, M. O. McAnally, R. R. Frontiera, G. C. Schatz, and R. P. V. Duyne, “Ultrafast and nonlinear surface-enhanced Raman spectroscopy,” *Chem. Soc. Rev.*, vol. 45, p. 2263–2290, 2016.
- [48] L. Jensen, C. M. Aikens, and G. C. Schatz, “Electronic structure methods for studying surface-enhanced Raman scattering,” *Chem. Soc. Rev.*, vol. 37, pp. 1061–1073, 2008.
- [49] S. M. Morton, D. W. Silverstein, and L. Jensen, “Theoretical studies of plasmonics using electronic structure methods,” *Chem. Rev.*, vol. 111, no. 6, pp. 3962–3994, 2011.
- [50] H. Chen, G. C. Schatz, and M. A. Ratner, “Experimental and theoretical studies of plasmon-molecule interactions,” *Rep. Prog. Phys.*, vol. 75, no. 9, p. 096402, 2012.
- [51] S. Malola, L. Lehtovaara, J. Enkovaara, and H. Häkkinen, “Birth of the localized surface plasmon resonance in monolayer-protected gold nanoclusters,” *ACS Nano*, vol. 7, no. 11, pp. 10263–10270, 2013.
- [52] K. Iida, M. Noda, K. Ishimura, and K. Nobusada, “First-principles computational visualization of localized surface plasmon resonance in gold nanoclusters,” *J. Phys. Chem. A*, vol. 118, no. 47, pp. 11317–11322, 2014.
- [53] S. Corni and J. Tomasi, “Enhanced response properties of a chromophore physisorbed on a metal particle,” *J. Chem. Phys.*, vol. 114, no. 8, pp. 3739–3751, 2001.

- [54] J. Mullin, N. Valley, M. G. Blaber, and G. C. Schatz, “Combined quantum mechanics (TDDFT) and classical electrodynamics (Mie theory) methods for calculating surface enhanced Raman and Hyper-Raman spectra,” *J. Phys. Chem. A*, vol. 116, no. 38, pp. 9574–9581, 2012.
- [55] Y. Gao and D. Neuhauser, “Communication: Dynamical embedding: Correct quantum response from coupling TDDFT for a small cluster with classical near-field electrodynamics for an extended region,” *J. Chem. Phys.*, vol. 138, no. 18, p. 181105, 2013.
- [56] A. Sakko, T. P. Rossi, and R. M. Nieminen, “Dynamical coupling of plasmons and molecular excitations by hybrid quantum/classical calculations: time-domain approach,” *J. Phys.: Condens. Matter*, vol. 26, no. 31, p. 315013, 2014.
- [57] S. M. Morton and L. Jensen, “A discrete interaction model/quantum mechanical method for describing response properties of molecules adsorbed on metal nanoparticles,” *J. Chem. Phys.*, vol. 133, no. 7, p. 074103, 2010.
- [58] J. L. Payton, S. M. Morton, J. E. Moore, and L. Jensen, “A discrete interaction model/quantum mechanical method for simulating surface-enhanced Raman spectroscopy,” *J. Chem. Phys.*, vol. 136, no. 21, p. 214103, 2012.
- [59] Z. Rinkevicius, J. A. R. Sandberg, X. Li, M. Linares, P. Norman, and H. Ågren, “Hybrid complex polarization propagator/molecular mechanics method for heterogeneous environments,” *J. Chem. Theory Comput.*, vol. 12, no. 6, pp. 2661–2667, 2016.
- [60] Y. Zelinsky, Y. Zhang, and V. May, “Supramolecular complex coupled to a metal nanoparticle: Computational studies on the optical absorption,” *J. Phys. Chem. A*, vol. 116, no. 46, pp. 11330–11340, 2012.
- [61] Y. Zelinsky and V. May, “Optical properties of supramolecular complexes coupled to a metal-nanoparticle: A computational study,” *Chem. Phys. Lett.*, vol. 511, p. 372–377, 2011.
- [62] Y. Zhang, Y. Zelinsky, and V. May, “Time and frequency resolved emission of molecular systems coupled to a metal nanoparticle,” *J. Nanophotonics*, vol. 6, p. 063533, 2012.
- [63] L. Wang and V. May, “Plasmon assisted control of photo-induced excitation energy transfer in a molecular chain,” *J. Phys. B: At. Mol. Opt. Phys.*, vol. 50, p. 154003, 2017.
- [64] V. May and O. Kühn, *Charge and energy transfer dynamics in molecular systems*. Wiley-VCH: Weinheim, 2011, 3rd ed.
- [65] M. Schröter, S. Ivanov, J. Schulze, S. Polyutov, Y. Yan, T. Pullerits, and O. Kühn, “Exciton–vibrational coupling in the dynamics and spectroscopy of Frenkel excitons in molecular aggregates,” *Phys. Rep.*, vol. 567, pp. 1–78, 2015.
- [66] J. D. Jackson, *Classical Electrodynamics*. Wiley, 1999, 3rd ed., 1999.
- [67] K. K. Roy, *Potential Theory in Applied Geophysics*. Springer, Berlin, Heidelberg 2008.

- [68] T. A. Niehaus, S. Suhai, F. Della Sala, P. Lugli, M. Elstner, G. Seifert, and T. Frauenheim, “Tight-binding approach to time-dependent density-functional response theory,” *Phys. Rev. B*, vol. 63, p. 085108, 2001.
- [69] P. Hohenberg and W. Kohn, “Inhomogeneous electron gas,” *Phys. Rev.*, vol. 136, pp. B864–B871, 1964.
- [70] W. Kohn and L. J. Sham, “Self-consistent equations including exchange and correlation effects,” *Phys. Rev.*, vol. 140, pp. A1133–A1138, 1965.
- [71] W. M. C. Foulkes and R. Haydock, “Tight-binding models and density-functional theory,” *Phys. Rev. B*, vol. 39, pp. 12520–12536, 1989.
- [72] G. Seifert, H. Eschrig, and W. Bierger, “An approximation variant of LCAO-X-ALPHA methods,” *Z. Phys. Chem.*, vol. 267, p. 529, 1986.
- [73] H. Eschrig and I. Bergert, “An optimized LCAO version for band structure calculations application to copper,” *Phys. Status Solidi B*, vol. 90, no. 2, pp. 621–628, 1978.
- [74] P. Sitch, T. Frauenheim, and R. Jones, “A density functional tight-binding approach for modelling Ge and GeH structures,” *J. Phys. Condens. Matter*, vol. 8, no. 37, p. 6873, 1996.
- [75] J. Widany, F. Weich, T. Köhler, D. Porezag, and T. Frauenheim, “Dynamic properties and structure formation of boron and carbon nitrides,” *Diam. Relat. Mater.*, vol. 5, no. 9, pp. 1031–1041, 1996.
- [76] F. Weich, J. Widany, and T. Frauenheim, “Paracyanogenlike structures in high-density amorphous carbon nitride,” *Phys. Rev. Lett.*, vol. 78, pp. 3326–3329, 1997.
- [77] M. Elstner, D. Porezag, G. Jungnickel, J. Elsner, M. Haugk, T. Frauenheim, S. Suhai, and G. Seifert, “Self-consistent-charge density-functional tight-binding method for simulations of complex materials properties,” *Phys. Rev. B*, vol. 58, pp. 7260–7268, 1998.
- [78] R. Pariser, “Theory of the electronic spectra and structure of the polyacenes and of alternant hydrocarbons,” *J. Chem. Phys.*, vol. 24, no. 2, pp. 250–268, 1956.
- [79] R. S. Mulliken, “Electronic population analysis on LCAO–MO molecular wave functions. I,” *J. Chem. Phys.*, vol. 23, no. 10, pp. 1833–1840, 1955.
- [80] T. A. Niehaus, D. Heringer, B. Torralva, and T. Frauenheim, “Importance of electronic self-consistency in the TDDFT based treatment of nonadiabatic molecular dynamics,” *Eur. Phys. J. D*, vol. 35, no. 3, pp. 467–477, 2005.
- [81] E. Runge and E. K. U. Gross, “Density-functional theory for time-dependent systems,” *Phys. Rev. Lett.*, vol. 52, pp. 997–1000, 1984.
- [82] E. Gross and W. Kohn, “Time-dependent density-functional theory,” *Adv. Quantum Chem.*, vol. 21, pp. 255–291, 1990.



- [83] M. Graf and P. Vogl, “Electromagnetic fields and dielectric response in empirical tight-binding theory,” *Phys. Rev. B*, vol. 51, pp. 4940–4949, 1995.
- [84] R. E. Blankenship, *Molecular mechanisms of photosynthesis*. John Wiley & Sons, 2013.
- [85] M. T. Milder, B. Brüggemann, R. van Grondelle, and J. L. Herek, “Revisiting the optical properties of the FMO protein,” *Photosynth. Res.*, vol. 104, no. 2, pp. 257–274, 2010.
- [86] M. Wendling, T. Pullerits, M. A. Przyjalowski, S. I. Vulto, T. J. Aartsma, R. van Grondelle, and H. van Amerongen, “Electron-vibrational coupling in the Fenna-Matthews-Olson complex of *Prosthecochloris aestuarii* determined by temperature-dependent absorption and fluorescence line-narrowing measurements,” *J. Phys. Chem. B*, vol. 104, no. 24, pp. 5825–5831, 2000.
- [87] C. Kreisbeck and T. Kramer, “Long-lived electronic coherence in dissipative exciton dynamics of light-harvesting complexes,” *J. Phys. Chem. Lett.*, vol. 3, no. 19, pp. 2828–2833, 2012.
- [88] O. Vendrell and H.-D. Meyer, “Multilayer multiconfiguration time-dependent hartree method: Implementation and applications to a Henon-Heiles hamiltonian and to pyrazine,” *J. Chem. Phys.*, vol. 134, no. 4, p. 044135, 2011.
- [89] J. Schulze and O. Kühn, “Explicit correlated exciton-vibrational dynamics of the FMO complex,” *J. Phys. Chem. B*, vol. 119, no. 20, pp. 6211–6216, 2015.
- [90] O. Kühn, T. Renger, and V. May, “Theory of exciton-vibrational dynamics in molecular dimers,” *Chem. Phys.*, vol. 204, no. 1, pp. 99–114, 1996.
- [91] V. Butkus, L. Valkunas, and D. Abramavicius, “Vibronic phenomena and exciton-vibrational interference in two-dimensional spectra of molecular aggregates,” *J. Chem. Phys.*, vol. 140, no. 3, p. 034306, 2014.
- [92] C. Mujica-Martinez and P. Nalbach, “On the influence of underdamped vibrations on coherence and energy transfer times in light-harvesting complexes,” *Ann. Phys.*, vol. 527, no. 9-10, pp. 592–600, 2015.
- [93] J. Moix, J. Wu, P. Huo, D. Coker, and J. Cao, “Efficient energy transfer in light-harvesting systems, III: The influence of the eighth bacteriochlorophyll on the dynamics and efficiency in FMO,” *J. Phys. Chem. Lett.*, vol. 2, no. 24, pp. 3045–3052, 2011.
- [94] E. Rivera, D. Montemayor, M. Masia, and D. F. Coker, “Influence of site-dependent pigment-protein interactions on excitation energy transfer in photosynthetic light harvesting,” *J. Phys. Chem. B*, vol. 117, no. 18, pp. 5510–5521, 2013.
- [95] T. Renger and R. Marcus, “On the relation of protein dynamics and exciton relaxation in pigment-protein complexes: an estimation of the spectral density and a theory for the calculation of optical spectra,” *J. Chem. Phys.*, vol. 116, no. 22, pp. 9997–10019, 2002.

- [96] J. Adolphs and T. Renger, “How proteins trigger excitation energy transfer in the FMO complex of green sulfur bacteria,” *Biophys. J.*, vol. 91, no. 8, pp. 2778–2797, 2006.
- [97] M. Chachisvilis, H. Fidder, T. Pullerits, and V. Sundström, “Coherent nuclear motions in light-harvesting pigments and dye molecules, probed by ultrafast spectroscopy,” *J. Raman Spectrosc.*, vol. 26, no. 7, pp. 513–522, 1995.
- [98] B. van Dijk, T. Nozawa, and A. J. Hoff, “The B800–850 complex of the purple bacterium chromatium tepidum: low-temperature absorption and Stark spectra,” *Spectrochim. Acta A Mol. Biomol. Spectrosc.*, vol. 54, no. 9, pp. 1269–1278, 1998.
- [99] D. M. Niedzwiedzki, D. Bina, N. Picken, S. Honkanen, R. E. Blankenship, D. Holten, and R. J. Cogdell, “Spectroscopic studies of two spectral variants of light-harvesting complex 2 (LH2) from the photosynthetic purple sulfur bacterium *Allochromatium vinosum*,” *Biochim. Biophys. Acta Bioenerg.*, vol. 1817, no. 9, pp. 1576–1587, 2012.
- [100] A. Kell, M. Jassas, K. Acharya, K. Hacking, R. J. Cogdell, and R. Jankowiak, “Conformational complexity in the LH2 antenna of the purple sulfur bacterium *Allochromatium vinosum* revealed by Hole-Burning spectroscopy,” *J. Phys. Chem. A*, vol. 121, no. 23, pp. 4435–4446, 2017.
- [101] L. Lüer, A.-M. Carey, S. Henry, M. Maiuri, K. Hacking, D. Polli, G. Cerullo, and R. J. Cogdell, “Elementary energy transfer pathways in *Allochromatium vinosum* photosynthetic membranes,” *Biophys. J.*, vol. 109, no. 9, pp. 1885–1898, 2015.
- [102] M. Schröter, M. J. P. Alcocer, R. J. Cogdell, O. Kühn, and D. Zigmantas, “Origin of the two bands in the B800 ring and their involvement in the energy transfer network of *Allochromatium vinosum*,” *J. Phys. Chem. Lett.*, vol. 9, no. 6, pp. 1340–1345, 2018.
- [103] M. Rätsep, Z.-L. Cai, J. R. Reimers, and A. Freiberg, “Demonstration and interpretation of significant asymmetry in the low-resolution and high-resolution  $Q_y$  fluorescence and absorption spectra of bacteriochlorophyll  $a$ ,” *J. Chem. Phys.*, vol. 134, no. 2, p. 024506, 2011.
- [104] O. Kühn, V. Sundström, and T. Pullerits, “Fluorescence depolarization dynamics in the B850 complex of purple bacteria,” *Chem. Phys.*, vol. 275, no. 1, pp. 15–30, 2002.
- [105] W. Hou and S. B. Cronin, “A review of surface plasmon resonance-enhanced photocatalysis,” *Adv. Funct. Mater.*, vol. 23, p. 1612–1619, 2013.
- [106] L. Piatkowski, N. Accanto, and N. F. van Hulst, “Ultrafast meets ultrasmall: Controlling nanoantennas and molecules,” *ACS Photonics*, vol. 3, p. 1401–1414, 2016.
- [107] M. Schwoerer and H. C. Wolf, *Organic Molecular Solids*. Weinheim: Wiley-VCH, 2007.
- [108] B. Aradi, B. Hourahine, and T. Frauenheim, “DFTB+, a sparse matrix-based implementation of the DFTB method,” *J. Phys. Chem. A*, vol. 111, no. 26, pp. 5678–5684, 2007.

- [109] S. Karaca and N. Elmacı, “A computational study on the excited state properties of a cationic cyanine dye: TTBC,” *Comp. Theor. Chem.*, vol. 964, pp. 160–168, 2011.
- [110] T. Kobayashi, *J-Aggregates*. World Scientific, 2012.
- [111] H. von Berlepsch and C. Böttcher, “Supramolecular structure of TTBC J-Aggregates in solution and on surface,” *Langmuir*, vol. 29, pp. 4948–4958, 2013.
- [112] T. Kubař, Z. Bodrog, M. Gaus, C. Köhler, B. Aradi, T. Frauenheim, and M. Elstner, “Parametrization of the SCC-DFTB method for halogens,” *J. Chem. Theory Comput.*, vol. 9, p. 2939–2949, 2013.
- [113] “Nist polycyclic aromatic hydrocarbon structure index.” <https://pah.nist.gov/?q=pah040>, accessed Feb. 19, 2019.
- [114] S. Karaca and N. Elmacı, “A computational study on the excited state properties of a cationic cyanine dye: TTBC,” *Comp. Theor. Chem.*, vol. 964, no. 1, pp. 160–168, 2011.
- [115] P.-A. Plötz, T. Niehaus, and O. Kühn, “A new efficient method for calculation of Frenkel exciton parameters in molecular aggregates,” *J. Chem. Phys.*, vol. 140, no. 17, p. 174101, 2014.



# Curriculum Vitae

## Personal Data

**Name:** Xiaomeng Liu  
**Date of Birth:** 02.10.1987  
**Place of Birth:** Shandong  
**Nationality:** Chinese

## Conference and seminar contributions

Jun. 2017 Poster: “Influencing Exciton Dynamics with Near Fields”, SFB final conference, *Rostock University*

Mar. 2017 Talk: “Triggering excitation energy transfer in molecular aggregates via nanoparticle near-fields”, DPG, *Maniz University*

Sep. 2016 Poster: “Influence of vibrations on the energy transfer in Fenna-Matthews-Olson complex”, High-Dimensional Quantum Dynamics, *Rostock University*

Jul. 2016 Poster: “Influence of vibrations on the energy transfer in Fenna-Matthews-Olson complex”, 621. WE-Heraeus-Seminar, *Bonn*

Sep. 2015 Poster: “Influence of vibrations on the energy transfer in Fenna-Matthews-Olson complex”, CERF15, *Rostock University*

Mar. 2015 Talk: “Influence of vibrations on the energy transfer in Fenna-Matthews-Olson complex”, DPG, *Heidelberg University*

## Publications

1. [Xiaomeng Liu](#), and Oliver Kühn, “The light-harvesting complex 2 of allochromatium vinosum: B800 absorption band splitting and exciton relaxation”, *arXiv*: 1905.13623 [physics.chem-phs] (2019)
2. [Xiaomeng Liu](#), Lennart Seiffert, Thomas Fennel and Oliver Kühn, “A DFT-based Tight-Binding Approach to the Self-consistent Description of Molecule Metal-Nanoparticle Interactions”, *Journal of Physics B* xxx, yyy (2019) *arXiv*: 1901.03740 [physics.chem-phs]
3. [Xiaomeng Liu](#), and Oliver Kühn, “Vibrational and Vibronic Coherences in the Dynamics of the FMO Complex”, *Chem. Phys.* **481**, 272 (2016)



# Acknowledgments

First of all, I would like to express my thanks to Prof. Dr. Oliver Kühn, who enabled me to work scientifically during my doctoral studies in the group “Molecular Quantum Dynamics”. He is very kind to give the constructive advice and nice guidance in the work.

I also thank to our colleagues in the group, especially Per-Arno Plötz for the discussing about the extension for the DFTB, and Marco Schröter for sharing the experimental data and discussing in LH2 absorption spectra.

Special thanks to Prof. Thomas Niehaus for the approximate TDDFT program. Thanks to Lennart Seiffert for the classical description of the NS.

Thanks for the financial support by Deutsche Forschungsgemeinschaft (DFG) through Sfb 652.

Finally, I also thank to my parents who are always helping and supporting me without any complaint. And thanks to my friends in Rostock.





# Eidesstattliche Versicherung

Ich versichere hiermit an Eides statt, dass ich die vorliegende Arbeit selbstständig angefertigt und ohne fremde Hilfe verfasst habe. Dazu habe ich keine außer den von mir angegebenen Hilfsmitteln und Quellen verwendet und die den benutzten Werken inhaltlich und wörtlich entnommenen Stellen habe ich als solche kenntlich gemacht.

Rostock

\_\_\_\_\_  
(Abgabedatum)

\_\_\_\_\_  
(Vollständige Unterschrift)